LBL-34838
UC-400

Lawrence Berkeley Laboratory

UNIVERSITY OF CALIFORNIA

EARTH SCIENCES DIVISION

Hydrogeologic Characterization of a Fractured Granitic Rock Aquifer, Raymond, California

A.J.B. Cohen
(M.S. Thesis)

October 1993

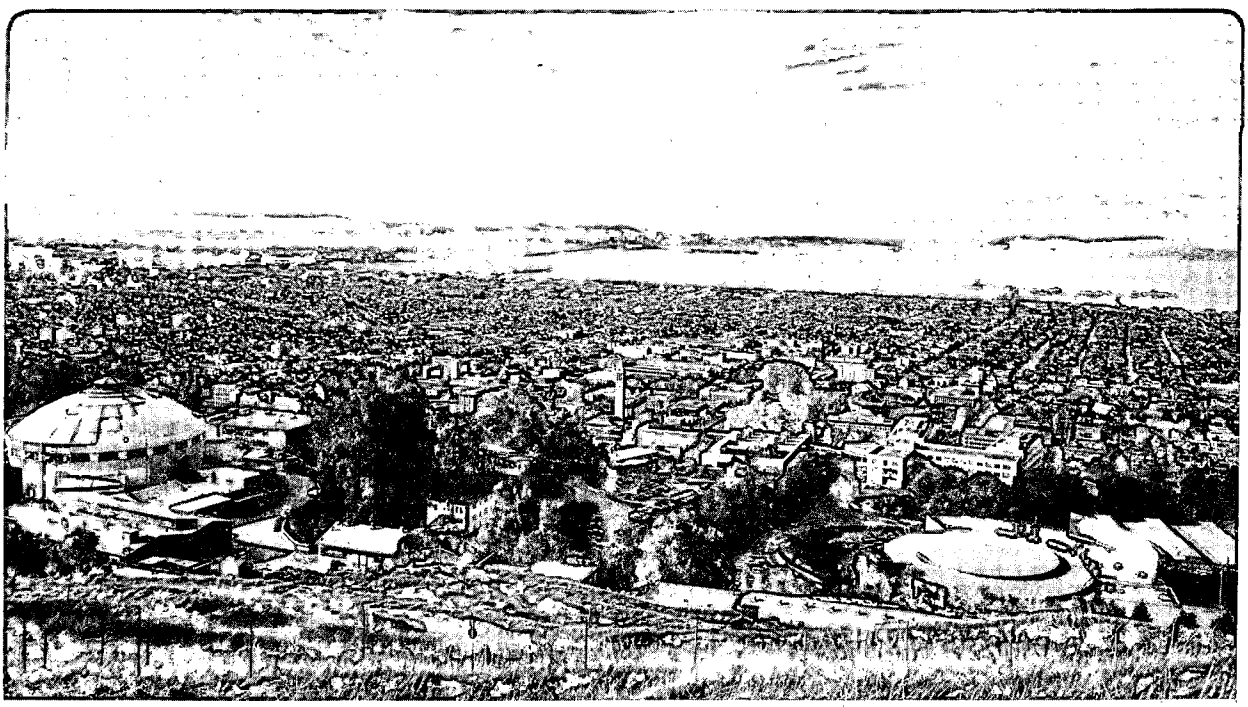

LOAN COPY
Circulates
for 4 weeks
Bldg. 50 Library.
Copy 2
LBL-34838

Prepared for the U.S. Department of Energy under Contract Number DE-AC03-76SF00098

DISCLAIMER

This document was prepared as an account of work sponsored by the United States Government. Neither the United States Government nor any agency thereof, nor The Regents of the University of California, nor any of their employees, makes any warranty, express or implied, or assumes any legal liability or responsibility for the accuracy, completeness, or usefulness of any information, apparatus, product, or process disclosed, or represents that its use would not infringe privately owned rights. Reference herein to any specific commercial product, process, or service by its trade name, trademark, manufacturer, or otherwise, does not necessarily constitute or imply its endorsement, recommendation, or favoring by the United States Government or any agency thereof, or The Regents of the University of California. The views and opinions of authors expressed herein do not necessarily state or reflect those of the United States Government or any agency thereof or The Regents of the University of California and shall not be used for advertising or product endorsement purposes.

Lawrence Berkeley Laboratory is an equal opportunity employer.

DISCLAIMER

This document was prepared as an account of work sponsored by the United States Government. While this document is believed to contain correct information, neither the United States Government nor any agency thereof, nor the Regents of the University of California, nor any of their employees, makes any warranty, express or implied, or assumes any legal responsibility for the accuracy, completeness, or usefulness of any information, apparatus, product, or process disclosed, or represents that its use would not infringe privately owned rights. Reference herein to any specific commercial product, process, or service by its trade name, trademark, manufacturer, or otherwise, does not necessarily constitute or imply its endorsement, recommendation, or favoring by the United States Government or any agency thereof, or the Regents of the University of California. The views and opinions of authors expressed herein do not necessarily state or reflect those of the United States Government or any agency thereof or the Regents of the University of California.

LBL-34838
UC-400

HYDROGEOLOGIC CHARACTERIZATION OF A FRACTURED GRANITIC ROCK AQUIFER, RAYMOND, CALIFORNIA

Andrew J. B. Cohen

M. S. Thesis

Earth Sciences Division
Lawrence Berkeley Laboratory
University of California
Berkeley, CA 94720

October 1993

This work was supported by the U. S. Environmental Protection Agency, under Interagency Agreement DW-89935185-01-2, through U. S. DOE Contract DE-AC03-76SF00098.

recycled paper

HYDROGEOLOGIC CHARACTERIZATION OF A FRACTURED GRANITIC ROCK AQUIFER, RAYMOND, CALIFORNIA

Andrew J. B. Cohen

ABSTRACT

The hydrogeologic properties of a shallow, fractured granitic rock aquifer in the foothills of the Sierra Nevada, California were investigated via the analysis of borehole geophysical logs and pumping tests. The drawdowns produced during these tests are not indicative of any simple conceptual aquifer model, and borehole logs show that the granite is intensely fractured. These observations are suggestive of a complex fracture-flow geometry which is extremely difficult to decipher. However, through the measurement of orientations of individual subsurface fractures from acoustic televiewer logs, and correlation between particular fractures and electrical resistivity and thermal-pulse flowmeter logs, it was found that the aquifer is, in general, comprised of two subhorizontal and nearly parallel zones of unloading fractures. Downhole flowmeter measurements taken in several wells provide further evidence for the inferred dual-layer structure of the aquifer, as well as yield quantitative measures of the contribution of flow from each zone. Analysis of drawdowns in pumped wells reveals that there are zones of relatively high transmissivity immediately around them. It was found that these properties, as well as a nearby zone of lower transmissivity, can account for their observed drawdowns. A numerical model was constructed to test whether these major heterogeneities could also account for the drawdowns in observation wells. This stepwise analysis of both the geophysical and hydrological data resulted in the formulation of a conceptual model of the aquifer which is consistent with observations, and which can account for its behavior when subjected to pumping.

TABLE OF CONTENTS

LIST OF FIGURES v
LIST OF TABLES viii
NOMENCLATURE ix
ACKNOWLEDGMENTS x

1.0 INTRODUCTION 1

2.0 SITE DESCRIPTION 3
2.1 General 3
2.2 Boreholes 5
2.3 Local Geologic Setting 6

3.0 FRACTURE DESCRIPTION 8
3.1 Regional Fracture Characteristics 8
3.2 Investigation of Subsurface Fracture Characteristics at the Site 13
3.2.1 Borehole Fracture Mapping 13
3.2.2 Tool Description 13
3.2.3 Fracture Detection and Measurement 16
3.2.4 Fracture Distribution 18
3.3 Geophysical Logs and Inferred General Hydrogeologic Structure of the Aquifer 25

4.0 PUMPING TESTS 33
4.1 Instrumentation and Field Procedures 33
4.2 Results and Interpretation 34
4.2.1 General 34
4.2.2 Analysis of Drawdowns in Pumped Wells 38
4.2.3 Evaluation of Wellbore Skin and Skin Effect 43
4.2.4 Analysis of Drawdowns in Observation Wells 49

5.0 DOWNHOLE FLOWMETER TESTS 56
5.1 Approach 56
5.2 Field Procedure 57
5.3 Data Analysis and Results 59
5.4 Effects of Turbulence During Flowmeter and Pump Tests 66

6.0 NUMERICAL MODELING 69
6.1 Purpose 69
6.2 Code Description 69
6.3 Grid Layout and Code Verification 70
6.4 Assignment of Properties to Model Grid 73
6.5 Simulation Results 74

7.0 SUMMARY AND CONCLUSIONS 79
7.1 Suggestions for Future Work 81

REFERENCES 83
APPENDIX 1: MEASUREMENTS AND CALCULATIONS OF BOREHOLE FRACTURE PROPERTIES 89
APPENDIX 2: DOWNHOLE FLOWMETER MEASUREMENTS 95

LIST OF FIGURES

Figure 2.1. Topographic map of site and surrounding area. 4

Figure 2.2. Schematic map showing borehole locations. Distances shown in feet. 4

Figure 2.3. Regional geologic map. 7

Figure 2.4. General surface expression of fractures in the central Sierra Nevada. 11

Figure 3.1. Diagram of ATV logging system. 14

Figure 3.2. Portion of ATV image from well 0-0. Note that these images are the 2nd photocopies of the original Polaroid photographs. 15

Figure 3.3. Determination of dip angle and azimuth of fracture from the ATV log. 16

Figure 3.4. Stereonets of mapped fractures in wells 0-0, SE-1, and SW-1 (Schmidt equal-area, lower hemisphere, polar projections). North is 1982 true north. 19

Figure 3.5. Density plot stereonet of mapped fractures from all three wells (Schmidt equal-area, lower hemisphere, polar projection). North is 1982 true north. 20

Figure 3.6. Definition of fracture sets. Set A=unloading fractures. Set B&C=tectonic fractures. 22

Figure 3.7. Fracture spacing histograms for sets A, B, and C. 23

Figure 3.8. Fracture spacing histograms for sets A, B, and C. Spacing class <2m. 24

Figure 3.9. a. Caliper logs of wells SW-1, 0-0, and SE-1; b. Apparent resistivity logs of wells SW-1, 0-0, and SE-1. 27

Figure 3.10. Density plot stereonet of fractures occurring at depths where apparent resistivity < 700 ohm-m in wells SW-1, SE-1, and 0-0 (Schmidt, equal-area, lower hemisphere, polar projection). North is 1982 true north. 29

Figure 3.11. Profile of apparent resistivity <700 ohm-m in all wells. 31

Figure 3.12. Profile of apparent resistivity <700 ohm-m and flow zones in all wells, and inferred general hydrogeologic structure of aquifer. 32

Figure 4.1. Log-log plot of drawdown vs. time in wells during test RAYP22. 35

Figure 4.2. Log-log plot of drawdown vs. time in wells during test RAYP3. 35

Figure 4.3. Log-log plot of drawdown vs. time in wells during test RAY12. 36

Figure 4.4. Semilog plot of drawdown vs. time in pump well SE-1. 39

Figure 4.5. Semilog plot of drawdown vs. time in pump well SW-1. 39

Figure 4.6. Semilog plot of drawdown vs. time in pump well 0-0. 40

Figure 4.7. Match of analytical solution that considers effective radius and impermeable boundary to drawdown in pump well SE-1. 47

Figure 4.8. Match of analytical solution that considers effective radius and impermeable boundary to drawdown in pump well 0-0. 47

Figure 4.9. Match of analytical solution that considers effective radius and impermeable boundary to drawdown in pump well SW-1. 48

Figure 4.10. Theis curve match to drawdown in well 0-0 during test RAY12. 51

Figure 4.11. Theis curve match to drawdown in well SW-1 during test RAY12. 51

Figure 4.12. Theis curve match to drawdown in well SW-2 during test RAY12. 52

Figure 4.13. Theis curve match to drawdown in well SW-4 during test RAY12. 52

Figure 4.14. Match of analytical solution that considers impermeable boundary to drawdown in well 0-0 during test RAYP22. 53

Figure 4.15. Match of analytical solution that considers impermeable boundary to drawdown in well SE-1 during test RAYP3. 54

Figure 4.16. Match of analytical solution that considers impermeable boundary to drawdown in well 0-0 during test RAYP3. 54

Figure 5.1. Schematic of flowmeter test configuration. 58

Figure 5.2. Semilog plot of drawdown vs. time in well SE-1 during test FLOW SE-1. 60

Figure 5.3. Semilog plot of drawdown vs. time in well SW-1 during test FLOW SW-1. 60

Figure 5.4. Semilog plot of drawdown vs. time in well 0-0 during test FLOW 0-0: B. 61

Figure 5.5. Relationship between Q_i and flow measurements made at two different depths. 62

Figure 5.6. Average horizontal hydraulic conductivity with depth in well SE-1. 64

Figure 5.7. Average horizontal hydraulic conductivity with depth in well SW-1. 65

Figure 6.1. Two-dimensional grid of nodes and elements used in TRINET simulation. The figure shows the distribution of the line elements. Nodes are located at the intersections of these elements. 71

Figure 6.2. Comparison of numerical and analytical solution for drawdown in pumped well (r=0.0826 m), and in an observation well. 72

Figure 6.3. Schematic of the basic distribution of properties assigned to the numerical model. 73

Figure 6.4. Schematic of model that accounts for observed drawdowns during tests RAYP22 and FLOW 0-0. 74

Figure 6.5. Simulated drawdown at pumped well SE-1 compared to actual drawdown during test RAYP22. 75

Figure 6.6. Simulated drawdown at observation well 0-0 compared to actual drawdown during test RAYP22. 75

Figure 6.7. Simulated drawdown at pumped well 0-0 compared to actual drawdown during test FLOW 0-0. 76

Figure 6.8. Schematic of numerical model in which all three wells are enclosed in a zone of constant transmissivity Ti. 77

Figure 6.9. Simulated drawdown in pumped well SE-1 using numerical model shown in Figure 6.8 compared to actual drawdown during test RAYP22. 77

Figure 6.10. Simulated drawdown in observation well 0-0 using numerical model shown in Figure 6.8 compared to actual drawdown during test RAYP22. 78

LIST OF TABLES

Table 2.1. Borehole specifications. 6

Table 3.1. Summary of orientation statistics of each fracture set. 22

Table 4.1. Specifications of pumping tests. 33

Table 4.2. Summary of drawdown analyses for all pump tests. 55

Table 5.2. Transmissivity values used for flowmeter analysis. 62

Table 5.3. Calculated flow entering different depth intervals during flowmeter test in well SE-1. 64

Table 5.4. Calculated flow entering different depth intervals during flowmeter test in well SW-1. 64

Table 5.5. Range of possible flow rates and transmissivities over different depth intervals in well 0-0. 65

Table 5.6. Reynolds number associated with flow from fractures. 67

NOMENCLATURE

b_i	depth interval i, L
b_f	fracture aperture, L
D	diameter of wellbore, L
E_i	exponential integral
g	gravitational acceleration , $L^2 \bullet T$
ΔH_{skin}	change in hydraulic head across skin zone, L
K	horizontal hydraulic conductivity, $L \bullet T^{-1}$
K_i	average horizontal hydraulic conductivity over the depth interval i, $L \bullet T^{-1}$
k	permeability of formation, $L \bullet T^{-1}$
k_s	permeability of skin zone, $L \bullet T^{-1}$
Q	discharge, $L^3 \bullet T$
Q_i	flow from the ith depth interval into the well, $L^3 \bullet T$
R_e	Reynold's number, 1
r_b	radial distance to impermeable boundary, L
r_e	effective wellbore radius, L
r_i	radial distance to image well, L
r_s	radius of skin zone, L
r_w	wellbore radius, L
S	storativity, 1
s	drawdown, L
s_k	skin factor, 1
T	transmissivity, $L^2 \bullet T$
T_i	transmissivity over depth interval i, $L^2 \bullet T$
t	time, T
t_1	time corresponding to the fictitious intersection point of 2 straight lines on semilog drawdown plot, T
V_w	flow velocity entering the wellbore, $L \bullet T$
ν	kinematic viscosity, $L^2 \bullet T$
z	depth, L
α	constant of proportionality, 1

ACKNOWLEDGMENTS

I sincerely thank Dr. Sally Benson of Lawrence Berkeley Laboratory for allowing me the opportunity to participate in this work. I greatly appreciate the freedom Sally allowed me to explore my own ideas. The study, and the completion of this Master's thesis, have been my greatest learning and thinking experience as a graduate student, and I am grateful to everyone who helped make this possible, including my family.

Technical discussions with my thesis advisors, Professor Nicholas Sitar, Professor T. N. Narasimhan, and Dr. Sally Benson, and their reviews of this document, made this experience a rich one. I appreciate Professor Sitar's repeated critical reviews of this thesis, and for the improved quality of work that resulted because of them.

Fred Paillet of the U. S. Geological Survey in Denver aided me in the mapping of the subsurface fractures from the ATV logs, and he answered questions I had regarding the downhole geophysical logs. Barbara Allen, Joyce Dey, and Ticie Taylor, also of the Geological Survey, helped me obtain this data.

Several colleagues in the Earth Sciences Division at Lawrence Berkeley Laboratory contributed to this work. Many thanks go out to Chris Doughty and Stuart Segan for their help with the computer modeling. If it were not for their extreme generosity, the numerical modeling shown in section 6 would not have been possible. Ray Solbau was instrumental in helping me obtain the hydrologic data. I am grateful to Ray for sharing his expertise with me. John Clyde and Sally Benson also helped collect the hydrologic data. Preston Holland, Kenzi Karasaki, Tetsu Tokunaga, and Peter Zawislanski provided valuable technical advise. Kenzi is also responsible for developing the field site, and I thank him for allowing me easy access to it.

Administrative technicalities were virtually nonexistent, thanks to the expertise of Mary Cook of the Department of Civil Engineering.

Funding for this work was provided by the Environmental Protection Agency under Interagency Agreement No. DW-89935185, through U. S. DOE Contract No. DE AC03-76SF00098. Thanks are due to Steve Kraemer, the EPA project manager, for his oversight and support.

Finally, I thank you, Lara, for putting up with all of this.

1.0 INTRODUCTION

The methodologies and findings of a field investigation of a fractured granitic rock groundwater system at a field site in the western foothills of the Sierra Nevada, California, are presented herein. This investigation is a part of a larger study aimed at improving the effectiveness of pump-and-treat remediation schemes in fractured rock aquifers.

The extraction and treatment of groundwater is the most common method used to remediate groundwater contamination. Due to the complexity of contaminant flow and incomplete and/or simplified characterization efforts, extraction of contaminants is often problematic. The extraction of contaminants in fractured crystalline rock systems is typically more difficult than in unconsolidated porous materials because the flow regime is usually more complex and harder to characterize and simulate (Mackay and Cherry, 1989).

The major pathway for groundwater flow and contaminant migration in crystalline rocks is through fractures. The most significant factors affecting the flow characteristics within fractures are the aperture, orientation, and degree to which individual fractures are mineral-filled, as well as their interconnection and spacing. Additionally, the extent to which contaminants can migrate will tend to be a function of depth because fracture apertures are highly stress-dependent (Gale, 1982), and because the in-situ stress typically, but not always, increases with depth. Because the transmissivity of a fracture is approximately proportional to its aperture cubed, the flow regime has the potential of being poorly understood if only a few relatively large fractures are not detected. Also, the intergranular porosity in crystalline rocks is very low, and the permeability of the matrix is very low relative to that of the fractures. Thus,

contaminants are mainly transported within the fracture network. As a result, they migrate faster and are more unevenly distributed than contaminants in porous systems under comparable seepage gradients (Fortin, 1988). If the contaminants are present in the fractures for a sufficient length of time, however, they can diffuse into the rock matrix (Mackay and Cherry, 1989).

The nature of contaminants also significantly influences their migration characteristics. For example, non-aqueous phase liquids (NAPL's) that have densities greater than the groundwater will sink and eventually get caught in dead-end fractures, as well as contaminate lower portions of the fracture network. Additionally, they have the potential of migrating in directions very different from that of the groundwater depending upon the fracture network orientation. At remediation sites in Massachusetts and Rhode Island, for example, investigators concluded that the major contaminant flow direction in the bedrock aquifer was controlled by the orientation of fractures and the slope of the bedrock surface (Di Nitto *et al.*, 1982). This behavior, coupled with the diffusion of dissolved portions of the contaminants into the matrix, will severely hamper the effectiveness of a remediation effort because little or no water will flush through the dead-end fractures or through the rock matrix (Mackay and Cherry, 1989).

In this study, the emphasis was on the hydrogeologic characterization of the fractured rock aquifer. The work and findings described in this report constitute a preliminary assessment and analysis of the site. Most of the analyses are based on geophysical logs and hydrologic tests collected and performed in 3 of the 9 boreholes at the site. Specifically, the study consisted of the following steps:

1) Borehole televiewer logs were used to measure the orientation and apparent aperture of individual fractures. Based on the spatial distribution of the mapped fractures

and on an understanding of the regional fracture characteristics and geologic history, the fractures were subdivided into several fracture sets.

2) A conceptual model of the flow system was formulated by analyzing the relationships between borehole geophysical properties and these fracture sets.

3) Pumping tests were conducted, and the results were used to assess the overall hydrologic properties of the aquifer. In addition, the locations of some relatively high and low hydraulic conductivity zones were inferred from analysis of these tests.

4) A numerical model was constructed in order to test whether or not the inferred hydrogeologic structure could account for the observed behavior of the system when subjected to pumping.

2.0 SITE DESCRIPTION

2.1 General

The experimental work described here was conducted at the Raymond Quarry Field Site, which is operated by Lawrence Berkeley Laboratory and U. S. Geological Survey, under the sponsorship of Office of Civilian Radioactive Waste Management of the Department of Energy.

The site is situated in the western foothills of the central Sierra Nevada, California, approximately 60 km (37 mi) south of Yosemite Valley and about 5 km (3 mi) southeast the town of Raymond. This site was selected in part because of its relatively easy access, and because it is located near an abandoned rock quarry. Mapping of the exposed fractures in this quarry could be useful in identifying the nature of fracturing at the site. Because the site is somewhat isolated, there is freedom to carry out different

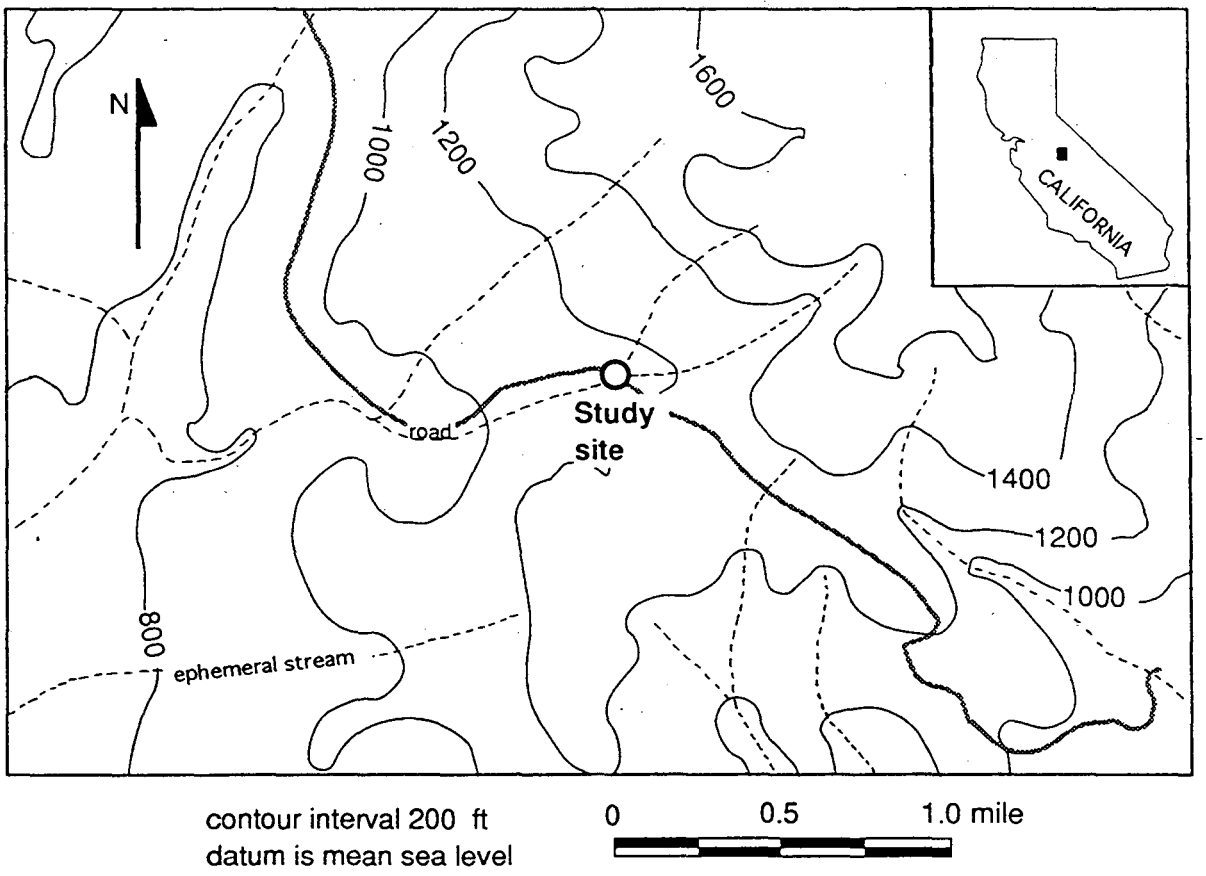

Figure 2.1. Topographic map of site and surrounding area.

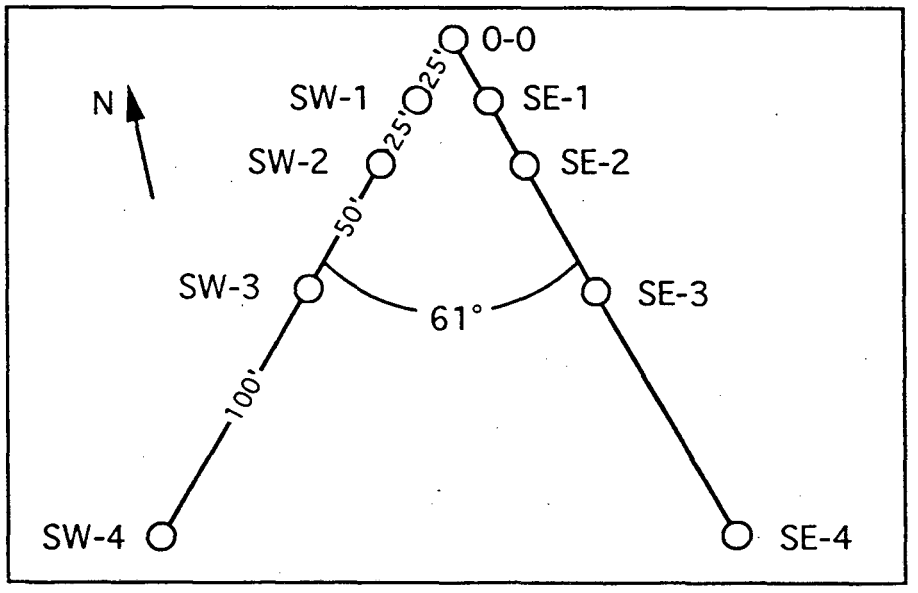

Figure 2.2. Schematic map showing borehole locations. Distances shown in feet.

types of experiments without interfering with other activities. The local relief is subdued, with altitude ranging from 245 to 610 m (800 to 2000 ft) above mean sea level (Fig. 2.1). Nine vertical boreholes spaced no more than 61 m (200 ft) apart and ranging in depth from 75 to 90 m (245 to 295 ft) below ground surface penetrate the shallow granitic bedrock (Fig. 2.2). The bedrock is overlain by a thin layer of soil and regolith which is approximately 8 m thick near the well field, and it is exposed in frequent outcroppings along hillsides and in stream beds. Annual precipitation varies widely from year to year, but it is on the order of 50 cm/yr (20 in/yr). More than 75 percent of the precipitation falls in the winter (Mitten *et al.*, 1970). The potentiometric surface is generally shallow, and during the period of this study it was about 5 m (15 ft) below ground surface. The surrounding area is dissected by several ephemeral streams, and groundwater flow is generally to the west (Mitten *et al.*, 1970).

2.2 Boreholes

Boreholes were drilled at the site between March and May, 1992 with an air-percussion drill. No intact core samples could be collected because the cuttings were usually powdered or finely crushed. The maximum relative difference in surface elevation between the wells is less than 2.5 m (8 ft). Driller's logs indicate that relatively unweathered granite is located beneath less than 8 m (25 ft) of soil and regolith. Steel casings were installed in each hole to a depth between 7 to 15 meters below ground surface, and the lower part of each borehole was left unscreened and uncased. Table 2.1 lists the borehole specifications.

Table 2.1. Borehole specifications.

Borehole	Total Depth [m]	Casing Depth [m]	Casing Diameter [m]	Nominal Uncased Borehole Diameter [m]	Elev. of top of casing relative to 0-0 [m]
0-0	76.2	12.2	0.168	0.17	
SE-1	74.7	15.2	0.168	0.17	-0.384
SE-2	74.4	7.3	0.254	0.25	-1.049
SE-3	88.4	8.1	0.254	0.17	-0.989
SE-4	88.1	11.6	0.254	0.16	-0.250
SW-1	76.2	7.9	0.168	0.17	-0.732
SW-2	89.9	9.0	0.254	0.25	-2.014
SW-3	82.0	7.9	0.254	0.17	-0.839
SW-4	90.1	8.7	0.254	0.17	-0.263

2.3 Local Geologic Setting

Two plutonic rock masses of the larger Sierra batholith comprise the bedrock in the vicinity of the site (Figure 2.3). The granodiorite of Knowles is a light-gray, equigranular, and medium-grained rock. It is generally spatially isotropic with respect to mineral composition and texture, and foliations are generally not observed. Because of these characteristics the rock has been extensively quarried and widely used as a building stone in some of the large cities of California. Isotopic dating indicates that the granodiorite is approximately 111 million years old. The characteristics of the tonalite of Blue Canyon are more varied regionally, but near the site it is a medium-grained, dark gray rock, and it is generally well foliated. Unlike the granodiorite, it contains conspicuous hornblende prisms and generally contains more biotite mafic minerals and less potassium feldspar by volume than the granodiorite. Isotopic dating indicates that the tonalite is approximately 114 m.y.o. (Bateman and Sawka, 1981; Bateman *et al.*, 1982).

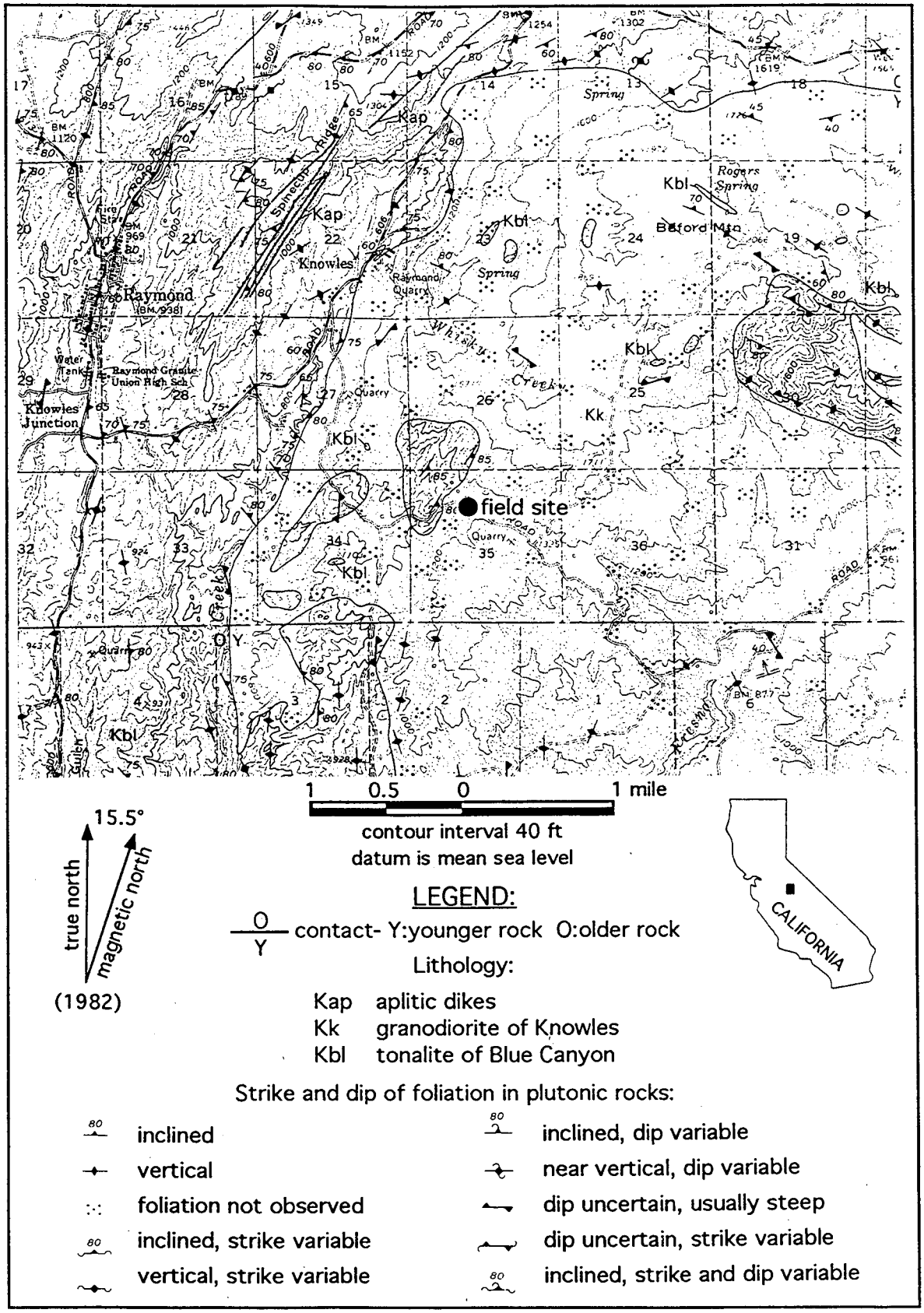

Figure 2.3. Regional geologic map (modified from Bateman *et al.*, 1982).

The outcrop of the contact between the two plutons is located less than 0.5 km (0.3 mi) from the well field. Given the shallow depth of regolith and soil, it is believed that the wells are situated in the granodiorite. However, it is not yet known whether or not the tonalite intersects the wells at greater depths, mainly because borehole core samples are not available. Pegmatitic and aplitic dikes are exposed in the frequent outcroppings along hillsides and in stream beds.

3.0 FRACTURE DESCRIPTION

3.1 Regional Fracture Characteristics

The first step in assessing the nature of flow in a fractured rock system is the analysis of the spatial distribution and physical properties of the fractures themselves. Prior to the investigation of fractures at the site, an appreciation for the regional geologic history, the characteristics of the fracture systems present, and the processes responsible for their formation is necessary. Since the fractures found at the site are likely to be part of the larger, regional system, such an understanding may provide clues as to what properties a particular fracture or fracture set might possess, and/or the relationships which can be expected to be seen or to which special attention should be devoted to.

The word fracture is used here as a collective term for all types of discontinuities including joints, fissures, shear zones, and faults. In general, three different systems of fractures are prevalent throughout the Sierra Nevada: two nearly vertical dipping sets that strike almost orthogonal to one another in a northeasterly and northwesterly direction, and a relatively shallow and young subhorizontal set that produces the sheet-like structure typical on many of the high ridges in the Sierran interior (Norris and Webb, 1976). Because these fractures crosscut the subvertical joints, do not contain hydrothermal

deposits, and are found at depths ranging from meters to no more than several hundreds of meters below the surface, there is little doubt that they are exfoliation fractures which resulted from pressure relief during erosional unloading (Segall and Pollard, 1983a,b; Billings, 1972). In contrast, the geologic history of, and the processes responsible for the formation of the near vertical fractures has proven to be complicated and difficult to decipher. It has long been acknowledged that they formed in response to tectonic forces. The rectilinear arrangement of near vertical fractures is a characteristic indicative of a tectonic origin (Chernyshev and Dearman, 1991). Additionally, many of the fractures are strike-slip faults, and the direction of compressive stresses inferred from their arrangement is consistent with plate tectonic theories regarding the geologic history of western North America (Dott and Batten, 1988). Isotopic dating of the central Sierran plutons indicates that they were emplaced between the late Mesozoic to early Cenozoic (between 135 and 70 m.y.a.) and provides a maximum age for the fractures. Because they are filled with mineral precipitates such as quartz, epidote, and chlorite, some investigators suggested that the near-vertical fractures must have formed during the emplacement of the plutons (e.g., Balk, 1937; Mayo, 1941). Others suggested that they must have formed after all of the plutons had cooled sufficiently enough to allow brittle failure to occur, since the fractures cut across interpluton boundaries with little change in trend (e.g., Bateman and Wahrhaftig, 1966; Lockwood and Moore, 1979). More recent work has suggested that the subvertical fractures formed in response to a series of individual tectonic events.

Prominent lineaments observable on aerial photographs display the large-scale structure of the two near-vertical sets, namely their rectilinear arrangement and strike-slip faulting. The northwesterly trending set is right-laterally offset, and the northeasterly set is left-laterally offset. Detailed work on these features in the central Sierra, where 80 million year old plutons are exposed, has revealed that there is a more complex internal

structure to these sets (Lockwood and Moore, 1979; Segall and Pollard, 1983a,b; Segall and Simpson, 1986; Martel *et al.*, 1988). At a site about 80 km (50 mi) east of Raymond, Segall and Pollard (1983a,b) observed that the northeasterly trending set is comprised of several smaller scale features: east-northeasterly striking microfaults with left-lateral offset ranging from a few centimeters to tens of centimeters, and east-northeasterly and northeasterly striking joints that are typically less than 1 cm wide (Figure 2.4). The northeasterly striking joints propagate off the ends of the east-northeasterly microfaults. By definition, the joints do not exhibit any offset parallel to their surfaces. Both types of fractures are completely mineral filled with chlorite, epidote, and/or quartz. Larger fault zones which are up to several hundred meters to kilometers in length, and which appear as the prominent lineaments on aerial photographs, are parallel to the trend of the microfaults and east-northeasterly striking joints. These lineaments are commonly marked by brush and trees or narrow depressions of extensively weathered angular blocks of rock, and this makes them appear as eroded gullies. They provide channels for surface water and potentially for groundwater as well (Lockwood and Moore, 1979; Segall and Pollard, 1983a). Slickensides on the surfaces of the microfaults and on the boundary faults of the lineaments plunge several degrees to the west (Lockwood and Moore, 1979; Martel *et al.*, 1988), suggesting that the strike-slip motion occurred prior to the westward tilting of the Sierran block during the late Cenozoic (Lockwood and Moore, 1979).

Also present are right-laterally sheared zones that trend northwesterly and which bend both the microfault and joint traces about 30° clockwise from their preferred northeasterly trend (Fig. 2.4). Within these kink bands (Segall and Pollard, 1983b) the density of joints and microfaults is greater than in regions outside the kink bands. They occur only in areas where greater than average strike-slip motion along the microfaults is present. They trend along or parallel to the previously offset dikes that trend to the north

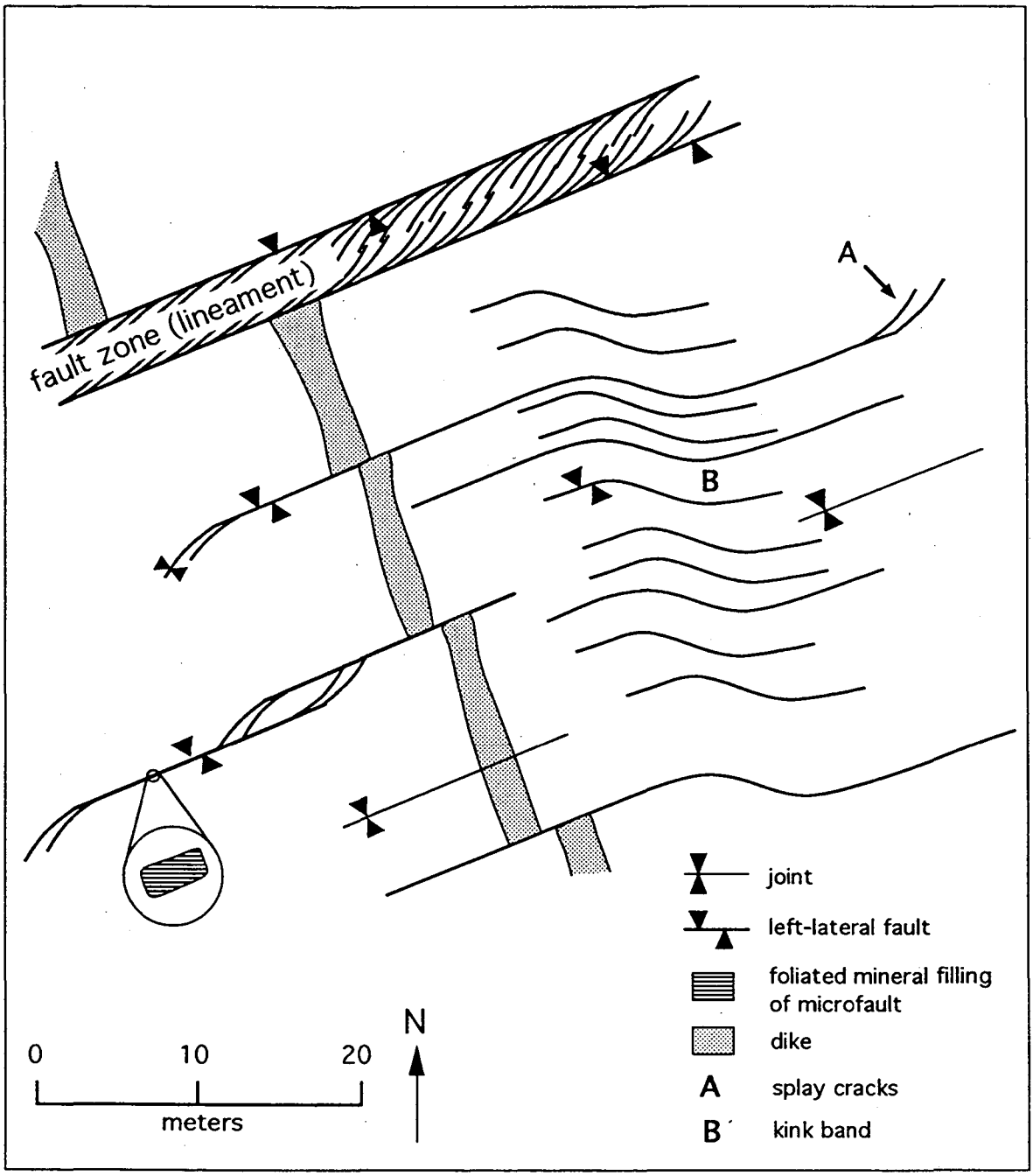

Figure 2.4. General surface expression of fractures in the central Sierra Nevada (modified from Martel *et al.*, 1988).

to northwest, but are offset by, or do not cross the larger fault zones (Segall and Pollard, 1983b; Davies and Pollard, 1986; Martel *et al.,* 1988). Martel *et al.* (1988) also noted a northwest-striking set of subvertical joints that are not filled with hydrothermal minerals. These cross the larger fault zones, and are therefore the youngest tectonic fractures.

Lockwood and Moore (1979) noted that the direction and arrangement of lineaments in the Sierra Nevada strongly parallel those formed during the late Cenozoic in the Basin and Range province. They suggested that some of the lineaments in the Sierra are the products of this later tectonic event. Perhaps the northwesterly trending fracture set that does not appear to be infilled with hydrothermal materials, as noted by Martel *et al.* (1988), is a product of this later deformation when the rock was brittle.

Although the inferences detailed above are based on observations in the central Sierras, mapping of major strike-slip faults throughout western California reveals that discontinuous parallel or subparallel segments are internal to their structure (Martel *et al.*, 1988). Dikes offset by microfaults were noted on surface exposures at the Raymond site, for example (Zawislanski, oral comm., 1993).

Because the events responsible for the near vertical fractures in the plutons occurred after their emplacement, major differences between the fracture characteristics in the tonalite and granodiorite near the site probably do not exist. Huber (1987) observed, however, that the composition and texture of plutonic rocks in Yosemite National Park is related to the spacing of joints within them. Generally, rocks with relatively low silica content (e.g. tonalite and diorite) or those that are finer grained have more closely spaced joints than the more siliceous (e.g. granite and granodiorite) or coarser grained rocks. The fact that the site is located very close to the contact between the tonalite and granodiorite may therefore influence its hydrogeologic structure.

3.2 Investigation of Subsurface Fracture Characteristics at the Site

3.2.1 Borehole Fracture Mapping

Detailed mapping of individual subsurface fractures and fracture zones was performed using acoustic borehole televiewer logs of wells 0-0, SE-1, and SW-1. The determination of the orientation and dip of individual fractures and fracture zones, as well as an approximate measure of their associated apertures, was made from inspection of these logs. The logs were made in August, 1992 by the U. S. Geological Survey of Denver, Colorado. As noted earlier, determination of fracture infilling properties was not possible because rock cores from wells were not available. Instead, the discretization of the observed fracture distribution into particular fracture sets was made based on their observed orientations and spacing characteristics, and on an understanding of the regional geology and geologic history.

3.2.2 Tool Description

An acoustic borehole televiewer (ATV) produces an image of the acoustic reflectivity of a borehole wall. Figure 3.1 shows a schematic of the logging system. As the probe is pulled up the borehole, a piezoelectric transducer is rotated at 3 revolutions per second, and it is pulsed between 800 and 2000 times per second. The emitted acoustic energy is reflected from the borehole wall and received by the same transducer, which sends the signal to an oscilloscope at land surface. When the transducer rotates past magnetic north, a flux-gate magnetometer signals a sweep on the oscilloscope. Therefore, a complete 360° rotation of the transducer is represented by a complete scanline across the oscilloscope screen. Because the amplitude of the reflected acoustic signal will be lower where discontinuities and irregular surfaces are present, and because the brightness of the oscilloscope trace is proportional to this amplitude, fractures and

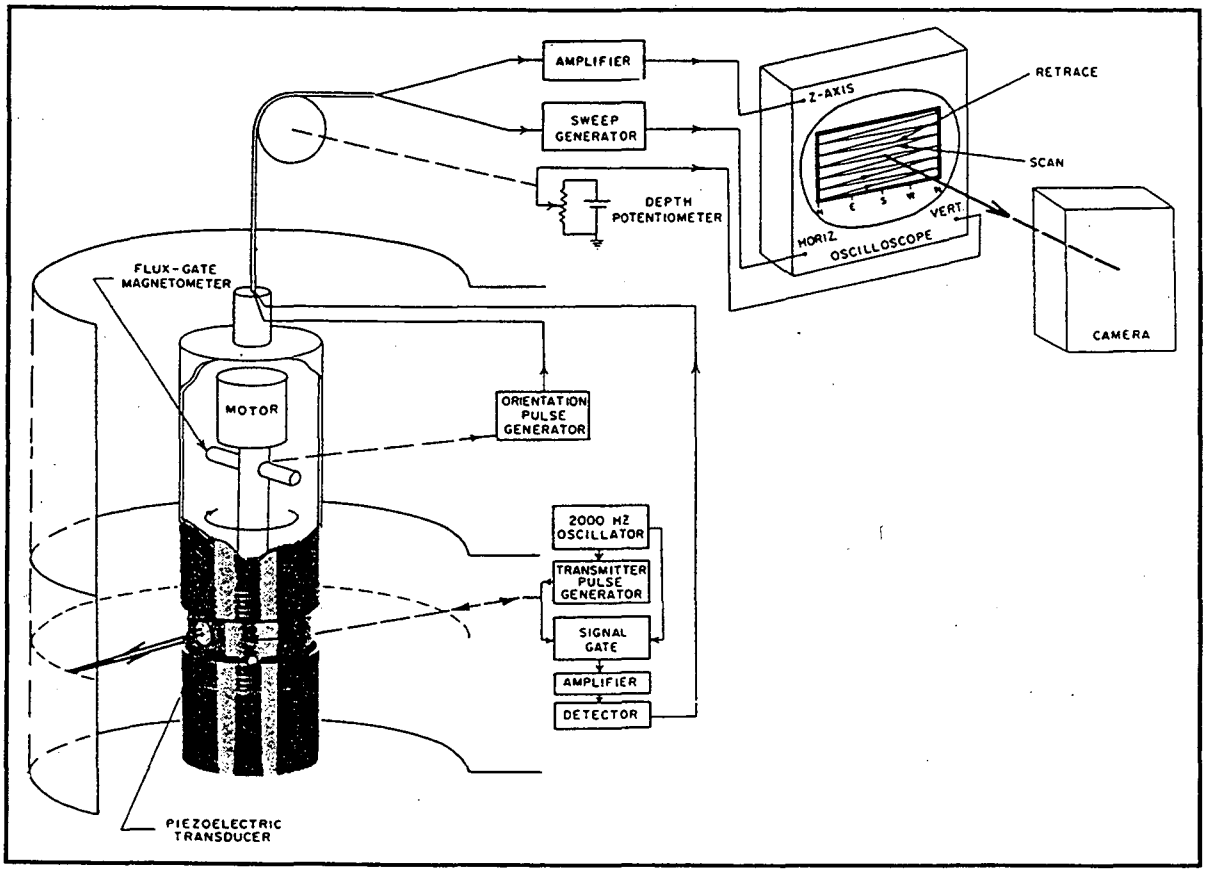

Figure 3.1. Diagram of ATV logging system (from Zemanek *et al.*, 1969). Reprinted with permission from the Society of Petroleum Engineers.

other openings will appear as dark areas on the oscilloscope screen. Since the tool is moved vertically simultaneously with transducer rotation, a spiral strip of the borehole wall is probed, and a fracture plane that intersects the borehole at an angle other than 90° will ideally produce a sinusoidal image on the oscilloscope screen (Zemanek *et al.*, 1969; Keys, 1990). The rate of ascent of the probe in this study was 5 feet per minute. A Polaroid camera was used to record the oscilloscope image, and the photographs were taped together to form a continuous log. Figure 3.2 shows a portion of the ATV log image of well 0-0.

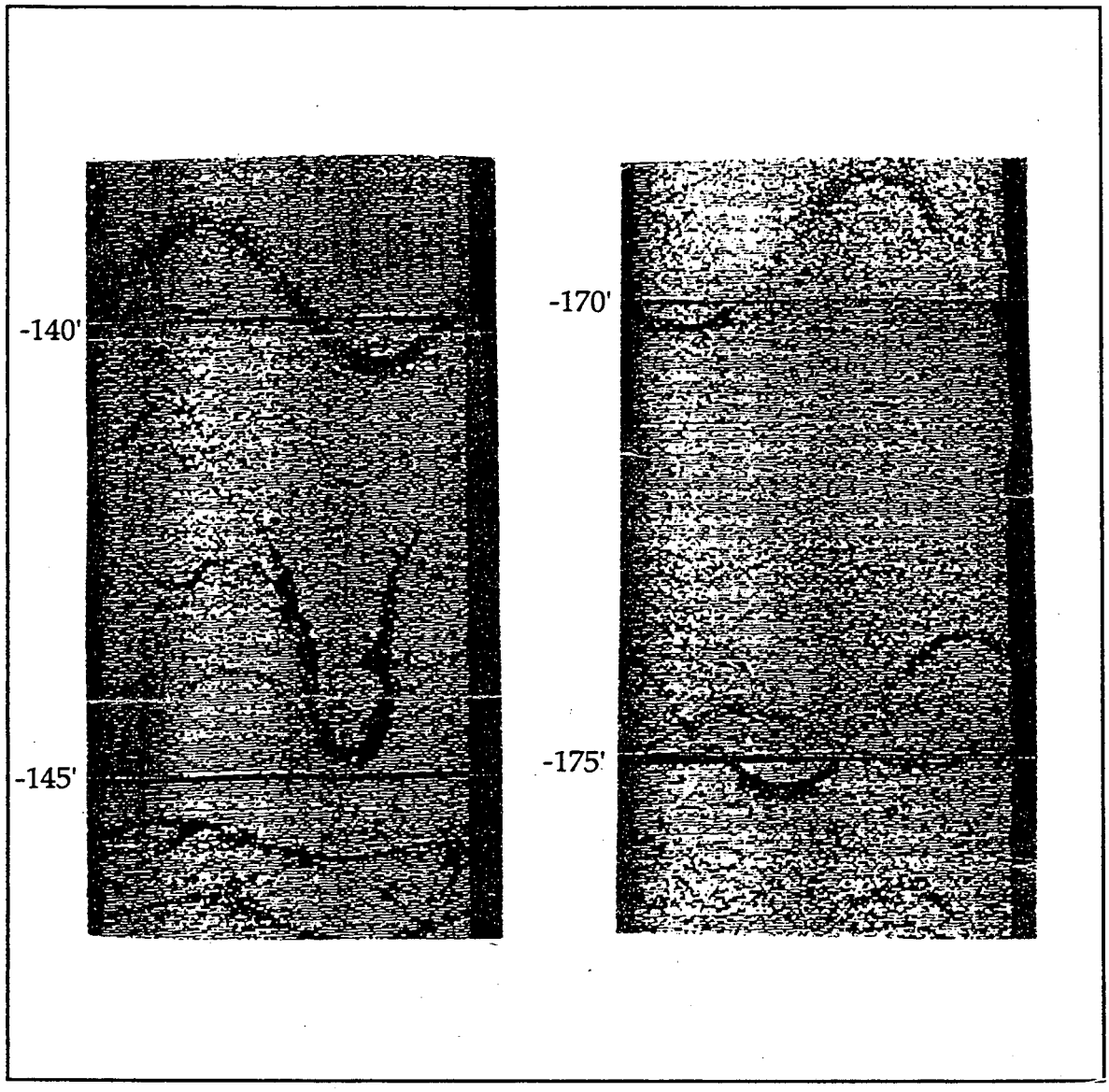

Figure 3.2. Portion of ATV image from well 0-0. Note that these images are the 2nd photocopies of the original Polaroid photographs.

3.2.3 Fracture Detection and Measurement

Under ideal conditions the sensitivity of the ATV is great enough to detect open fractures in crystalline rocks with apertures greater than 1mm (Davison *et al.*, 1982). Closed or completely filled fractures are not detected unless there is a difference between the acoustic reflectivity of their infilling and that of the intact borehole wall. The determination of fracture dip and azimuth of individual fractures from the ATV log is relatively straightforward (Fig. 3.3). The dip angle is simply the arc tangent of H/D. Since the edges of the oscilloscope image represent magnetic north, a 360° scale constructed to fit the width of the image can be used to determine the dip azimuth. Similarly, a scale constructed to fit the actual 5 ft borehole length represented by each oscilloscope image can be constructed.

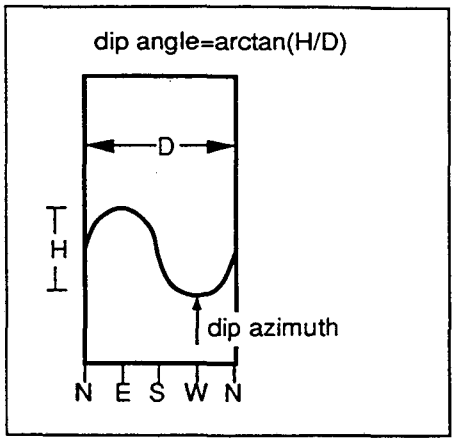

Figure 3.3. Determination of dip angle and azimuth of fracture from the ATV log.

The problematic aspect of the measurements arises because the fractures are inevitably disturbed by the drilling process and/or because fractures intersecting the borehole wall do not always form a sinusoidal image. Concentration of stress at the fracture-borehole intersection during the passage of the drill bit often causes the rock adjacent to fractures to break out. This in turn increases the apparent thickness of the fracture on the ATV log (Paillet *et al.*, 1985). For nearly vertical fractures, chips of rock

are frequently broken out near the upper and lower fracture-borehole intersection. This gives the appearance that the fracture is more steeply dipping than it actually is. Thin wedges of rock situated between closely spaced subparallel fractures that are either open or mineral filled can be broken out to give the appearance of a single large, open, and nearly horizontal fracture zone, the orientation and dip of which cannot be easily determined. Vertical deviation of the borehole can further complicate feature determination (Davison *et al.*, 1982). Geophysical logs indicate that all the boreholes at the site are essentially vertical and that the three boreholes investigated here deviate less than 3° from the vertical. No correction was made for this deviation, since the purpose of measuring the fractures was to examine the overall general structure, and since the relative errors associated with the measurements are of the same order as the deviation.

To verify the detectability limit of the ATV, a television camera log and the ATV log of well 0-0 were compared, and it was found that all fractures were recorded by the ATV. Using the Polaroid pictures of the oscilloscope, four measurements were taken of each fracture trace: 1) the elevation of the middle of the trace at its minimum depth, 2) the elevation of the middle of the trace at its maximum depth, 3) the dip direction, and 4) an average apparent aperture thickness, taken as an approximate average over the entire trace. Measurements were made in English units since the photographs were marked at 5 ft intervals. Measurements 1 and 2 were taken with a standard ruler with markings every 1/10 inch. Because the vertical scale of the photos is 2.5in/5ft, a 0.20 ft elevation difference in the borehole measures as 0.10 inches on the photo. Interpolations were made to the nearest 0.05 in. (0.1 ft). A 360° scale with markings every 10° was used to measure the dip angle to the nearest 10°. To determine the dip angle as it is shown in Fig. 3.3, H was taken as the difference between measurements 1 and 2. A nominal borehole diameter of 6.5 inches was used for D. The measurements and calculations, and the uncertainties of these calculations are listed in Appendix 1.

The above calculations were not possible for all fractures, however. Only one or two of the measurements were obtainable on traces that were not continuous across the entire borehole wall, for example. Several vertical fractures intersected the wells, and these do not show up as sinusoidal images on the ATV log. These fractures pierce the borehole over a short distance and therefore appear as oval traces with a major axis in the vertical direction. The azimuth of this axis was taken as the dip azimuth of these fractures.

3.2.4 Fracture Distribution

The ATV logs showed that a total of approximately 210 fractures intersect the three wells. The fracture traces that were not continuous across the entire televiewer image were difficult or impossible to measure with confidence. Therefore, only the measurements of the 181 continuous fracture traces constitute the fracture database from which the following analyses are based. It should be noted that the incomplete traces did not appear to be of fractures with distinctly different characteristics. They often paralleled other fracture traces, for example, but simply were not distinct enough to measure. A stereonet projection of the mapped fractures in each well is shown in Figure 3.4. A stereonet is a convenient way to display fracture orientation data because it shows both the dip azimuth and the dip angle of individual fractures. Each point on the stereonet represents the intersection of the pole of a fracture plane surface which passes through the center of a sphere with the surface of the lower hemisphere (Billings, 1972). The stereonet shows the intersection as if the surface of the lower hemisphere is viewed from the top of the upper hemisphere. For example, a fracture that dips steeply to the west would plot as a point near the eastern periphery of the stereonet. For the sake of clarity, the lines of longitude and latitude that normally appear on a stereonet have been omitted.

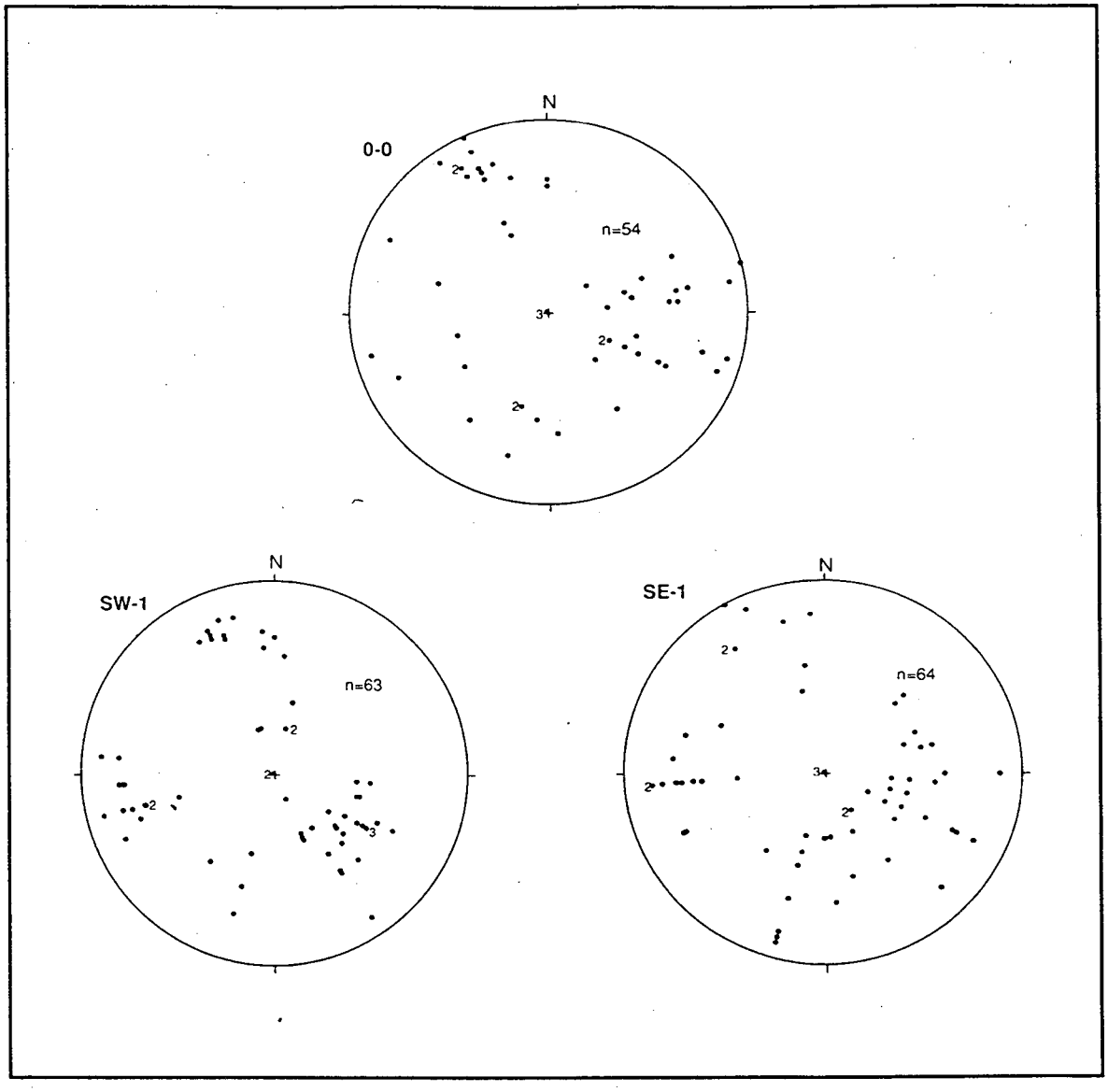

Figure 3.4. Stereonets of mapped fractures in wells 0-0, SE-1, and SW-1 (Schmidt equal-area, lower hemisphere, polar projections). North is 1982 true north.

Since the three wells are located relatively close to one another, and because not all fractures intersecting each well could be identified, inference of the rock-fracture structure near these boreholes is made based on the cumulative observations in all three wells. Figure 3.5 shows the density plot stereonet of mapped fractures from all three wells, and it clearly shows that there are three distinct sets. Those fractures that have a dip angle uncertainty greater than 10° are not included in this plot. These fractures were typically the large, open, and seemingly horizontal fractures mentioned in section 3.2.3. Inclusion of these fractures on the stereonet would give the appearance that many more horizontal fractures are present. Figure 3.5 clearly shows that there are two nearly orthogonal, nearly vertical sets, as well as a set that dips to the west.

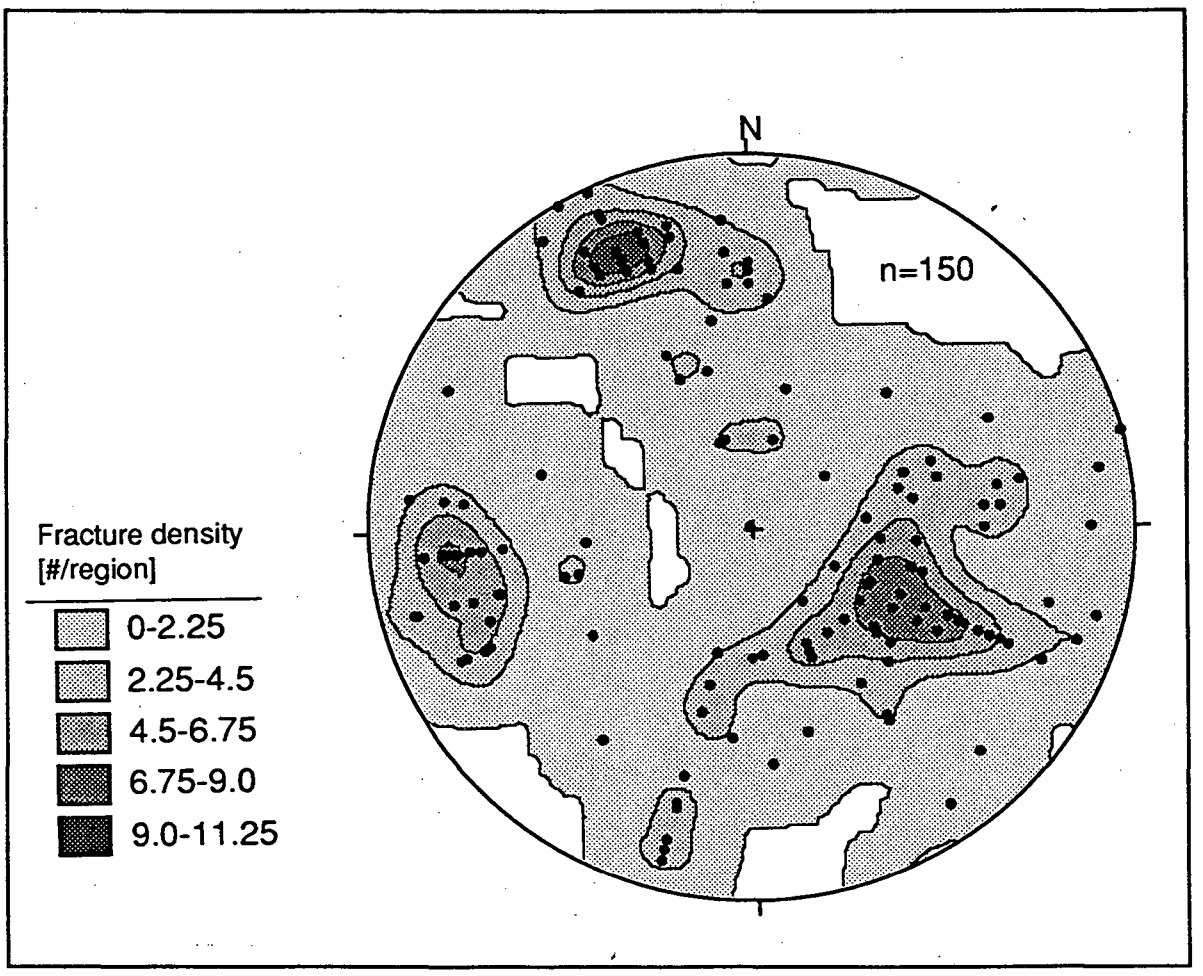

Figure 3.5. Density plot stereonet of mapped fractures from all three wells (Schmidt equal-area, lower hemisphere, polar projection). North is 1982 true north.

Evidence for the presence of the nearly vertical fracture sets is not only expressed in the wells, but also as lineament traces on an aerial photo of the site, and as stream traces on topographic maps (Fig. 2.1). Based on the similarity of the orientation of the mapped subsurface vertical fracture sets to fracture trends present throughout the Sierra, these fractures are believed to be the tectonic fractures described in section 3.1.

The westwardly dipping fractures are unloading, or exfoliation fractures. This conclusion is supported by the fact that 1) these fractures dip subparallel to the surface at the site and unloading fractures form essentially parallel to the topographic surface (Billings, 1972), and 2) unloading fractures constitute the third prominent fracture set observed throughout the Sierra Nevada.

The grouping of all fractures into particular sets is shown in Figure 3.6. The summary of orientation statistics for each set is shown in Table 3.1. Lockwood and Moore (1979) observed that parts of the same steeply dipping microfaults in the Sierra dip in opposite directions. Therefore, the subvertical fractures that strike in the same direction, but which dip in opposite directions are considered to be part of the same set. The spacing distribution of fractures in each set is shown in Figure 3.7 and 3.8.

Priest and Hudson (1976) concluded that unless there is a large predominance of evenly spaced fractures, any combination of evenly spaced, clustered or randomly positioned fractures will lead to a negative exponential spacing distribution. Such a

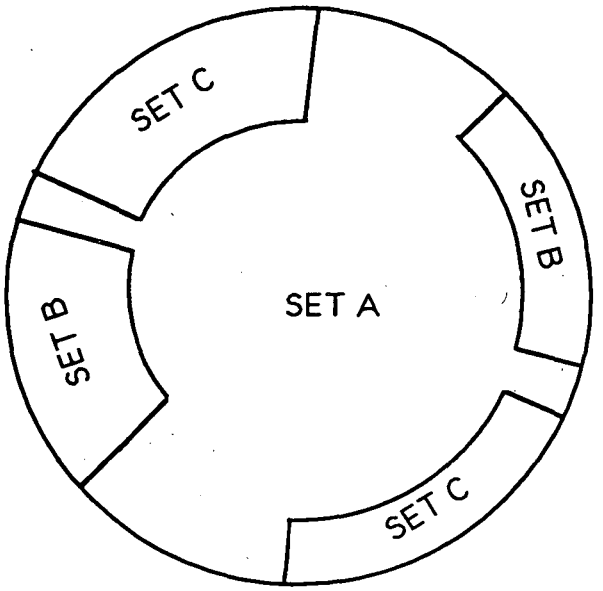

Figure 3.6. Definition of fracture sets. Set A=unloading fractures. Set B&C=tectonic fractures.

Table 3.1. Summary of orientation statistics of each fracture set.

FRACTURE SET	CENTRAL TENDENCY OF STRIKE	CENTRAL TENDENCY OF DIP	MEAN DIP ANGLE	PERCENT OF TOTAL OBSERVED FRACTURES
A	N27E	N63W	40°	42
B	N9W	N81E	70°	15
C	N66E	S23E	71°	17
*	N/A	N/A	N/A	26
			TOTAL # =	210

*Non-continuous fractures or those with measurement error > 10 °.

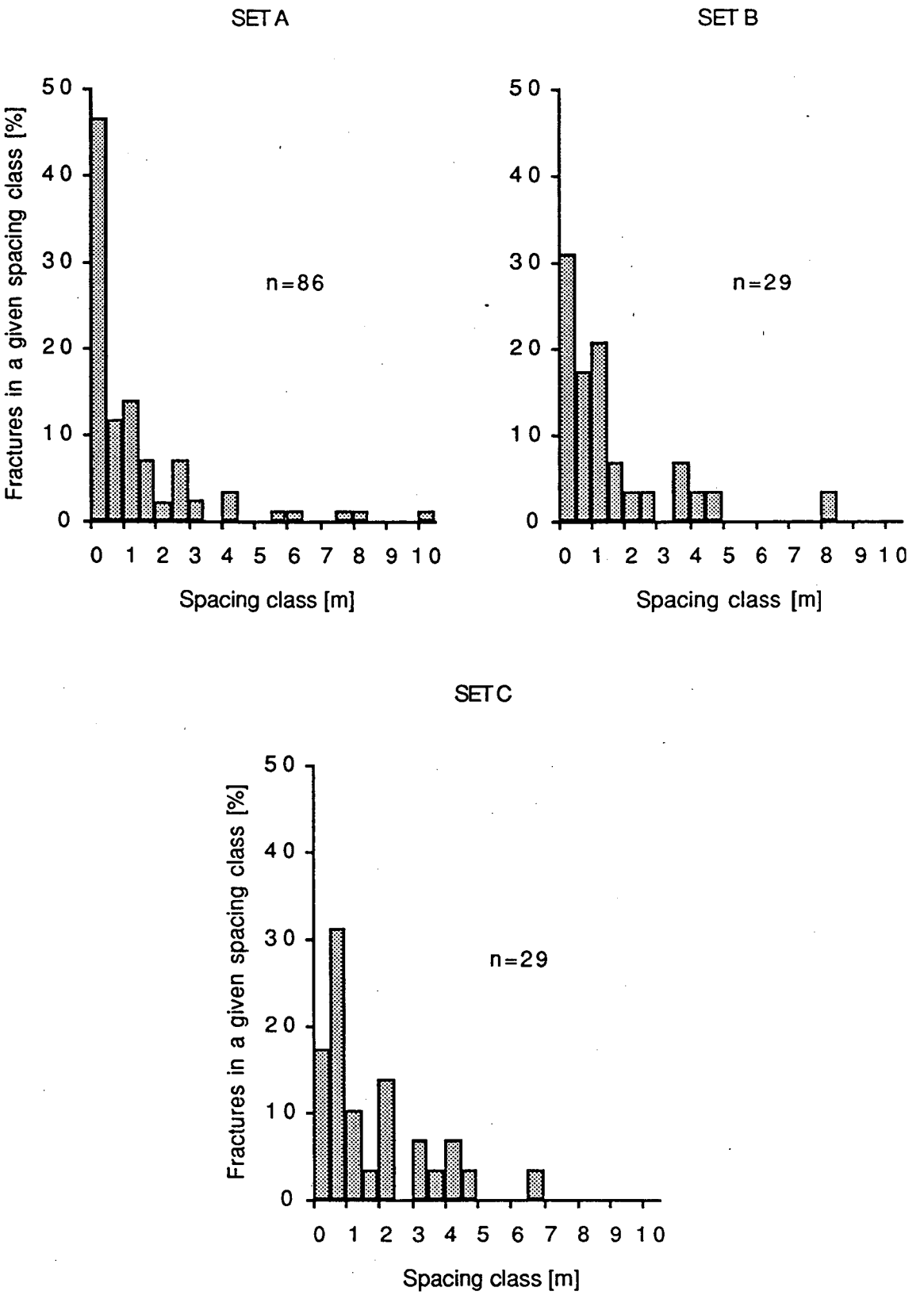

Figure 3.7. Fracture spacing histograms for set A, B, and C.

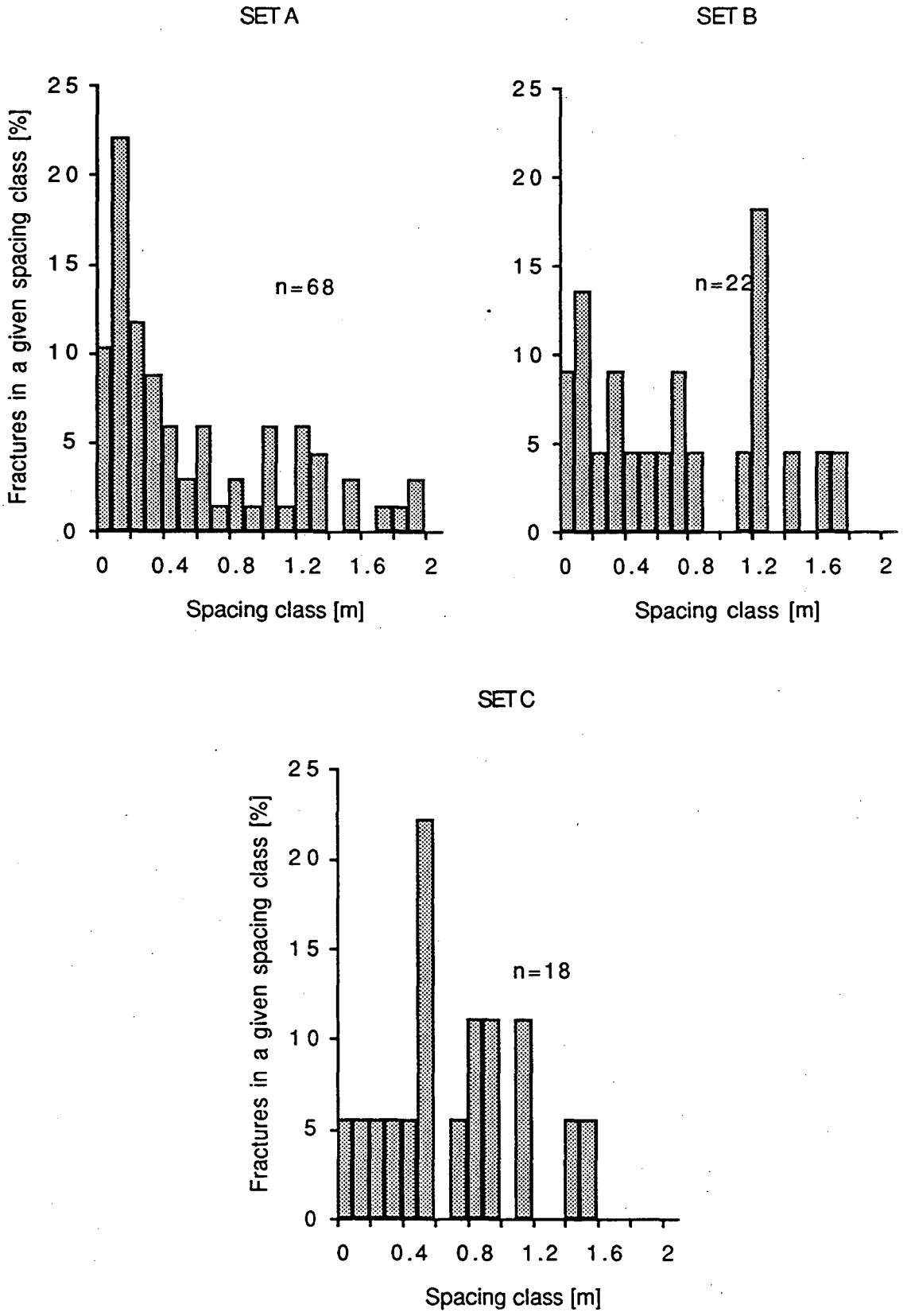

Figure 3.8. Fracture spacing histograms for set A, B, and C. Spacing class < 2m.

combination would result, for example, when several different fracture sets are present or when fractures resulting from different tectonic events overlap one another (Chernyshev and Dearman, 1991). The lognormal distributions shown in Figures 3.7 and 3.8 are not surprising, however. The lognormal model results because very small fractures are not visible, and this results in an underestimate of the number of smaller spacings between adjacent fractures (Chernyshev and Dearman, 1991). The mean of the lognormal spacing distribution for set A, B, and C is -0.49, -0.20, and 0.11, respectively.

Several investigators have attempted to correlate the spacing distribution of subsurface fractures with hydraulic conductivity in granitic rock with little or no success (e.g. Jones *et al.*, 1985; Carlsson and Olsson, 1981). This results from the fact and consistent finding that although many fractures may intersect the well, only a few act to conduct fluid (Paillet, 1991). As shown subsequently, this proved to be the case at the Raymond site. Therefore, no further analysis concerning spacing distribution was carried out.

3.3 Geophysical Logs and Inferred General Hydrogeologic Structure of the Aquifer

In addition to the ATV logs, three-arm caliper, fluid conductivity, 16- and 64-inch normal resistivity, natural gamma, heat-pulse flowmeter, temperature, single-point resistance, spontaneous potential, and lateral logs were collected in each well by the U. S. Geological Survey. Visual inspection of all the normal resistivity, caliper, and heat-pulse flowmeter logs seemed to indicate that there are in general two subhorizontal, hydraulically conductive, fracture zones beneath the site. In light of this observation, and since quantitative data concerning the orientation of individual fractures in well SE-1, SW-1, and 0-0 was now available, this apparent hydrogeologic structure could be more

objectively assessed by checking whether or not the fracture sets exhibit some central tendencies with respect to their geophysical properties. This in turn might suggest which of the fractures or fracture zones are significant conductors of water.

Resistivity logs may indicate where hydraulically conductive fractures are located, for example, because weathered rock materials such as clays in and adjacent to these fractures have high electrical conductivities compared to the parent rock. Caliper logs can show where zones of intense fracturing occur, such as in areas where many closely spaced, subhorizontal fractures are present (Paillet, 1991). The heat-pulse flowmeter (Hess, 1986) is capable of detecting the direction and magnitude of very low flows in a borehole. It is especially useful when measurements are made at different depths in the neighboring wells of a pumped well. In this way, particular fractures or fracture zones contributing flow to the pumped well can be identified. A more comprehensive review of the principles and uses of these and other downhole geophysical techniques used in groundwater investigations is given by Keys (1989).

The three-arm caliper and 16-inch normal resistivity logs of the three wells are shown in Figure 3.9. The borehole diameter indicated by the caliper log is based on an average extension of the three arms. Comparison of the caliper logs with downhole television camera logs revealed that zones where the borehole diameter is greater than 18.5 cm are intensely weathered and broken into angular blocks. These are the zones in which the individual constituent fractures could not be measured on the ATV logs, and which have very large apparent apertures. Given that these fracture zones are present at nearly the same depths in each borehole, and since the regions of closely spaced subhorizontal fractures are commonly enlarged during the drilling process (section 3.2.3), it appears that there are two continuous and subhorizontal fracture zones intersecting the

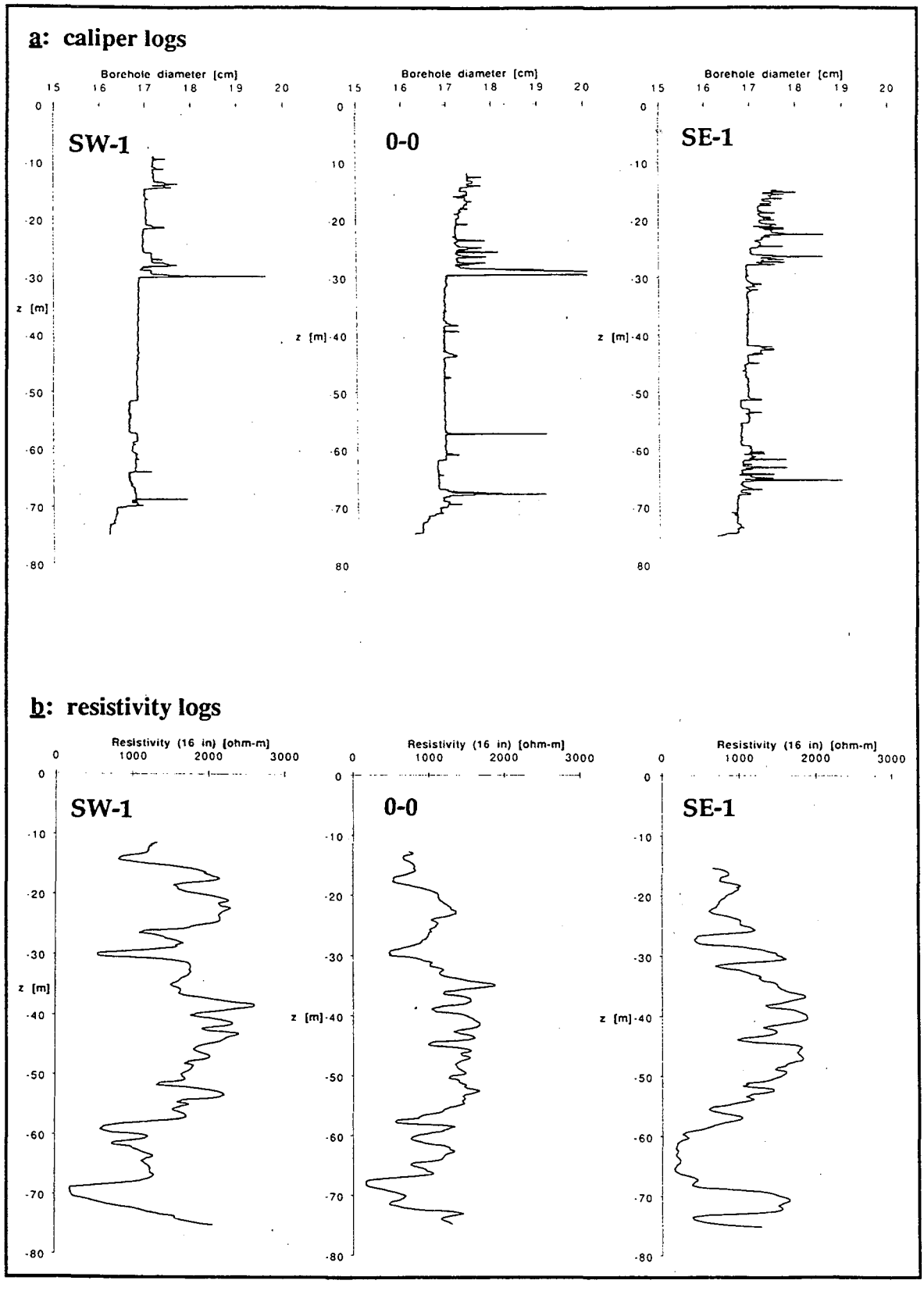

Figure 3.9. a. Caliper logs of wells SW-1, 0-0, and SE-1; b. 16-in. normal resistivity logs for wells SW-1, 0-0, and SE-1.

boreholes: an upper zone at about -30 meters, and a lower zone between -55 and -70 meters. The smaller anomalies occur in chipped-out portions of near vertical fractures, zones of closely-spaced subhorizontal fractures, and in the zone near the uppermost portion of the uncased borehole in which few or no fractures could be identified. This zone appeared to be a transitional region between the shallow regolith and the granitic bedrock.

The 16-inch normal resistivity logs in Figure 3.9b show the measured apparent resistivities in the boreholes. The relatively low resistivities measured near -30 and -70 m are in part the result of the large borehole diameters at these depths. If the true resistivity of the formation is sought, the measurements need to be corrected for several factors including variations in borehole diameter and fluid conductivity, electrode spacing, fluid invasion effects, temperature, and resistivity of adjacent resistive zones (Keys, 1989). The purpose here was to determine if zones of low resistivity (hydraulically weathered zones) are associated with a particular fracture set. Given that 1) the fractures within the anomalously large diameter zones could not be measured and are not part of the database of measured fractures; 2) the aberrations in the borehole diameter near all other mapped fractures is small enough that their effects are negligible (Paillet, oral comm., 1993); and 3) it was found that the fluid conductivity and temperature were constant with depth and essentially the same in each well, the correlation between the mapped fractures that are included in the database with the measured apparent resistivity logs is an appropriate way to evaluate which fractures or fracture sets exhibit a higher degree of weathering (Paillet, oral comm., 1993). Note that the wellbore diameters were the same in all wells during the resistivity survey. It is known that the accuracy of normal resistivity measurements greater than several thousand ohm-meters is questionable and that they should generally only be used in a qualitative way (Keys, 1989). Measurements less than about 1500 ohm-m can generally be used quantitatively (Paillet, oral comm., 1993).

Since the volume of investigation of the resisitivity probe is considered to be a sphere with a diameter approximately twice the spacing of the electrodes (Keys, 1989), and since it is most appropriate to correlate measured fractures to properties close to the borehole, the 16-inch normal resistivity log was used rather than the 64-inch log. In the three wells analyzed, it was found that the depths where the apparent resistivity is less than 700 ohm-m mostly correspond to areas where the subhorizontal fractures are present. Figure 3.10 shows the density plot stereonet of the fractures in all three wells that were at depths where the apparent resistivity was less than 700 ohm-meters.

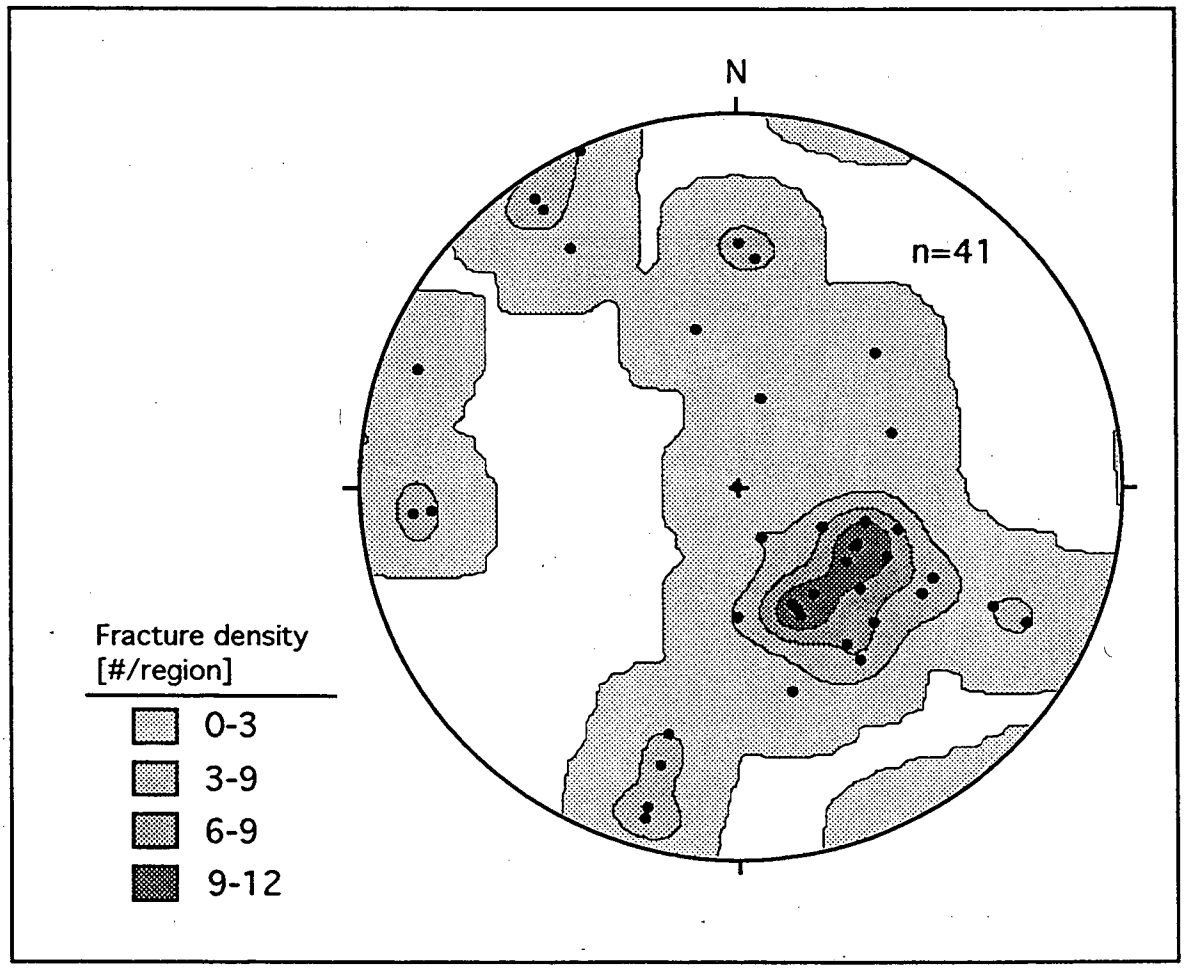

Figure 3.10. Density plot stereonet of fractures occurring at depths where apparent resistvitiy < 700 ohm-m in wells SW-1, SE-1, and 0-0 (Schmidt, equal-area, lower hemisphere, polar projection). North is 1982 true north.

The greater number of total observed fractures belonging to set A in all wells introduces some bias into this analysis. However, the fact that nearly 75 percent of the fractures shown on the stereonet in Figure 3.10 belong to set A, and that only 42 percent of all fractures belong to set A (Table 3.1) indicates that set A does in fact exhibit a higher degree of weathering than the others. Also note that some of the subvertical fractures correlate to low resistivity zones simply because they are located at the same depth as a subhorizontal fracture.

When the apparent resistivities in all the wells are considered (Figure 3.11), two westward dipping weathered zones are apparent. Given that these zones dip in the same direction as the mapped subhorizontal fractures, and since the blowout zones that account for some of the observed low resistances in Figure 3.11 are commonly associated with closely spaced, subhorizontal fractures, it is logical to suggest that these zones are the major conductors of groundwater in this system. The results of the heat-pulse flowmeter survey carried out by the U. S. Geological Survey provide further evidence that this is the case. By measuring the direction and flow rate at different depths in a well during a pump test, and during the recovery from a pump test, several distinct fracture zones that are hydraulically connected to other wells were detected. Figure 3.12 shows the locations of the detected flow zones superimposed over the regions where the apparent resitivity is less than 700 ohm-m. The flow zones shown were found from heat-pulse flowmeter surveys conducted during four (4) different tests: 1) during pumping of well 0-0, 2) during pumping of well SE-3, 3) during the recovery of well SE-3; and 4) during injection into well SE-1. Not all of the flow zones shown were detected during each test.

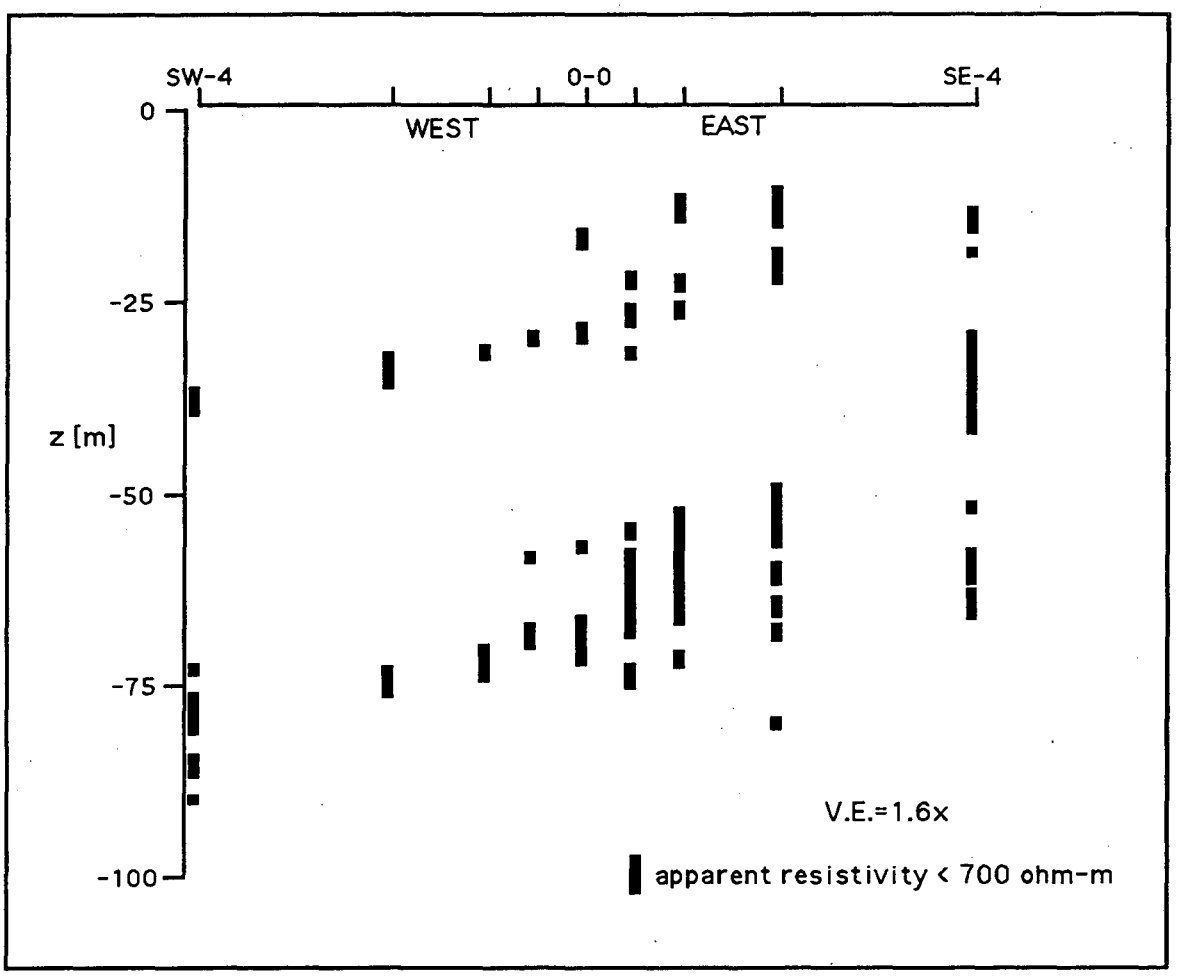

Figure 3.11. Profile of apparent resistivity <700 ohm-m in all wells.

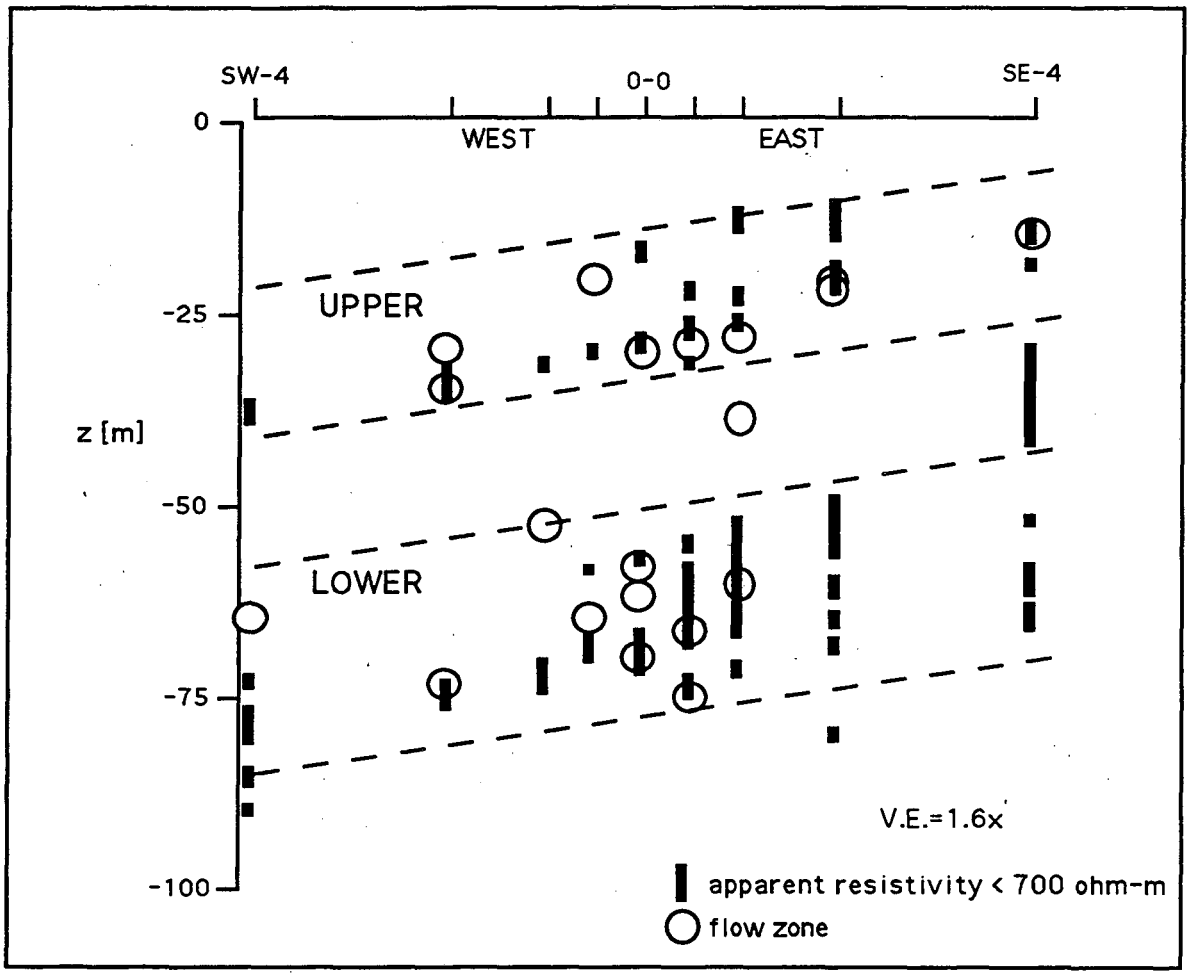

Figure 3.12. Profile of apparent resistivity <700 ohm-m and flow zones in all wells, and inferred general hydrogeologic structure of aquifer.

The detailed study of the fracture sets present, the correlation of the subhorizontal set to the more highly weathered zones adjacent to the boreholes, and visual inspection of Figure 3.12 all support the inferred general hydrogeologic structure of the aquifer: two subhorizontal and nearly parallel zones of unloading fractures, dipping approximately 15° to the west and seperated by about 25 meters.

4.0 PUMPING TESTS

Multiple-well interference tests were conducted in October of 1992. Each test consisted of pumping water out of one well at a constant rate while simultaneously measuring the drawdown in the pumped well and in one or more neighboring wells. Analyses of the transient water level responses during the period of pumping were used to obtain estimates of the transmissivity and storativity of the aquifer, and to estimate the locations of relatively high and low transmissivity zones. No packers were used to seal off particular depth intervals within the wells during the tests described here. The specifications of each test are presented in Table 4.1.

Table 4.1 Specifications of pumping tests.

Test name	Date	Pumped well	Pumping rate [gpm]	Pumping time [hrs]	Drawdown measured in wells:	Total drawdown in pumped well [m]
RAYP22	10/1/92	SE-1	4.0	2	0-0, SE-1	7.2
RAYP3	10/2/92	SW-1	4.0	3.2	0-0, SE-1,SW-1	12.5
RAY12	10/20/92	SW-3	3.0	10	0-0, SW-1,2,3,4	22

*water levels recovered completely from test RAYP22 before test RAYP3 was initiated.

4.1 Instrumentation and Field Procedures

A computerized data logging system and high precision Paroscientific® pressure transducers were used to collect the drawdown data. These transducers can detect water level changes on the order of 0.1mm, and measurements were recorded as often as every 10 seconds. Pressure transducers were installed approximately 30 meters below ground

surface, and a downhole-submersible pump was installed about 0.3 meters above the transducer in the pumped well. Pumping for a particular test was not initiated until the water levels stabilized following previous tests and installation of monitoring instrumentation. A calibrated flowmeter attached to the discharge hose of the pump was used to monitor the discharge rate, and the pumped water was diverted to a nearby ephemeral streambed. Flow from the well usually fluctuated slightly during the first few minutes of a test, while the pump was being adjusted to obtain the desired flow rate, but the pump rate remained steady thereafter.

The downhole pressure transducers measure the cumulative pressure produced by the column of water above them and by the atmospheric pressure. A transducer at land surface was therefore connected to the logging system. Drawdown was taken as the difference between downhole and atmospheric pressures at the time just prior to the initiation of pumping minus the difference between these measurements at any later time. The barometric efficiency of the aquifer was therefore assumed to be 100%. This assumption does not introduce significant errors into the analyses because the drawdowns in wells were several orders of magnitude greater than the maximum amount of possible water level fluctuation due to atmospheric pressure changes alone. In addition, the barometric efficiency is likely to be large since the aquifer is located in shallow granitic rock.

4.2 Results and Interpretation

4.2.1 General

Figures 4.1, 4.2, and 4.3 show the drawdowns in the pumped well and in the observation wells during the three tests. Even prior to formal analysis, several qualitative inferences can be made from visual inspection of these graphs.

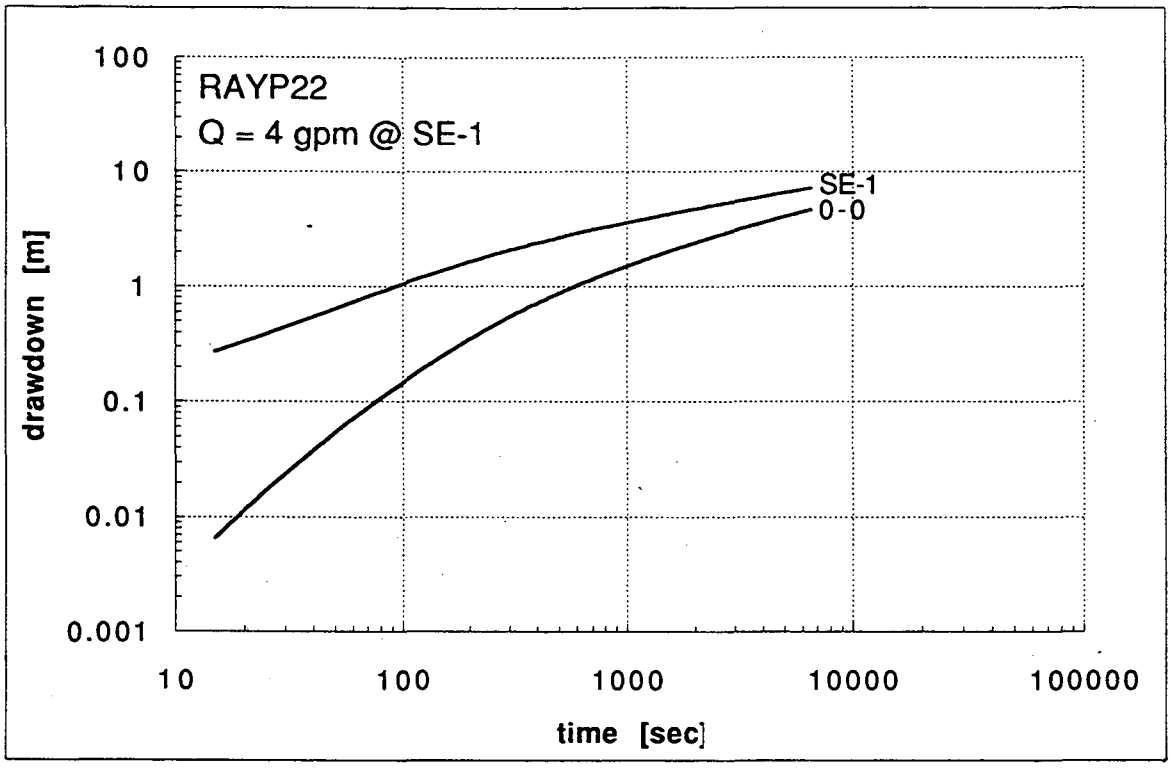

Figure 4.1. Log-log plot of drawdown vs. time in wells during test RAYP22.

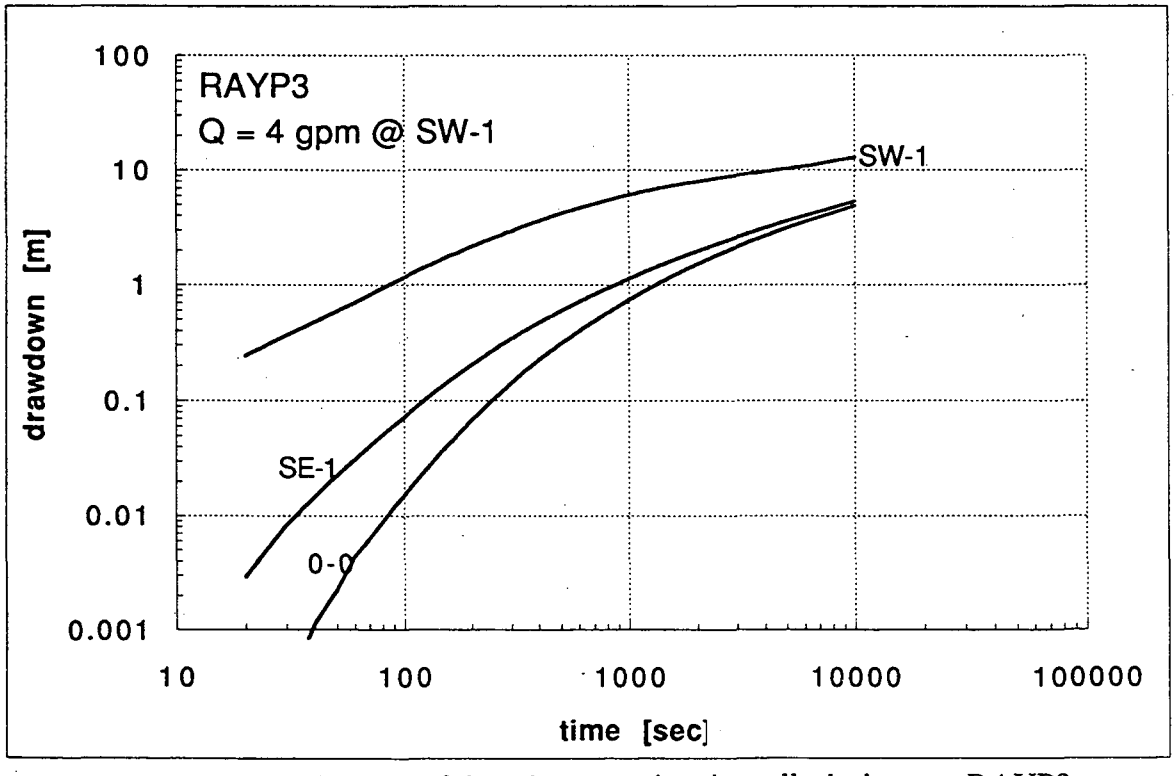

Figure 4.2. Log-log plot of drawdown vs. time in wells during test RAYP3.

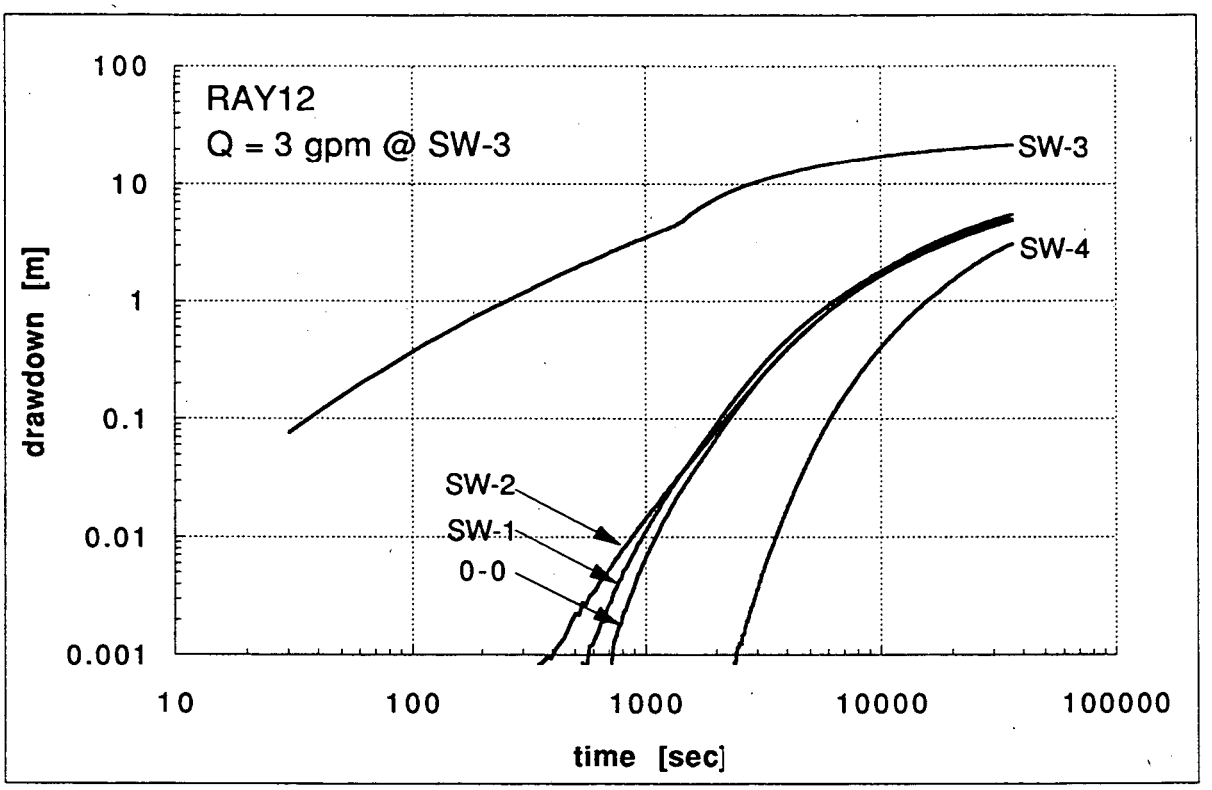

Figure 4.3. Log-log plot of drawdown vs. time in wells during test RAY12.

For example, the fact that the drawdowns in wells 0-0, SW-1, and SW-2 during test RAY12 (Fig. 4.3) are nearly identical in magnitude, even though they are as much as 15 meters apart from one another, suggests that they are connected by a zone of very high transmissivity. In addition, well 0-0 responds quicker and with greater magnitude during test RAY12 than does well SW-4, even though both are the same distance from the pumped well. Similarly, the drawdown in well SE-1 is more than twice that in well 0-0 for more than half the duration of pumping during test RAYP3 (Fig. 4.2).

The abrupt increase in drawdown in the pumped well (SW-3) during test RAY12 (Fig. 4.3) is believed to be the result of the water level falling below the bottom of the casing and into the smaller diameter, uncased wellbore. Such fluctuation is possible if wellbore storage effects are still significant, a condition indicated by the near unit-slope of the drawdown curve up to about 1050 seconds.

The aquifer transmissivity and storativity were estimated using the traditional Theis curve matching procedure for the observation wells. Transmissivity was determined from the pump well drawdowns using the Cooper-Jacob semilog analysis. The equations used for the analyses are shown for completeness in the following sections. It is recognized that these methods are generally best suited for the analysis of tests conducted in confined and porous media aquifers. The assumptions that flow is horizontal towards the well and that the wellbore penetrates the entire thickness of a confined aquifer inherent in these analyses is considered satisfied for all practical purposes. As shown in section 3.3, most of the flow is confined to the two subhorizontal fracture zones located within the interval of the uncased wellbore, and the water levels in wells during undisturbed conditions are tens of meters above the level of the upper subhorizontal fracture zone. Additionally, the drawdown responses in wells do not exhibit characteristics which would warrant the use of analysis procedures designed for an aquifer system different from that assumed for the Theis solution, such as a discretely fractured, leaky, dual-porosity, or unconfined aquifer. It is also recognized that the values determined from these analyses are first-order, spatially averaged approximations. The practical appeal in using the Theis curve matching procedure and semilog analysis is in their relative simplicity and usefulness in helping to identify what types of conditions (e.g., flow geometries and/or boundary conditions) might exist that could account for the deviation of the actual drawdowns from the ideal case. The analyses also provide quantitative input to more detailed numerical calculations.

4.2.2. Analysis of Drawdowns in Pumped Wells

After a relatively short time of pumping, the drawdown in the pumped well may be described with the Cooper-Jacob equation (1946). This formulation assumes that wellbore storage effects have dissipated and that there is no skin effect or turbulent flow around the well. The drawdown, $s_{(r_w,t)}$, is then expressed as:

$$s_{(r_w,t)} = \frac{2.303Q}{4\pi T}\log_{10}\frac{2.25Tt}{r_w{}^2 S} \tag{4.1}$$

where s is the drawdown, Q is the total pumped discharge, T and S are the aquifer transmissivity and storativity, respectively, t is the time since pumping began, and r_w is the well radius. When $4Tt / Sr_w{}^2 \geq 100$, the error in using (4.1) rather than the complete Theis formula is less than 0.3% (de Marsily, 1986). By simple manipulation of (4.1), it is easy to see that

$$s_{(r_w,t_2)} - s_{(r_w,t_1)} = \frac{2.303Q}{4\pi T}\log_{10}\frac{t_2}{t_1} \tag{4.2}$$

if $t_2 = 10t_1$ then (4.2) can be rewritten:

$$T = \frac{2.303Q}{4\pi(\Delta s / \log \text{ cycle})} \tag{4.3}$$

The transmissivity can therefore be found from (4.3) by plotting the drawdown vs. the logarithm of time and noting the slope of the first straight line portion of the curve. Figures 4.4 and 4.5 show the semilog plots corresponding to pumping of wells SE-1 and SW-1. The calculated transmissivity is shown inside each figure.

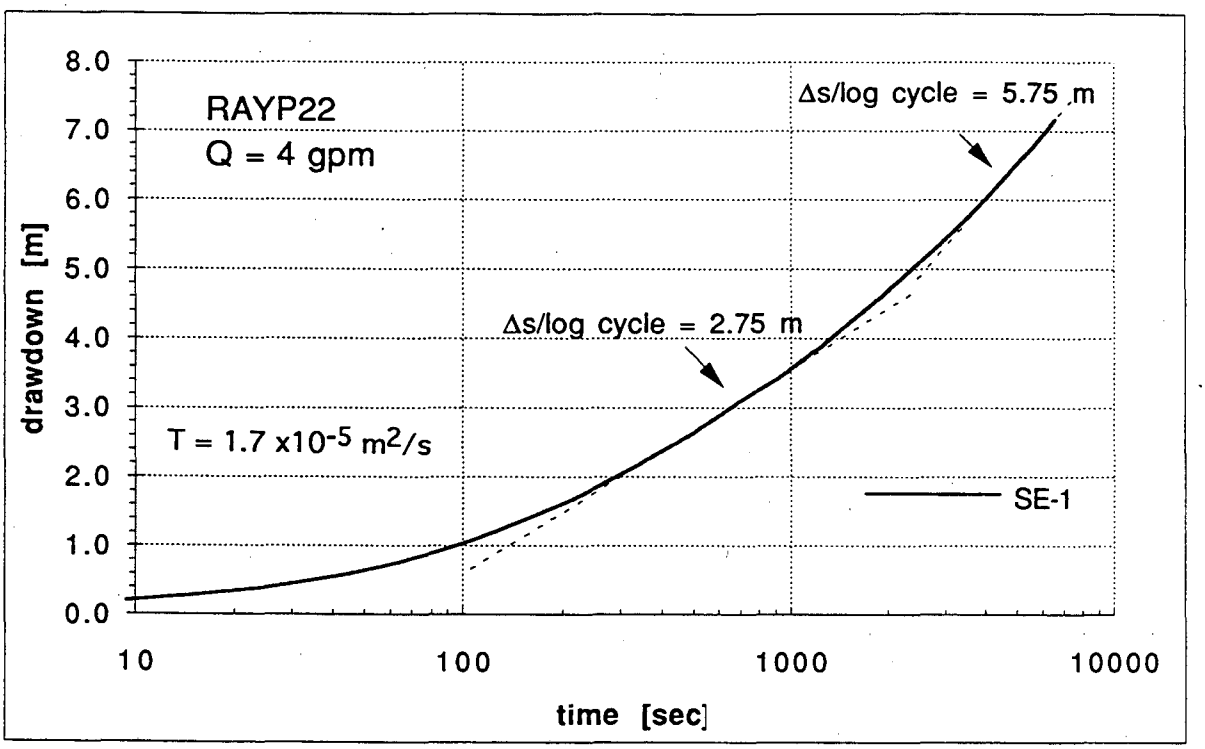

Figure 4.4. Semilog plot of drawdown vs. time in pump well SE-1.

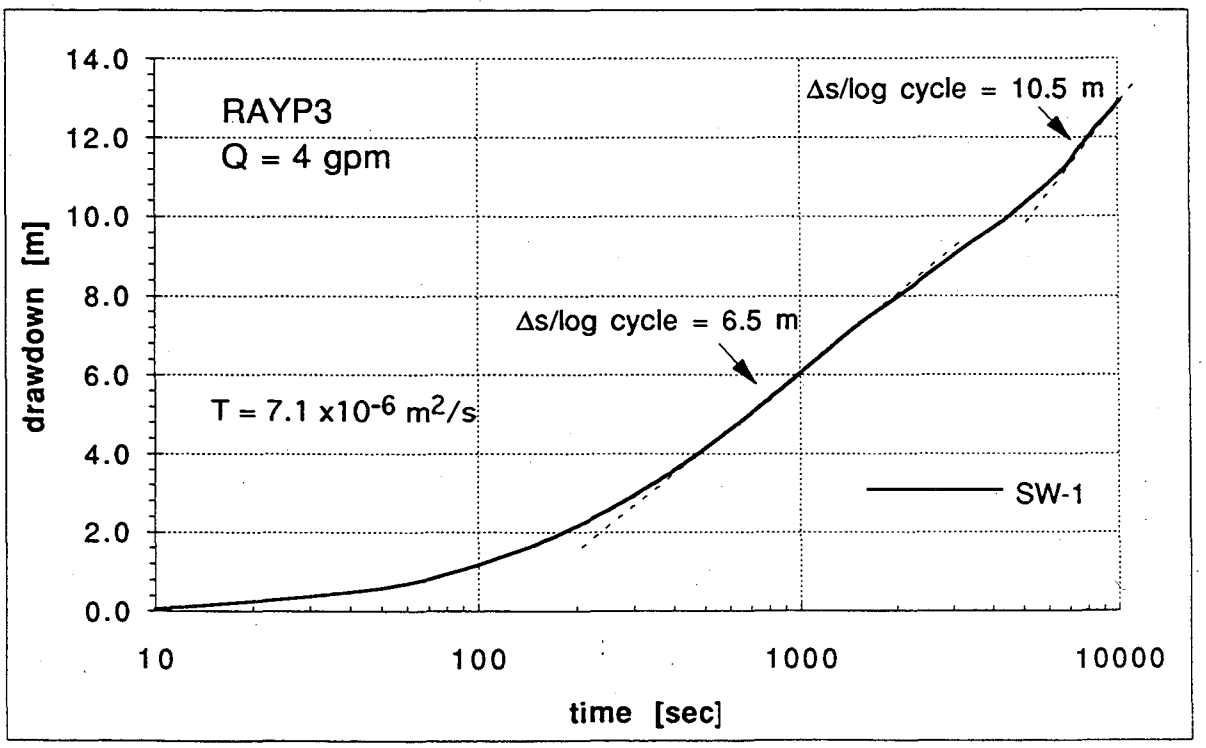

Figure 4.5. Semilog plot of drawdown vs. time in pump well SW-1.

For the purpose of investigating the aquifer properties in the region of wells SE-1, SW-1, and 0-0, the results of a pump/flowmeter test conducted in well 0-0 are also considered in the following analysis. This test (described in section 5.0 and named FLOW 0-0) involved the use of an inflatable packer in the wellbore which was alternatingly inflated and deflated after about 2000 seconds of pumping. The use of the packer produced small oscillations in the pumped well drawdown, but calculations showed that it did not influence the overall drawdown response in any significant way (section 5.3). Figure 4.6 shows the semilog plot of the drawdown in well 0-0 and the corresponding calculated transmissivity by (4.3).

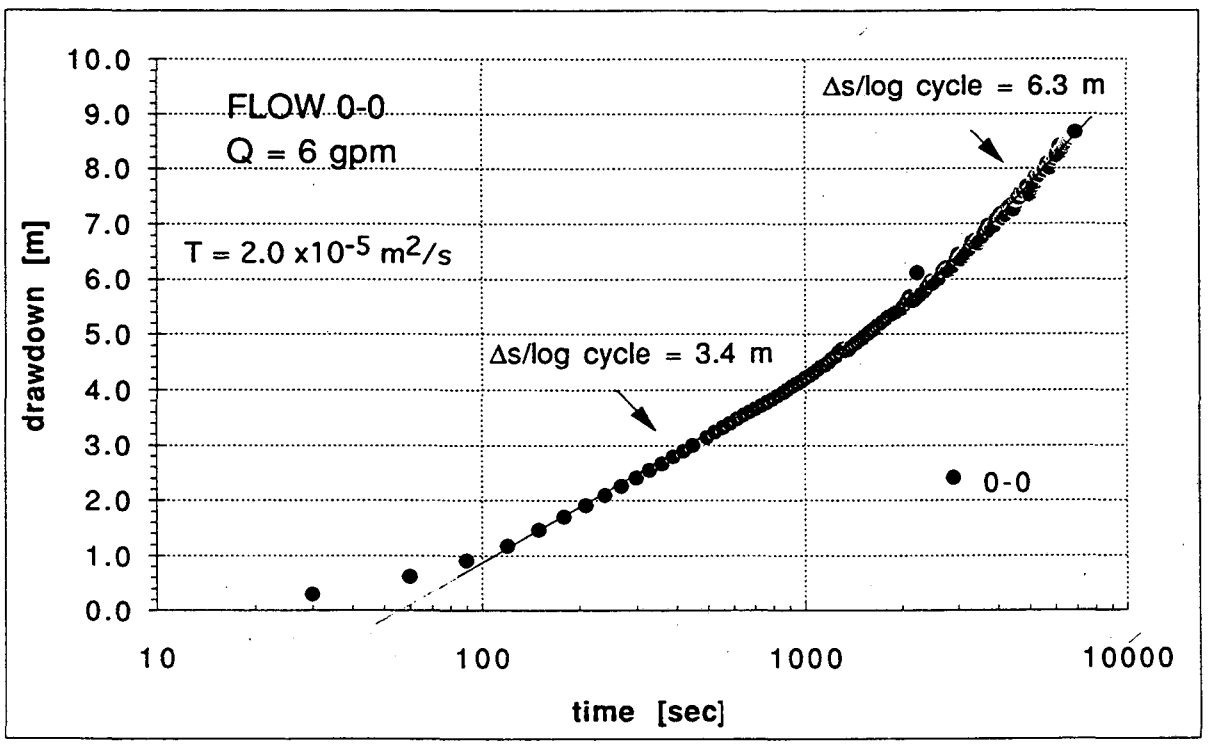

Figure 4.6. Semilog plot of drawdown vs. time in pump well 0-0.

An interesting finding in the above analysis is that the calculated transmissivity found from the pumping test in wells 0-0 and SE-1 is more than twice that found from the test in well SW-1, despite the fact that the wells are only 7.5 meters away from each other. This may be indicative of the high degree of heterogeneity present over relatively small scales. Two possible causes are the discontinuity of fractures or fracture zones, and the spatial variation of fracture apertures. Large variations in transmissivity can result from relatively small changes in fracture apertures because of the cubic dependence of fracture transmissivity on aperture.

The relatively low transmissivity calculated from the pumping test in well SW-1 could be explained by the presence of a low conductivity zone situated to the west of SW-1. This inference is based on the time at which the drawdowns in wells 0-0 and SE-1 begin to deviate from the first straight line portions on their respective semilog plots, the distance these wells are located from well SW-1, and on the aquifer properties determined from each test. As a first approximation, this zone is considered to create a linear impermeable boundary. The distance to such a boundary can be determined from the semilog plot of drawdown in the pumped well using the equation

$$r_b = \frac{1}{2}\sqrt{\frac{2.25Tt_I}{S}} \tag{4.4}$$

where r_b is the radial distance to the boundary from the pumped well, and t_I is the time at which the presence of the boundary begins to influence the drawdown in the pumped well. This time is approximately indicated by the point of intersection of the two straight line portions on the semilog drawdown curve (de Marsily, 1988). A practical problem in using equation (4.4) results from the fact that the storativity cannot, in general, be determined from the drawdown response in the pump well. The approach taken here was to first use the storativity determined from a Theis curve analysis of the drawdown in

observation well SW-4 during test RAY12 (Fig. 4.13). The drawdown in this well is distinct from all the others in that the entire drawdown curve matched the Theis curve. Therefore, the confidence associated with the calculated storativity of 2.4 $\times 10^{-4}$ found by this analysis is highest. Using a slightly different storativity of 2.3 $\times 10^{-4}$, a consistent formulation in the remaining analyses was possible. The calculated radial distance to the boundary from wells SE-1 and 0-0 using a t_I of 2500 and 2000 sec, the transmissivity determined from each test, and a storativity value of 2.3 $\times 10^{-4}$, is about 10 meters. Since the distance to well SW-1 from well SE-1 and 0-0 is just short of this value, and since the presence of a low transmissivity boundary located on the westward side of well SW-1 would affect the early-time drawdown for pump well SW-1 and result in a calculated transmissivity approximately half that of the adjacent and more conductive area, it is plausible that a zone of decreased transmissivity lies directly to the west of well SW-1. This possibility is explored more thoroughly in the next section, and by means of a numerical simulation described in section 6.0. The increase in slope of the drawdown curve for well SW-1 at 7000 seconds could have been produced by a second discontinuity.

Geometries other than an impermeable boundary can cause drawdowns similar to the ones described above. When a pump well is located in a region of high hydraulic diffusivity (defined as T / S), which in turn is surrounded by an annular region of lower diffusivity, the semilog drawdown plot will in theory exhibit an early straight line portion followed by some transitional period. After this period a second straight line portion with a slope less than twice that of the first would appear. An aquifer with this type of heterogeneity is referred to as a 'composite aquifer' (Louches and Guerro, 1961; Ramey, 1970). Evidence for the presence of a zone of high transmissivity immediately around the pump wells is presented in the next section. A pumped well response similar to the one just described can also occur if there is a linear discontinuity behind which the

transmissivity is lower, but not so low as to be considered impermeable (Bixel *et al.*, 1963).

4.2.3 Evaluation of Wellbore Skin and Skin Effect

The act of drilling and producing a well invariably alters the formation characteristics around it. The invasion of drilling fluids into the aquifer material adjacent to the well, or the accumulation of transported clayey particles in this zone resulting from pumping, for example, can produce a zone around the well which has a relatively low permeability compared to that in the rest of the formation. One of the effects of this disturbed zone will be to enhance the drawdown in the pumping well. Conversely, the drawdown will be lessened by the presence of a zone of relatively high permeability, a condition which could be produced by the installation of a gravel pack or because of the presence of fractures adjacent to the well, for example. In discussing the effects of a zone of increased permeability around a well, Jacob (1947) was the first to introduce the concept of an 'effective well radius', which he defined as the radial distance from the center of the well at which the theoretical drawdown equals the actual drawdown just outside the well screen. Later, van Everdingen (1953) and Hurst (1953) coined the term 'skin' and 'skin effect' to denote the zone of differing permeability around the pump well and its effect on the drawdown. A zone of enhanced permeability is said to have a negative skin, whereas a zone of decreased permeability acts as a positive skin. The impetus for investigating skin effects here stems from the fact that there are zones of intensely fractured rock alongside the wellbore. From the outset then, the potential for negative skin effects seems great. Given that some observation wells are located as little as 7.5 meters from the pumped well, it is perhaps possible that a wellbore skin could also affect drawdowns at these wells. Gringarten and Witherspoon (1972) noted that a large

negative skin or fracture can affect observation well responses, despite the fact that they are generally considered only to influence the drawdown in the pumped well.

Van Everdingen (1953) defined the skin factor as a constant that equates the change in hydraulic head across the skin zone to the flow rate and to the permeability of the formation. For a confined aquifer, this relationship may be expressed as follows:

$$\Delta H_{skin} = s_k \left(\frac{Q}{2\pi T} \right) \tag{4.5}$$

where ΔH_{skin} is the change in hydraulic head across the skin zone and s_k is the dimensionless skin factor. With the inclusion of the skin effect, semi-steady state flow into the wellbore is now expressed by a modified Cooper-Jacob equation:

$$s_{(r_w,t)} = \frac{2.303Q}{4\pi T} \log_{10} \frac{2.25Tt}{r_w{}^2 S} + s_k \frac{Q}{2\pi T} \tag{4.6}$$

which can be rearranged to yield the skin factor:

$$s_k = 1.15 \left(\frac{s_{(r_w,t)} 4\pi T}{2.303Q} + \log_{10} \frac{r_w{}^2 S}{2.25Tt} \right) \tag{4.7}$$

As indicated by equation (4.7), the skin factor may be determined by noting the drawdown corresponding to any time on the first straight-line portion of the semi-log drawdown plot or, more easily perhaps, by extrapolating the straight line portion of the line to the time corresponding to zero drawdown. In this way, the first term inside the brackets of equation (4.7) may be neglected. As with equation (4.4), the practical problem in using equation (4.7) is that the storativity cannot be determined from the drawdown response in the pump well (precisely because of head losses such as the skin

effect which result in an ill-defined wellbore radius). From the semilog plots of drawdowns in the pumped well during test RAYP22 and FLOW 0-0, the skin factors for wells SE-1 and 0-0 using (4.7) were found to be -3.6 and -3.7, respectively. A storativity value of 2.3×10^{-4} and a nominal borehole radius of 8.5 cm was used in these calculations. As expected, the analysis reveals that a zone of enhanced transmissivity surrounds these wells. Given that the boreholes intersect densely fractured zones, the finding that they possess negative skins makes sense physically. In addition, the skin factors obtained here are of the same order as those observed for wells which have been hydraulically fractured. These wells typically exhibit skin factors between -3 and -5 (Matthews and Russell, 1967).

Of interest is the approximate size of the zone of enhanced transmissivity around the wells. Assuming that the zone of differing permeability is an annular region around the wellbore, Hawkins (1956) showed that

$$s_k = \left(\frac{k}{k_s} - 1\right) \log_e \frac{r_s}{r_w} \tag{4.8}$$

where k and k_s are the permeability of the formation and of the skin zone, respectively, and r_s is the radius of that zone measured from the center of the wellbore. The practical appeal of equation (4.8) is that an approximate value r_s can be determined when a negative skin is present. For the case where the permeability of the skin is much greater than the formation, equation (4.8) can be rearranged to obtain an effective wellbore radius, r_e:

$$r_e = r_w e^{-s_k} \tag{4.9}$$

Nothing very specific can be said, however, about the transmissivity of this zone, only that it is probably at least an order of magnitude more than that of the surrounding area. The effective radii of wells SE-1 and 0-0 using the skin values obtained earlier and equation (4.9) are 3.1 and 3.4 m, respectively.

If the calculated distances to the boundary and the effective radii of each well is considered in the theoretical solution, the drawdowns in the pumped wells can be matched almost exactly (Figs. 4.7 and 4.8). The match of the theoretical curve to the drawdown in well 0-0 up to 100 seconds, and the underpredicted drawdown in well SE-1 during this time is coincidental. Wellbore storage and pumping fluctuations persist during this time, so the match or mismatch of the curves during this time should be ignored. The fact that the theoretical curve fits the data after 100 seconds is significant.

The skin factor for well SW-1 can not be determined by equation (4.6) because the early time drawdown is already influenced by the nearby boundary. An additional term that accounts for the increased drawdown produced by the presence of this boundary would theoretically need to be added to equation (4.6). However, by including this term, the skin factor solution becomes non-unique even if T and S are assumed to be known. The result is that the distance to the image well and the effective radius of the well can be substituted for one another to yield the same theoretical drawdown. Because the drawdown response in pumped well SW-1 is influenced by a boundary at very early times, and since the semilog drawdown analyses of pumped wells SE-1 and 0-0 revealed that a low conductivity boundary is located approximately 10 meters from these wells, the boundary is likely to be located to the west of well SW-1. Since well SW-1 is approximately 7.5 meters away from each of these wells, an initial estimate of the distance to the low conductivity boundary from well SW-1 is 3 meters. Figure 4.9 shows that the drawdown in well SW-1 can be matched almost exactly if it assumed to have an

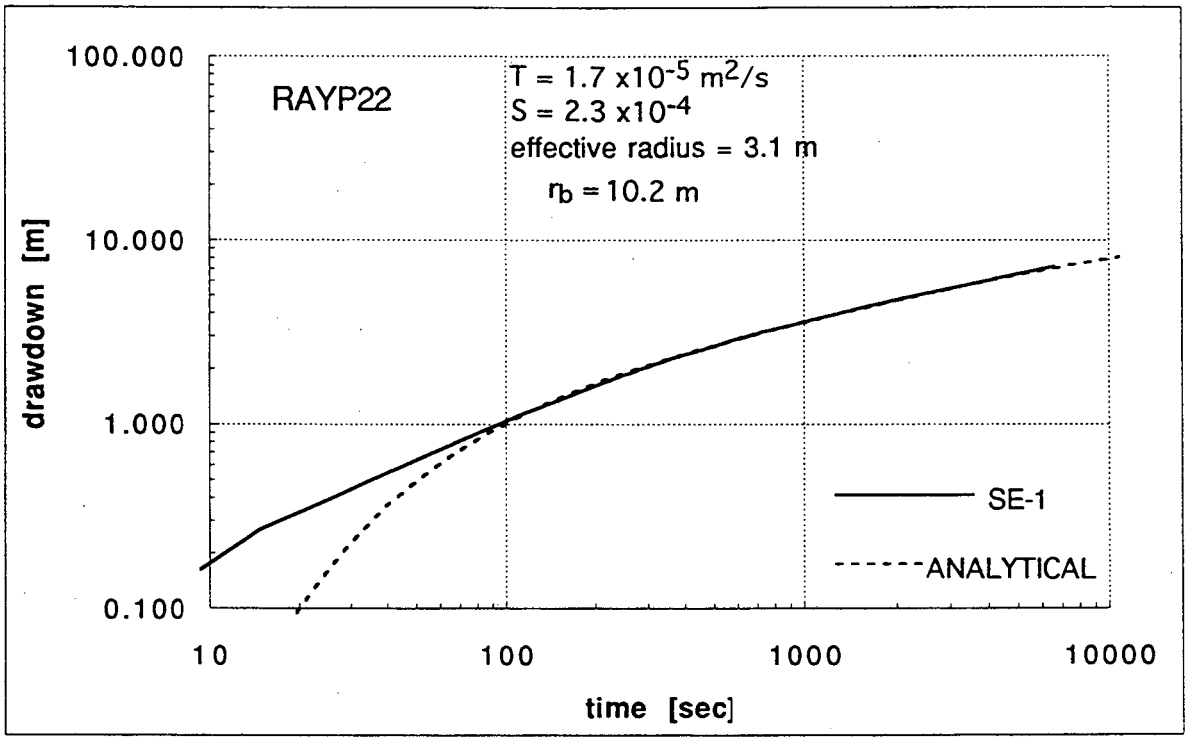

Figure 4.7. Match of analytical solution that considers effective radius and impermeable boundary to drawdown in pump well SE-1.

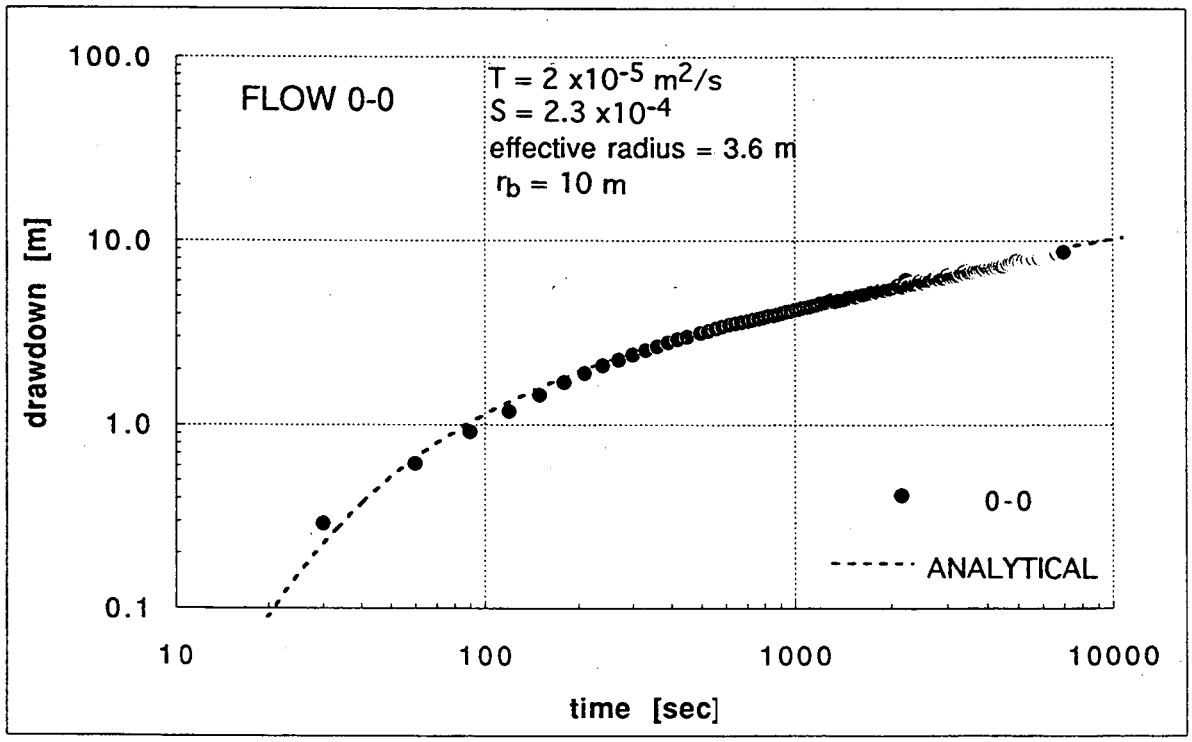

Figure 4.8. Match of analytical solution that considers effective radius and impermeable boundary to drawdown in pump well 0-0.

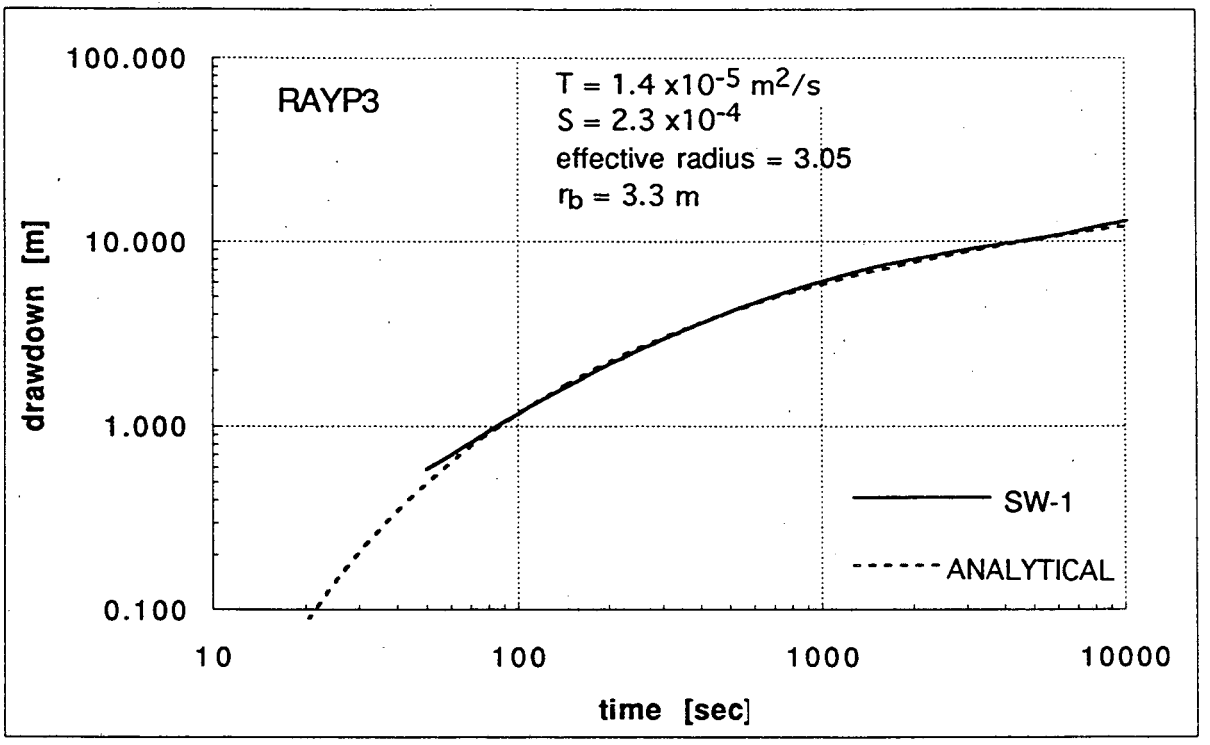

Figure 4.9. Match of analytical solution that considers effective radius and impermeable boundary to drawdown in pump well SW-1.

effective radius of 3.05 meters, and to be located 3.3 meters from the boundary. These distances are consistent with the findings from the other drawdown analyses in that the drawdowns in all three wells can be explained by single linear boundary located approximately 3 meters to the west of well SW-1. In addition, the effective radius of 3.05 m is equivalent to a skin factor of -3.6, a value consistent to those found for the other wells. These findings suggest that the presence of a low conductivity zone to the west of well SW-1 and a region of high transmissivity near the wells could be two of the prominent heterogeneities situated near the well field.

As shown in the next section, the transmissivities from drawdown analyses from observation wells during test RAY12 are about 4.5 times less than the those found from

pumping in wells 0-0 and SE-1. This may be further evidence that the portion of the aquifer located to the west of well SW-1 has a lower transmissivity than the eastern side.

The concept of an effective well radius is useful in that it helps to provide an estimate of the extent of the higher permeable region around the wellbores. Agarwal and others (1970) pointed out that the definition of the skin factor as a constant relating a pressure drop to steady-state flow (as indicated by eq. 4.5) is fundamentally incorrect. A region of differing permeability around the well also has a storage capacity, and therefore transient flow must exist in the skin zone. However, they realized that this transient period is short, and that it can probably be neglected for all practical purposes.

Finally, the effective radii determined above almost overlap one another in the region of wells SW-1, SE-1, and 0-0. It seems more physically reasonable then that there exists a continuous zone of relatively high transmissivity connecting these three wells, rather than each possessing a finite radius skin. For this reason, analysis of the transient well responses might be more amenable to the 'composite reservoir' analysis such as that presented by Louckes and Guerrero (1961).

4.2.4 Analysis of Drawdowns in Observation Wells

In order to evaluate the observation well responses during both early and late times, the complete Theis solution was used to match observation well data. The complete Theis function is given by

$$s_{(r,t)} = \frac{Q}{4\pi T}\left[-E_i\left(-\frac{r^2 S}{4Tt}\right)\right] \tag{4.10}$$

where E_i is the exponential integral and the remaining variables and parameters are as defined before. Theis curve matching to observation well data was accomplished using a computer spreadsheet, and a polynomial approximation with an absolute error less than 5×10^{-5} was used to evaluate the exponential integral.

No single combination of T, S, and distance to impermeable boundaries could be used to fit the Theis solution to the entire drawdown curve for most of the observation wells. The fitted curves to the observation well data for test RAY12 are shown in Figures 4.10 through 4.13. The fact that the fitted storativity values are very much different from one another, but that the transmissivities are roughly the same for the Theis curves matching the drawdowns in these wells, is a consequence of fitting the Theis curve to drawdowns in a medium with varying transmissivity (e.g. in a anisotropic or composite medium). It does not necessarily indicate that the storativity is very different near these wells. Because all of the observation wells for test RAY12 lie along the same transect, the methods of Papadoupulos (1965) or Neuman *et al.* (1984) designed to determine the directions of maximum and minimum transmissivity could not be employed.

Given that there was a considerable time during which wellbore storage was significant in test RAY12, it is unusual that the early time drawdowns in the observation wells are displaced to the left of the Theis curve. In an ideal system with wellbore storage in the pump well, the early time drawdowns in observation wells would in theory be displaced to the right of the Theis curve (Papadopoulos and Cooper, 1967). The deviation at early times is believed to have occurred because of the presence of the high transmissivity zone connecting these wells. In this sense a similar condition as that observed around wells 0-0, SE-1, and SW-1 exists near these wells. The presence of a

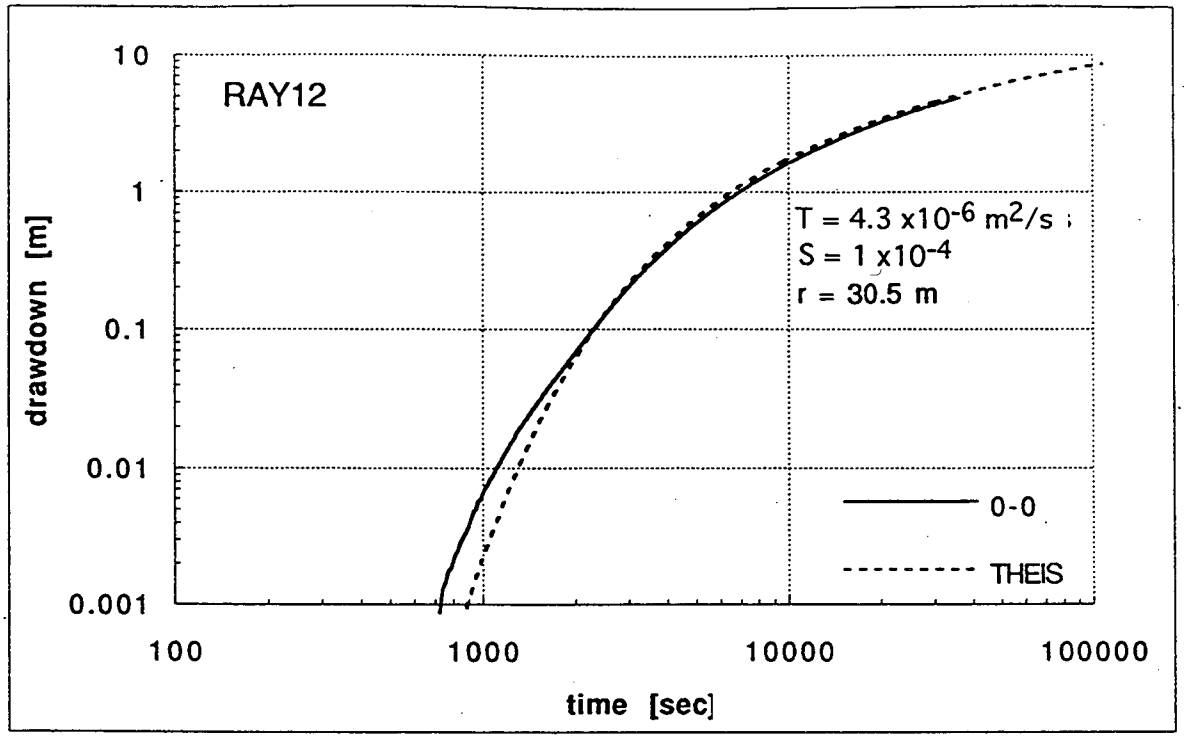

Figure 4.10. Theis curve match to drawdown in well 0-0 during test RAY12.

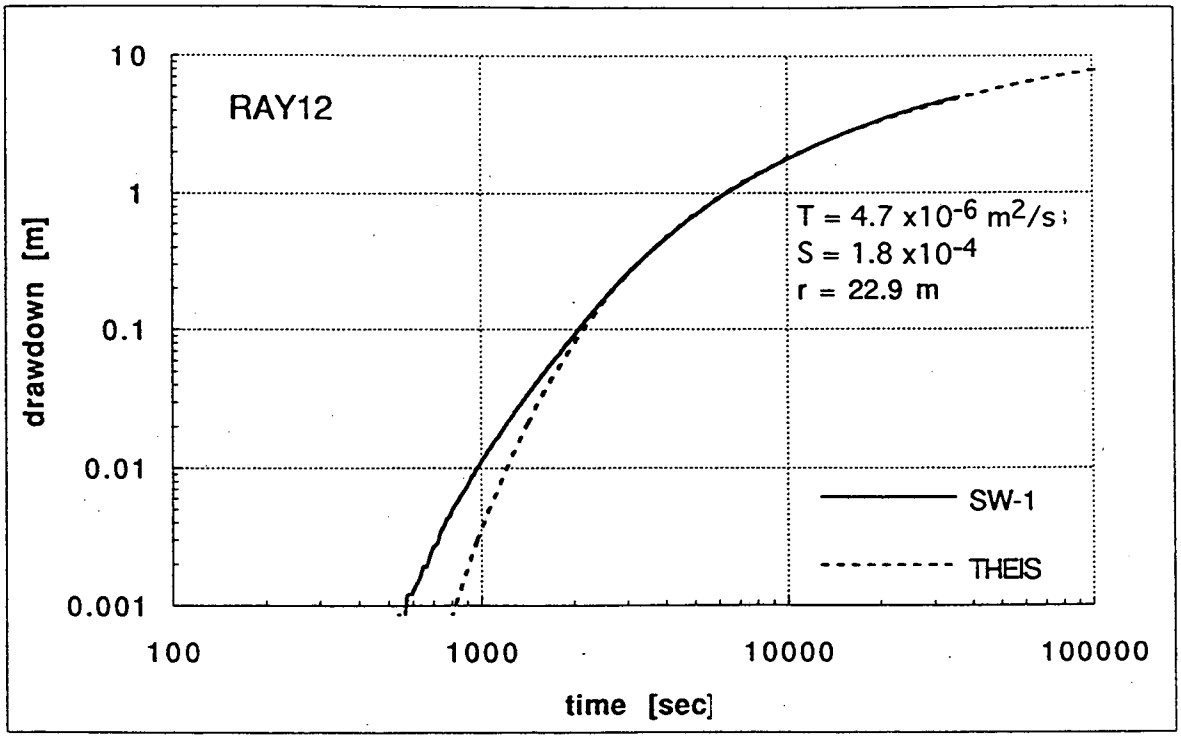

Figure 4.11. Theis curve match to drawdown in well SW-1 during test RAY12.

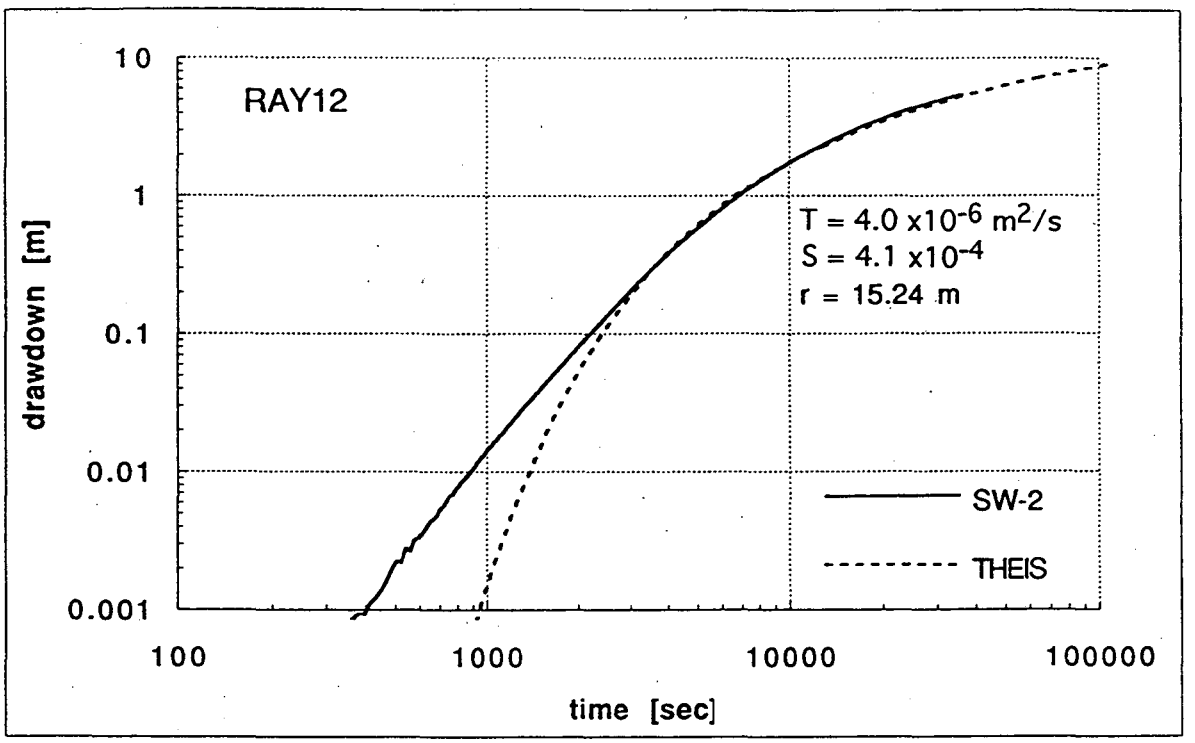

Figure 4.12. Theis curve match to drawdown in well SW-2 during test RAY12.

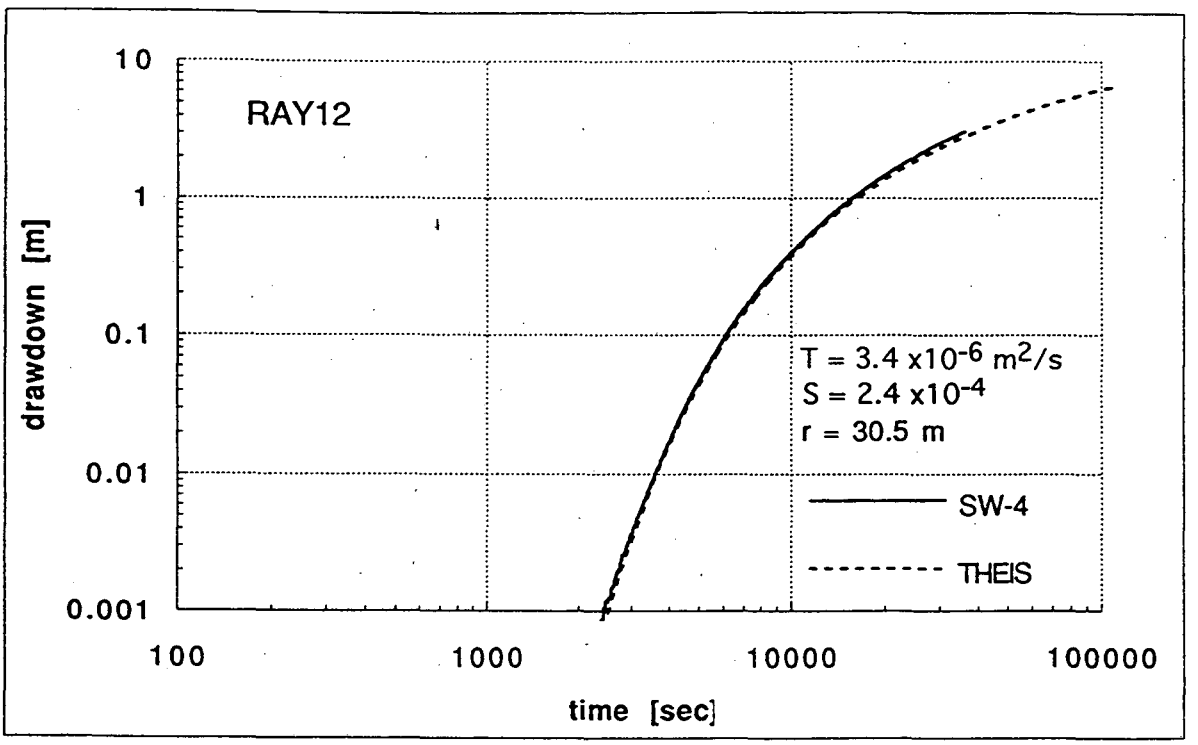

Figure 4.13. Theis curve match to drawdown in well SW-4 during test RAY12.

zone with a relatively high transmissivity would act to yield a quick response in the observation wells. Note that the transmissivities found for the observation wells to test RAY12 are about 4.5 times less than the those found from pumping in wells 0-0 and SE-1. This may be further evidence that the portion of the aquifer located to the west of well SW-1 is generally of a lower transmissivity than that on the eastern side.

The match of the analytical solution, which is the superposition of two Theis solutions, to the drawdown in well 0-0 during test RAYP22 is shown in Figure 4.14. The match to the drawdowns in wells SE-1 and 0-0 during test RAYP3 is shown in Figure 4.15 and 4.16.

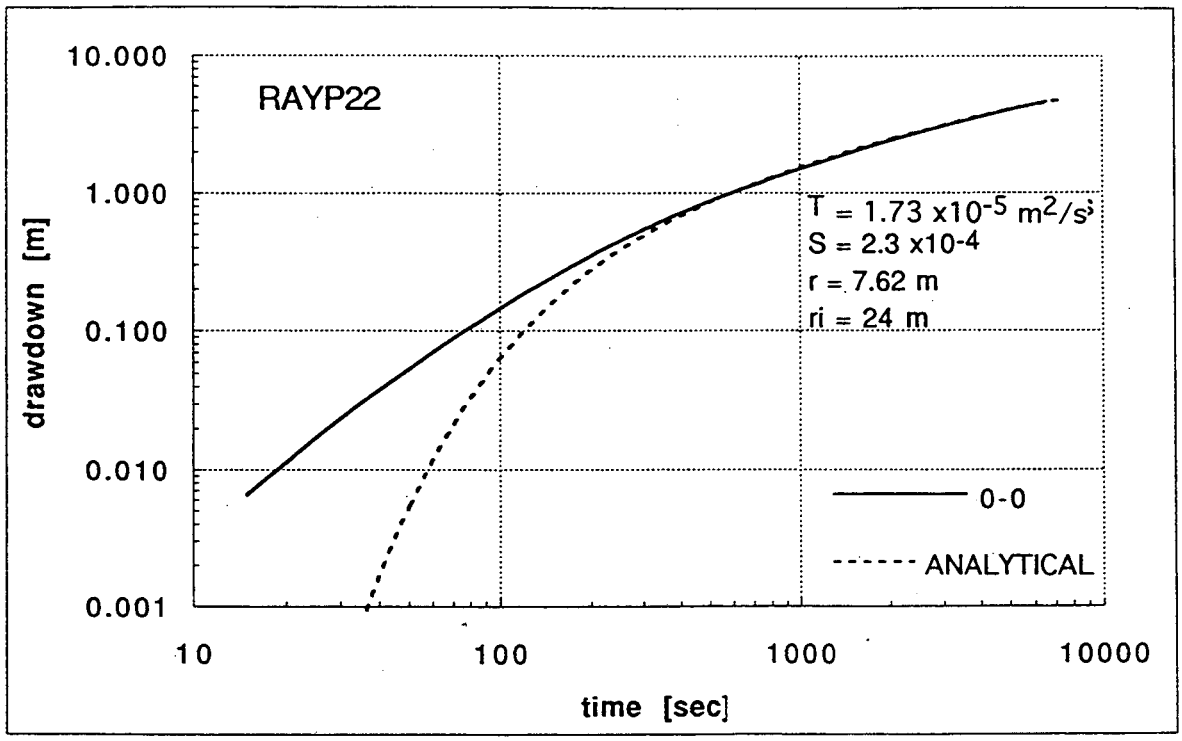

Figure 4.14. Match of analytical solution that considers impermeable boundary to drawdown in well 0-0 during test RAYP22.

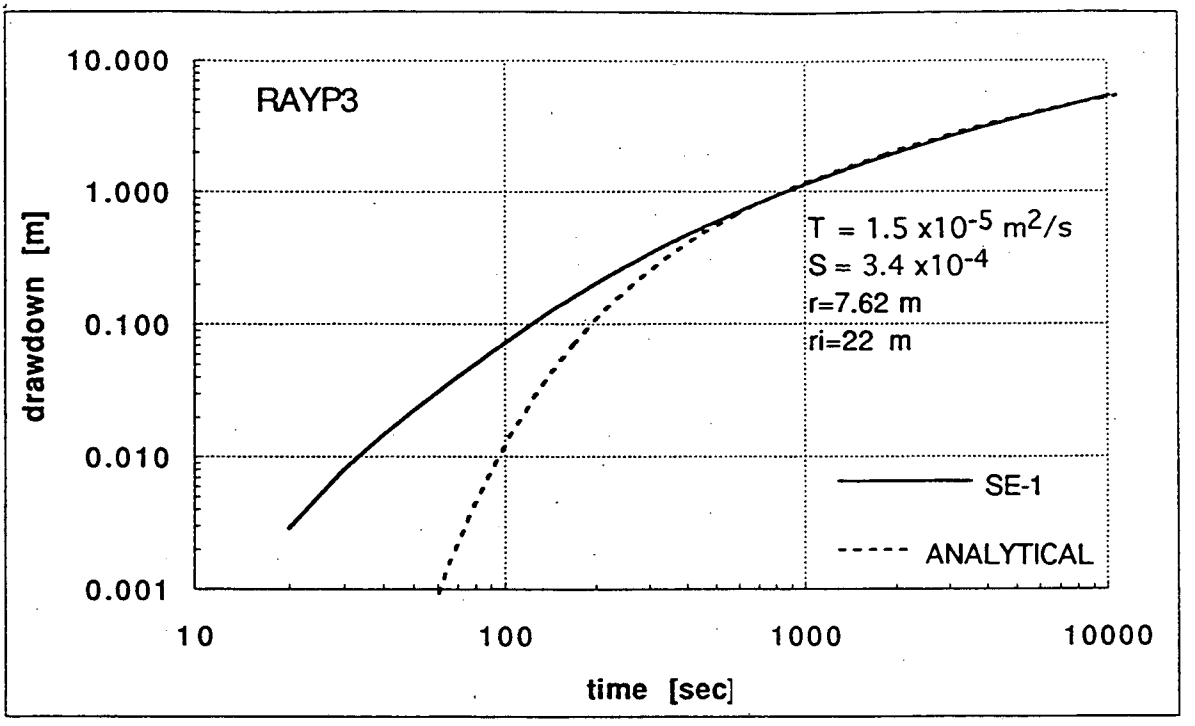

Figure 4.15. Match of analytical solution that considers impermeable boundary to drawdown in well SE-1 during test RAYP3.

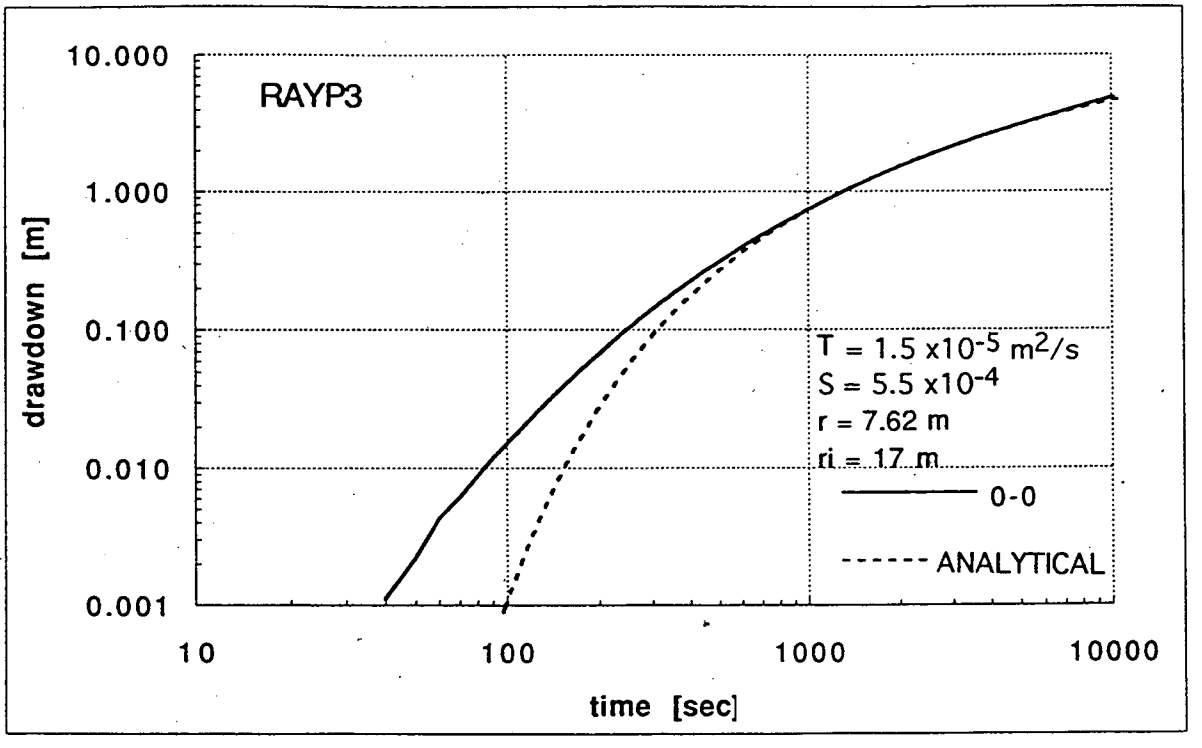

Figure 4.16. Match of analytical solution that considers impermeable boundary to drawdown in well 0-0 during test RAYP3.

The best fit to the data was found when the transmissivity calculated from the semilog analysis in the pump well was used, and when an image well accounting for the observed boundary effects during those tests were considered. The fact that the early time data does not fit the curve is again suggestive of the presence of the very high transmissivity surrounding these wells. The question is whether or not the skin zone surrounding the pumped well or a zone of high transmissivity connecting these wells could produce this early-time deviation from the Theis curve. In section 6.0 it is shown that these deviations can be produced by such anomalies, and that the analyses presented here yielded significant insight into the hydrologic structure near wells 0-0, SE-1, and SW-1. Table 4.2 summarizes the findings from the analyses in this section.

Table 4.2. Summary of drawdown analyses for all pump tests.

Test name	Well	T [m^2/s]	S	r_i [m]	r_e [m]
RAYP22	SE-1*	1.7 x10^{-5} †	2.3 x10^{-4} †	20.4	3.1
	0-0	1.7 x10^{-5} ‡	2.3 x10^{-4} ‡	24	
RAYP3	SW-1*	1.4 x10^{-5} †	2.3 x10^{-4} †	6.6	3.3
	SE-1	1.5 x10^{-5} ‡	3.4 x10^{-4} ‡	22	
	0-0	1.5 x10^{-5} ‡	5.5 x10^{-4} ‡	17	
RAY12	SW-3*	na	na		
	0-0	4.3 x10^{-6}	1 x10^{-4}		
	SW-1	4.7 x10^{-6}	1.8 x10^{-4}		
	SW-2	4.7 x10^{-6}	4.1 x10^{-4}		
	SW-4	3.4 x10^{-6}	2.4 x10^{-4}		
FLOW 0-0	0-0*	2 x10^{-5} †	2.3 x10^{-4} †	20	3.6

* pumped well

† based on including the listed r_i and r_e in the analysis

‡ based on including the listed r_i in the analysis

5.0 DOWNHOLE FLOWMETER TESTS

Downhole flowmeter tests were conducted in wells 0-0, SE-1, and SW-1. These tests consisted of pumping water from the upper portion of a well at a constant rate while simultaneously measuring the upward flow at different depths in the wellbore. The variation in the average horizontal hydraulic conductivity over different depth intervals was assessed using these tests, and further evidence that most of the flow near these wells is through the two subhorizontal fracture zones was obtained.

5.1 Approach

Molz and others (1989) proposed a relatively simple technique whereby the variation of horizontal hydraulic conductivity with depth in a horizontally layered and porous medium aquifer can be determined. Although the aquifer at Raymond does not satisfy their model precisely, it is analogous in the sense that there is confined flow restricted mainly to the two subhorizontal fracture zones.

In an ideal confined aquifer, in which the pumped well penetrates the entire aquifer thickness, water flows horizontally toward the well. Even if the aquifer is composed of horizontal layers of highly differing conductivities, flow near the well quickly becomes horizontal (Javandel and Witherspoon, 1969). After a relatively short time of pumping, drawdown in the pumped well can be expressed by the Cooper-Jacob equation (4.1). Taking the derivative of s with respect to r_w in equation (4.1) reveals that the hydraulic gradient near the well is constant in time. For this reason, a semi-steady state condition is said to exist near the pumped well when equation (4.1) becomes applicable (Matthews and Russell, 1967). Under steady conditions, the flow into the well from each layer is proportional to the transmissivity of the layer:

$$Q_i = \alpha T_i = \alpha K_i b_i \tag{5.1}$$

where α is a constant of proportionality, K is the average horizontal hydraulic conductivity over the interval b, and the subscript i denotes a particular depth interval. Since

$$Q = \sum_{i=1}^{n} Q_i = \alpha \sum_{i=1}^{n} K_i b_i = \alpha T \tag{5.2}$$

it follows from (5.1) and (5.2) that

$$K_i = \frac{TQ_i}{b_i Q} \tag{5.3}$$

From (5.3) it is apparent that all that is needed to determine the average horizontal hydraulic conductivity over a particular depth interval is the transmissivity of the entire formation thickness and the percentage of total pumped water entering the well from that interval. Deviations from the idealized case for which equation (5.3) is strictly applicable to, and their influence on the analysis is addressed in section 5.4.

5.2 Field Procedure

A schematic of the test configuration is shown in Figure 5.1. Near the top portion of the uncased wellbore, water is pumped at a constant rate to the surface via a downhole-submersible pump. A pressure transducer is situated about 1 meter above the pump, and a flowmeter-packer assembly several meters below it. This assembly is composed of a calibrated impeller-type flowmeter mounted on the top of a pipe that passes through the

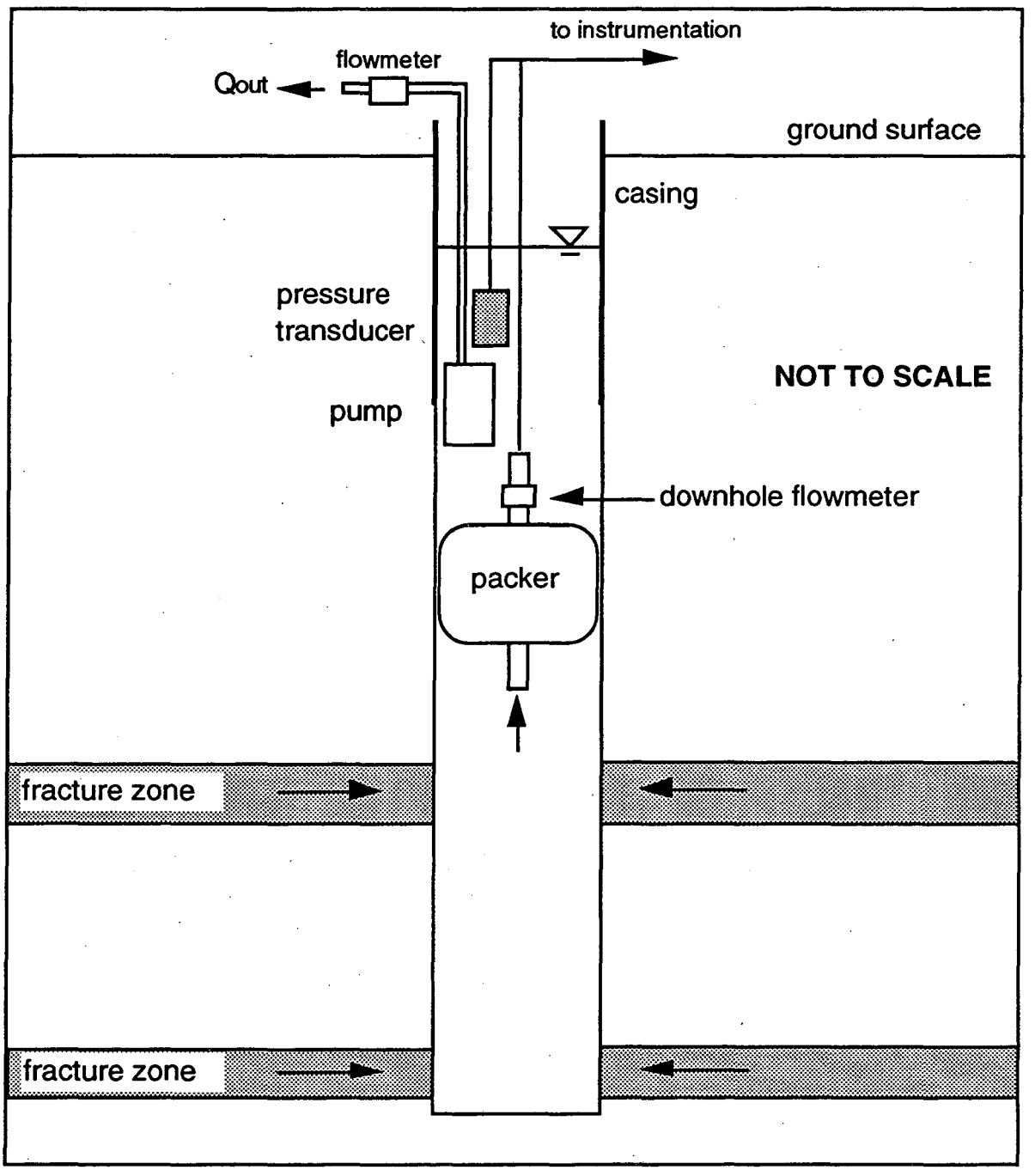

Figure 5.1. Schematic of flowmeter test configuration.

center of the packer. When the packer is inflated, the upward flow through the wellbore beneath it is restricted to pass through the pipe and flowmeter. After the flow through the packer becomes steady at this initial depth, it is deflated, lowered to another depth, and

inflated again. A measurement is taken and the procedure is repeated successively at different depths. Because the flowmeter rotates at a rate that is linearly dependent on the velocity, the flow rate is easily determined from a calibration curve.

To insure that the packer sealed the borehole, it was inflated at depths where only minor fractures were present. In addition, it was inflated to slightly higher pressures at greater depths to compensate the compression caused by the additional height of water above it. Pressure transducer data was recorded every 30 seconds. Appendix 2 shows the data collected for wells SE-1, SW-1, and 0-0.

5.3 Data Analysis and Results

Figures 5.2, 5.3, and 5.4 show the semilog drawdown plots for the flowmeter tests in well SE-1, SW-1, and 0-0. The fluctuations in water levels at later times correspond to the inflating and deflating of the packer. The transmissivity over the entire uncased wellbore for well SE-1 was found using equation (4.3) and the slope of the drawdown curve in figure 5.2. A 2 hour pump test in well 0-0 was conducted 1 hour prior to the one that is shown in figure 5.4, but it was halted because of a malfunctioning of the downhole flowmeter. The drawdown during this previous test is shown in Figure 4.6., and it is named FLOW 0-0. As exhibited by the reduced rate of drawdown during the second test (Fig. 5.4), the aquifer was still recovering from the first test. Therefore, the first test response was used to determine the transmissivity. Similarly, the test in well SW-1 followed shortly after the test in well SE-1. Therefore, the transmissivity determined from test RAYP3 was used (Fig. 4.9). The drawdown that would have occurred in well

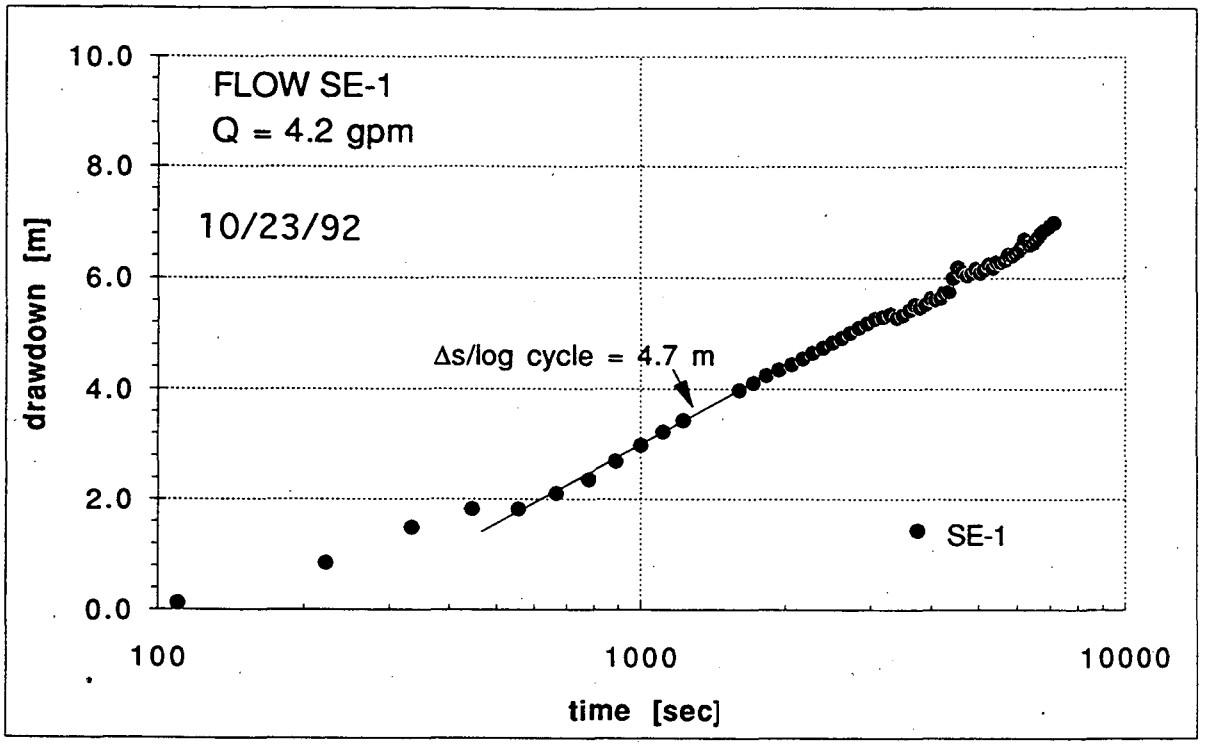

Figure 5.2. Semilog plot of drawdown vs. time in well SE-1 during test FLOW SE-1.

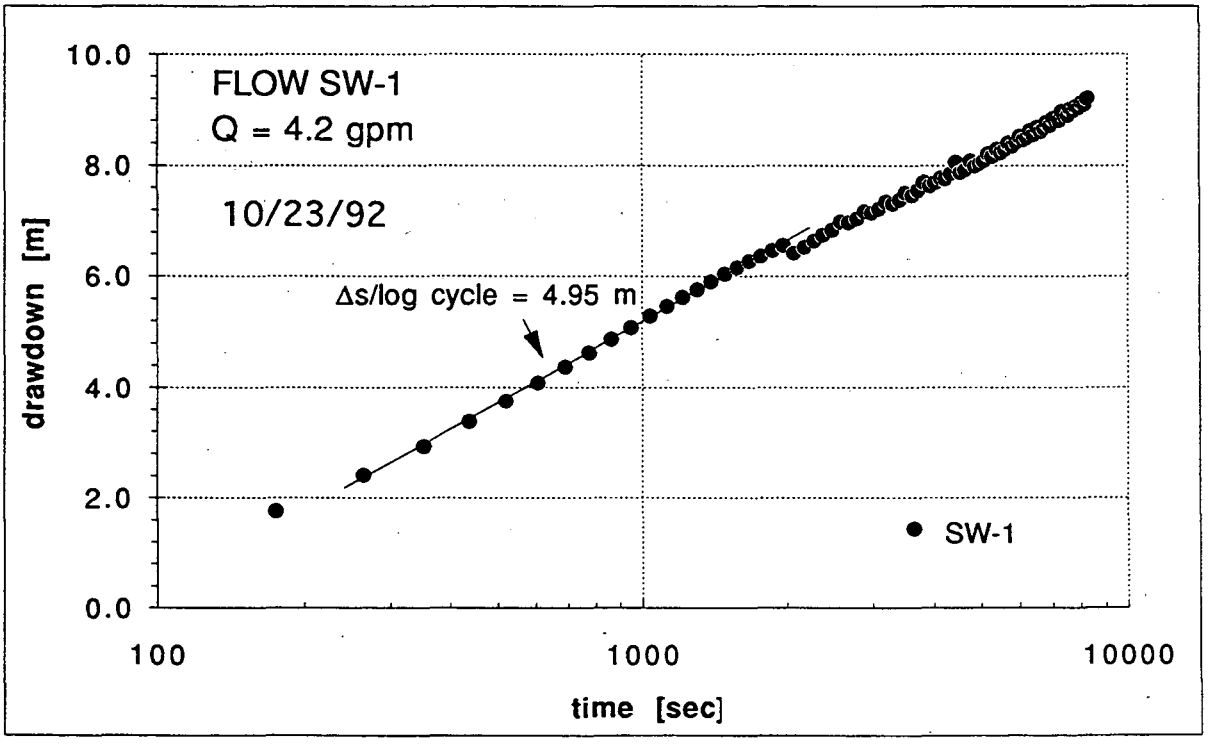

Figure 5.3. Semilog plot of drawdown vs. time in well SW-1 during test FLOW SW-1.

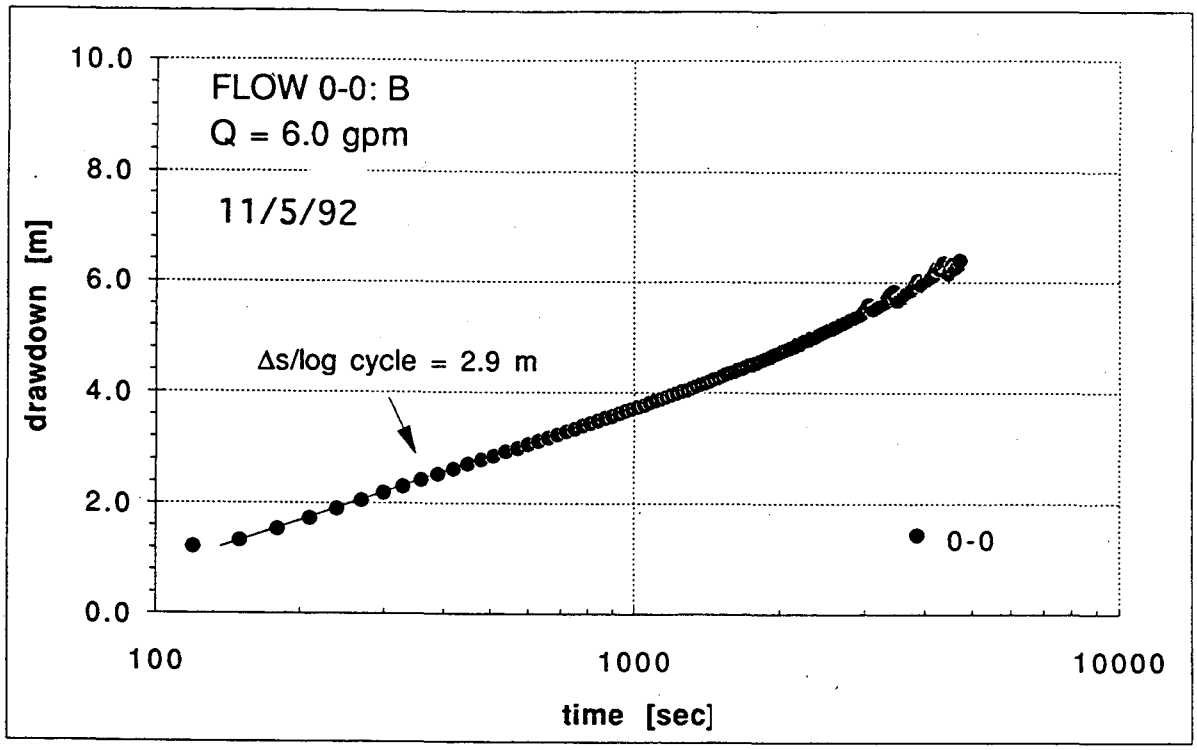

Figure 5.4. Semilog plot of drawdown vs. time in well 0-0 during test FLOW 0-0: B.

SW-1 if the test in well SE-1 had not been conducted earlier was determined by subtracting the superimposed effects of the aquifer recovery from the drawdown observed in well SW-1. The transmissivity calculated from this drawdown was the same as that calculated from test RAYP3. This shows that the mechanics of the flowmeter test did not significantly alter the drawdown response in the pump well. It is not known why the calculated transmissivity from test FLOW SE-1 is lower than the transmissivity found during test RAYP22. Perhaps it is due in part to the clogging of fractures with clayey particles as a result of the many pump tests that were conducted between test FLOW SE-1 and RAYP22. The transmissivities used for the analysis of the flowmeter data for each well are shown in Table 5.2.

Table 5.2. Transmissivity values used for flowmeter analysis.

WELL	T [m^2/s]
0-0	2.0 x10-5
SE-1	1.0 x10-5
SW-1	1.4 x10-5

Figure 5.5 shows how the discharge coming from a particular depth interval is determined from flow measurements made at different depths. Calibration of the downhole flowmeter prior to the tests in SE-1 and SW-1 showed that the impeller had a

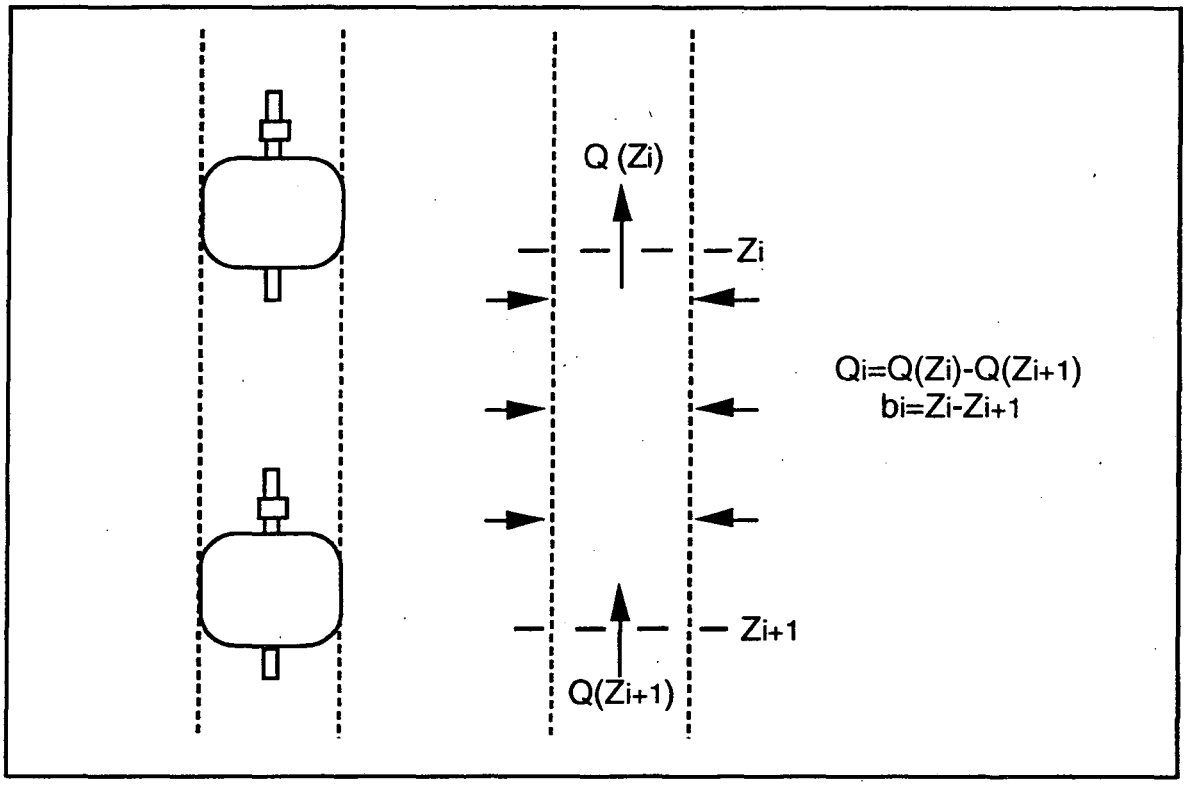

Figure 5.5. Relation between Q_i and flow measurements made at two different depths.

stall velocity below 21 rpm (1.2 gpm). Similarly, a stall velocity below 33 rpm (1.9 gpm) was found when it was calibrated after the test in 0-0. Therefore, a reading of zero rpm does not necessarily indicate that no flow entered the wellbore beneath the depth of measurement. The flow entering the well in the interval between the bottom of the well and the depth at which the lowest non-zero reading was measured was taken as the discharge recorded at that depth. Additionally, where measured downhole flow did not vary significantly between different depths, the interval between the measurements was considered a no-flow zone. This was the case for the interval between -26.8 and -63.4 m in well SW-1, for example (Appendix 2). The flow beneath the shallowest packer depth was taken as the highest value measured there. Flow entering the well in the interval between the bottom of the casing and the depth of the shallowest measurement was assumed to equal the total pump rate minus the flow measured at the shallowest depth. The calculated flow from different depth intervals for well SE-1 and SW-1 based on the above procedure is shown in Tables 5.3 and 5.4, and the calculated hydraulic conductivities of these intervals using equation (5.3) are shown in Figures 5.6 and 5.7.

A slightly different procedure was used to interpret the test results in well 0-0. From the thermal-pulse flowmeter survey it is known that a highly conductive zone is present at about -30 m. During the downhole flowmeter test the flow beneath this depth was lower than the impeller stall velocity. Therefore, a zero rpm reading was obtained at -31 m. The discharge coming from this zone is therefore impossible to calculate directly. For the purpose of showing the range of possible transmissivities for the upper and lower conducting zones, both the maximum and minimum possible flows coming from each zone were determined. The maximum flow entering from the upper zone is simply the flow measured immediately above it. The minimum is this flow minus the flow corresponding to the stall velocity of the impeller (33 rpm). These calculations and the transmissivity values associated with them are shown in Table 5.5.

Table 5.3. Calculated flow entering different depth intervals during flow meter test in well SE-1.

SE-1; Q = 4.2 gpm		
z [m]	b_i [m]	Q_i [gpm]
-15.6		
	6.2	0.20
-21.8		
	1.2	0.38
-23.0		
	1.2	0.52
-24.2		
	1.5	0.11
-25.8		
	3.4	0.18
-29.1		
	1.2	0.90
-30.3		
	0.9	0.46
-31.3		
	43.8	1.4
-75.1		

Table 5.4. Calculated flow entering different depth intervals during flow-meter test in well SW-1.

SW-1; Q = 4.2 gpm		
z [m]	b_i [m]	Q_i [gpm]
-8.7		
	12.8	0.86
-21.5		
	1.5	0.99
-23.0		
	1.5	0.11
-24.5		
	1.6	0.17
-26.1		
	1.5	0.10
-27.6		
	36.9	0.0
-64.5		
	11.2	2.0
-75.4		

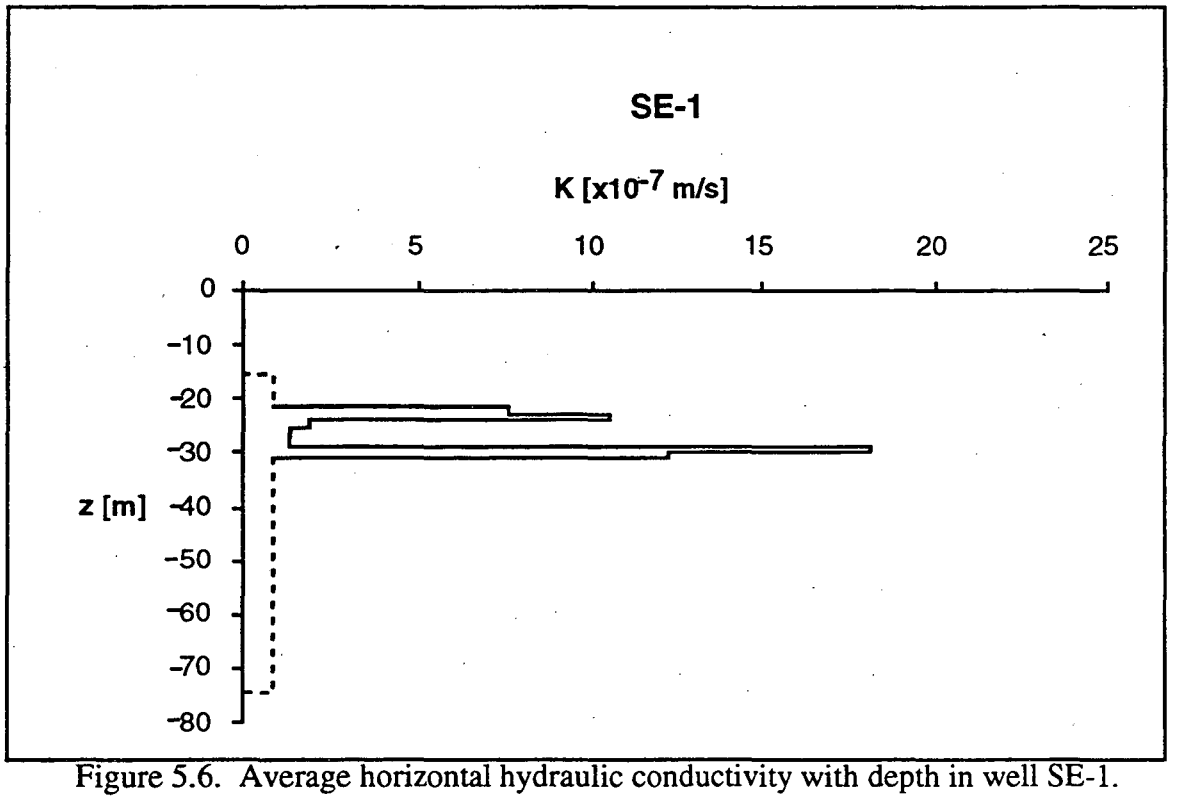

Figure 5.6. Average horizontal hydraulic conductivity with depth in well SE-1.

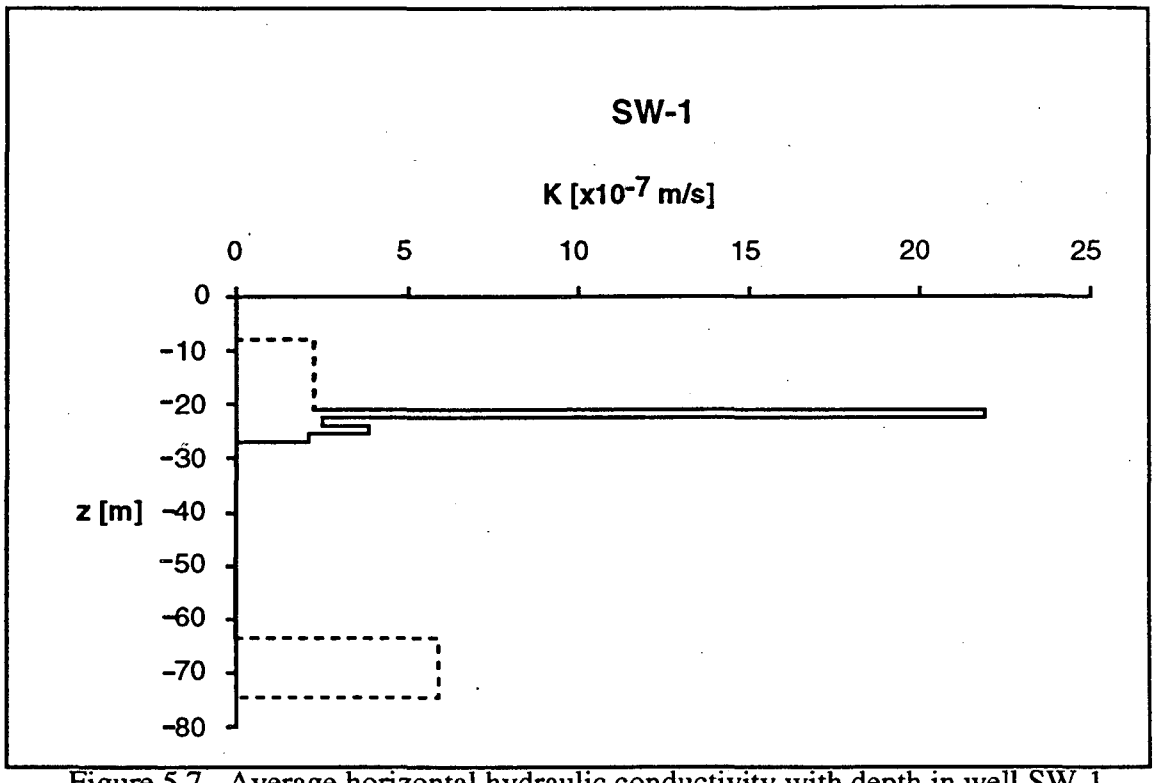

Figure 5.7. Average horizontal hydraulic conductivity with depth in well SW-1.

Table 5.5. Range of possible flow rates and transmissivities over different depth intervals in well 0-0.

z [m]	b_i [m]	max Q_i [gpm]	min Q_i [gpm]	max T_i [m^2/s]	min T_i [m^2/s]
-12.2					
	16.2	0.6	0.6	2.0 x10^{-6}	2.0 x10^{-6}
-28.4					
	3.3	5.4	3.4	18 x10^{-6}	11 x10^{-6}
-31.7					
	43.0	0.0	2.0	0	0.67 x10^{-7}
-74.7					

The above analyses assume that the well penetrates a horizontally layered and confined aquifer. Additionally, equation (4.1) assumes laminar flow to the well. It is believed that the first two assumptions are not violated significantly here because 1) the major fracture and flow zones are subhorizontal, and 2) because the shallowest major

fracture zone is well below the free water surface in the well. Additionally, pump tests performed earlier show that the aquifer behaves as confined. The potential for non-laminar flow near the well during these tests is considered in the next section.

5.4 Effects of Turbulence During Flowmeter and Pump Tests

The term well loss refers to the enhanced drawdown in a pumped well created by either non-laminar flow and/or by the presence of a well skin. The former can arise as a result of the increased flow velocities created by the convergence of flow near the well and/or by restriction of flow into narrow passages such as fractures. Skin effects were evaluated in section 4.2.3.

To check for the potential of turbulence near the wellbore, use is made of the cubic law for flow through a single smooth fracture with a constant aperture:

$$T = \frac{g b_f^{\,3}}{12 \nu} \tag{5.4}$$

where T is the transmissivity of the fracture, g is the gravitational acceleration, b_f is the fracture aperture, and ν is the kinematic viscosity of the fluid. The onset of turbulence in rock fissures commonly lies between a Reynolds number of 100 and 2300 depending on joint wall relative roughness (Elsworth, 1984). The Reynolds number is defined here as

$$\mathrm{R_e} = \frac{V_w b_f}{\nu} \tag{5.5}$$

Using equation (5.4) and the transmissivity value determined from a fully penetrating pump test, the apertures of any number of equally sized fractures intersecting the wellbore can be calculated. Using these aperture values, the borehole diameter, and the flow per fracture, the flow velocity entering the wellbore, V_w, from each of these fractures is determined. The Reynolds number associated with the flow in each fracture can then be calculated for a particular total pump rate. These calculations are shown in Table 5.6 using the transmissivity value calculated from a pump test in 0-0. Considering that flow to this well comes mostly from just several discrete zones, these calculations suggest that some degree of turbulence was likely to have been present near these wells during pumping.

Table 5.6. Reynolds number associated with flow from fractures.

	Q = 6 gpm	T = 2 x10^{-5} m^2/s	
# of fractures	aperture [m]	Vw [m/s]	Re
1	2.9 x10^{-4}	2.72	395
2	2.3 x10^{-4}	1.71	198
5	1.7 x10^{-4}	0.93	79
10	1.3 x10^{-4}	0.59	40
100	6.3 x10^{-5}	0.13	4
Vw=flow velocity at wellbore entrance	Re=Reynold's #		

Jacob (1947) accounted for the effects of well skin and turbulence into a single expression:

$$s_{(r_w,t)} = BQ + CQ^2 \tag{5.6}$$

The first term on the right side is the head loss due to laminar flow through the medium, i.e., it is simply the Theis equation, where B is equal to $W(u)/(4\pi T)$. The second term accounts for head losses due to both the turbulent flow and skin effects in the vicinity of the wellbore. Field experience in oil and gas wells indicates that the exponent 2 should be replaced by n, where n lies between unity and 2 (Ramey, 1982). However, Rorabaugh (1953) found that an n value closer to 2.5 was common in water-well testing.

Whether or not turbulent flow or skin effects around the well are significant, their influence on the drawdown in the pump well does not invalidate the determination of total transmissivity used for the downhole-flowmeter analysis. Because flow near the well becomes steady after a relatively short time of pumping, the term on the right side of (5.6) also becomes constant with time. The magnitude of this constant will simply shift the slope on the drawdown vs. logarithm of time plot, but not change it. Therefore, the calculated transmissivity remains the same regardless if there is turbulence or not.

6.0 NUMERICAL MODELING

6.1 Purpose

The purpose of using a numerical model was to test the hypothesis that the two major heterogeneities affecting the drawdowns in wells 0-0, SE-1, and SW-1 are a low conductivity zone located just west of well SW-1, and a high conductivity zone around the wells. Two different geometries of the high conductivity zone were considered: individual zones around well SE-1 and 0-0, and a single high conductivity zone encompassing all three wells. The model developed here is not intended to be used as a predictive tool.

The original intent of this modeling effort was to simulate the dual-layer structure of the aquifer. In this way, the dynamics of the flow resulting from variations in transmissivity in both layers, and from the connection of the layers by the boreholes could be considered. Much of the time spent during this study was devoted to constructing, testing, and matching field data to such a model. However, the successful development of this model was found to be too ambitious given the present understanding of the system and the limited data collected so far. Therefore, a single-layer, equivalent porous medium model was constructed instead.

6.2 Code Description

The code TRINET was used to simulate transient flow. This code was developed at Lawrence Berkeley Laboratory, and it was chosen because of its versatility and capability of handling complex three-dimensional flow geometries. Simulation of flow and transport in discretely fractured or equivalent continuum aquifers, or in combination discrete and continuum aquifers is possible. For example, the code can simulate the

upper and lower fracture zones as continuum layers which are in turn connected by several discrete fractures. As further work is carried out at the site and new information and insights are gained, the model can be continually expanded upon, and complexities such as these can be accounted for.

In TRINET, hydraulic heads are calculated at nodes which are connected by linear elements. Mathematically, an element represents a finite-dimension rectangular rod of porous material with a particular hydraulic conductivity and specific storage. Nodes and line elements can be distributed in one-, two-, or three-dimensional space, and each node is connected to at least one line element. The code solves the head distribution over the entire domain using a simple Galerkin finite element formulation for spatial discretization, and the time derivative is approximated using a finite difference scheme. When the nodes and elements are distributed on a Cartesian grid with uniform spacing in both dimensions, the model effectively simulates an equivalent porous medium. In addition, it was found that the radius of the fictitious well represented by a node that is assigned a flux condition is equal to approximately 0.2 the grid spacing. This finding is consistent with that of Peaceman (1978). When the spacing between nodes is sufficiently small, radial flow can be simulated with a high degree of accuracy even at small times and close to the pumped well.

6.3 Grid Layout and Code Verification

The grid used for the simulations is shown in Figure 6.1. In order to simulate the drawdowns in the pumped wells, the innermost region of the grid was assigned a spacing that is 5 times the radius of wells 0-0, SW-1, and SE-1. Wellbore storage is not accounted for in the present model. For the purpose of conserving CPU time and space, the nodal spacing and element lengths increase geometrically away from the center of the

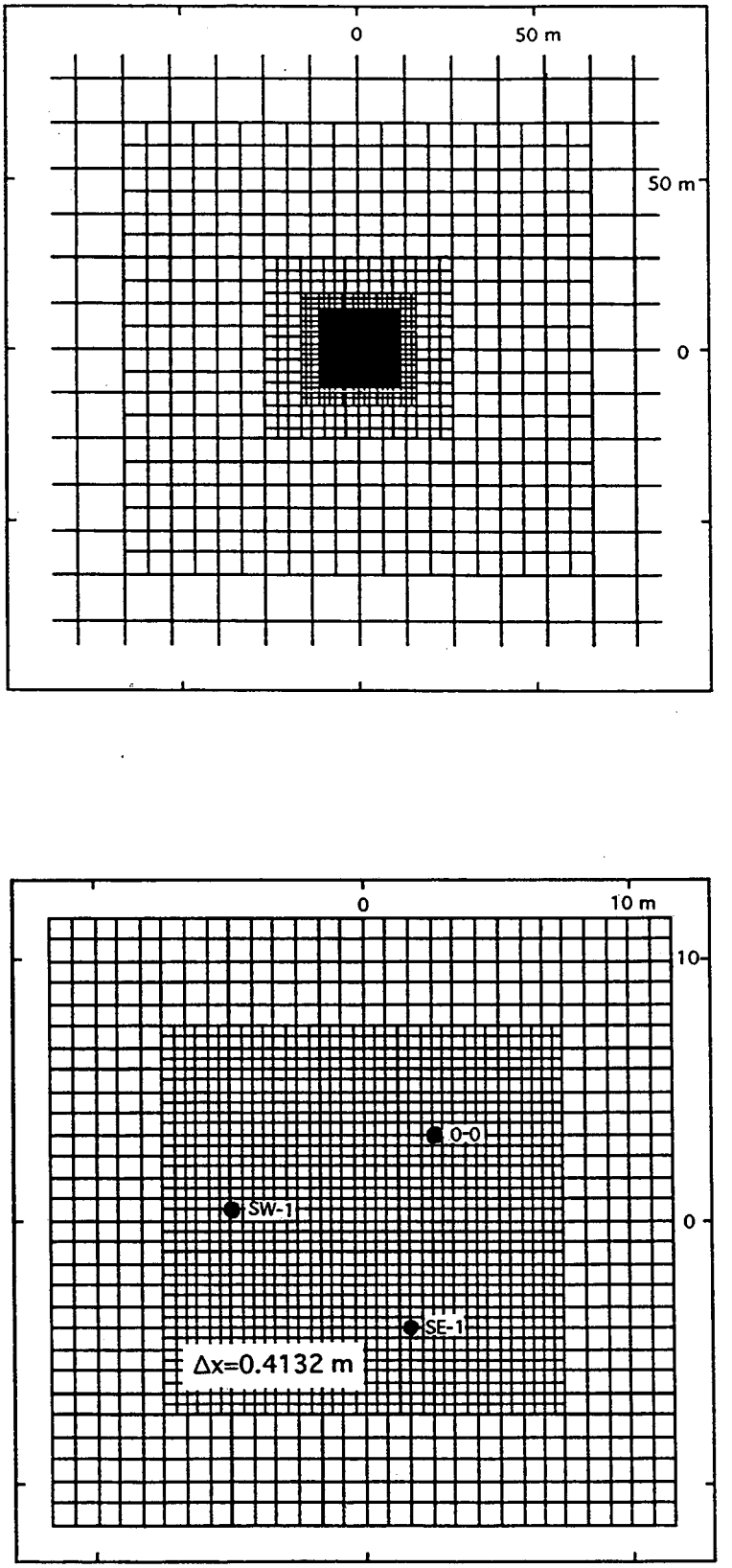

Figure 6.1. Two-dimensional grid of nodes and elements used in TRINET simulation. The figure shows the distribution of the line elements. Nodes are located at the intersections of these elements.

grid by a factor of two. This expansion does not introduce significant errors into the calculated head distribution. The entire grid represents a domain that is 172 x 172 meters in size, and the nodes on the boundaries of the grid are assigned constant head conditions. The dimensions of the grid are sufficiently large so that the boundaries do not affect the drawdowns in the well field for the pumping times considered.

The capability of the model to effectively simulate radial flow in a confined aquifer is shown in Figure 6.2. This figure shows the numerical solution for the drawdown in a homogeneous and isotropic medium at the node corresponding to pump well SE-1, and at the node corresponding to well 0-0. The transmissivity and storativity of the model is the same as is used in the simulations. The analytical solution is shown superimposed on these curves. The relative errors in the simulated drawdowns become less than 1% after 100 seconds of pumping.

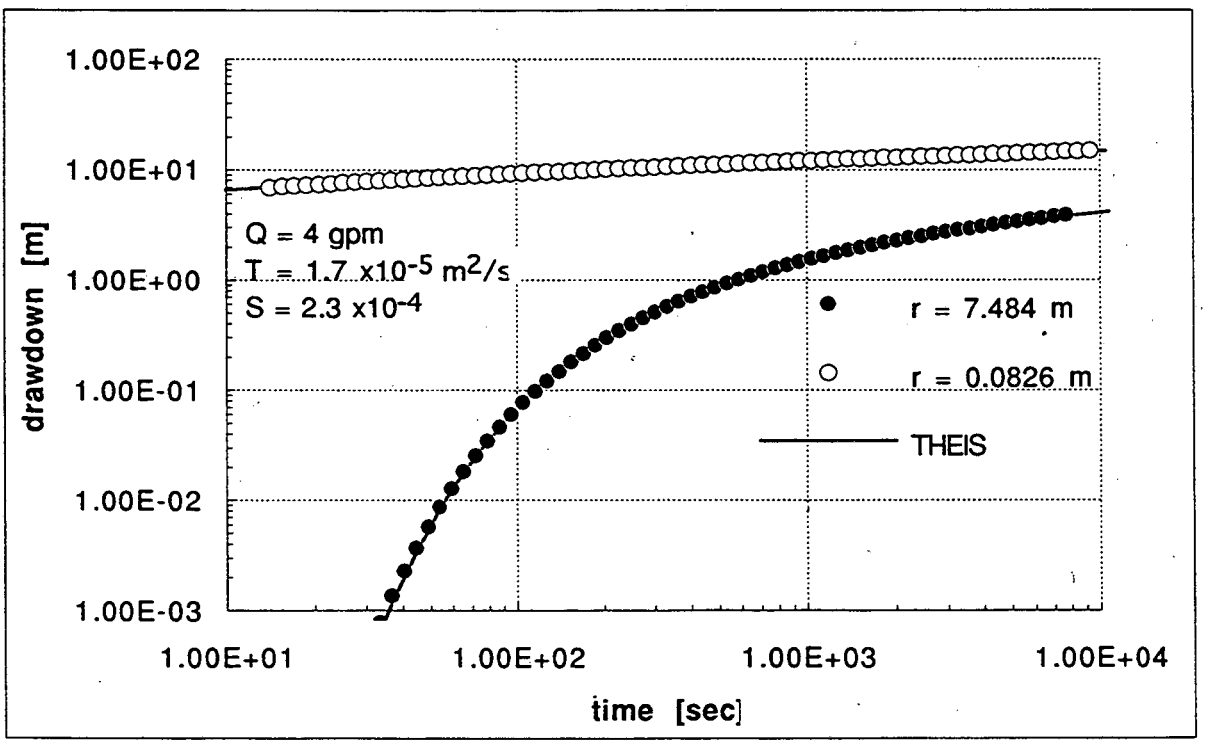

Figure 6.2. Comparison of numerical and analytical solution for drawdown in pumped well (r=0.0826 m), and in an observation well.

6.4 Assignment of Properties to Model Grid

Using the calculated distance to the impermeable boundary from wells 0-0, SW-1, and SE-1, and the average transmissivity and storativity value of the formation inferred from the analyses of the drawdowns in these wells (shown in Figs. 4.7, 4.8, and 4.9), the basic structure of the model was designed (Fig. 6.3). The low conductivity zone behind the boundary is simulated as a region with a transmissivity that is 100 times less than that in the more conductive region. The calibration of the model to actual drawdown data was begun by assuming an annular zone of greater conductivity around well 0-0 and SE-1. The radii of these zones were those shown in Figure 4.7 and 4.8, and they were assigned a transmissivity 100 times greater than the surrounding formation. The initial numerical model was therefore a simplified version of the conceptual model suggested in section 4: a linear impermeable boundary to the west of well SW-1, and zones of higher transmissivity around two of the three wells.

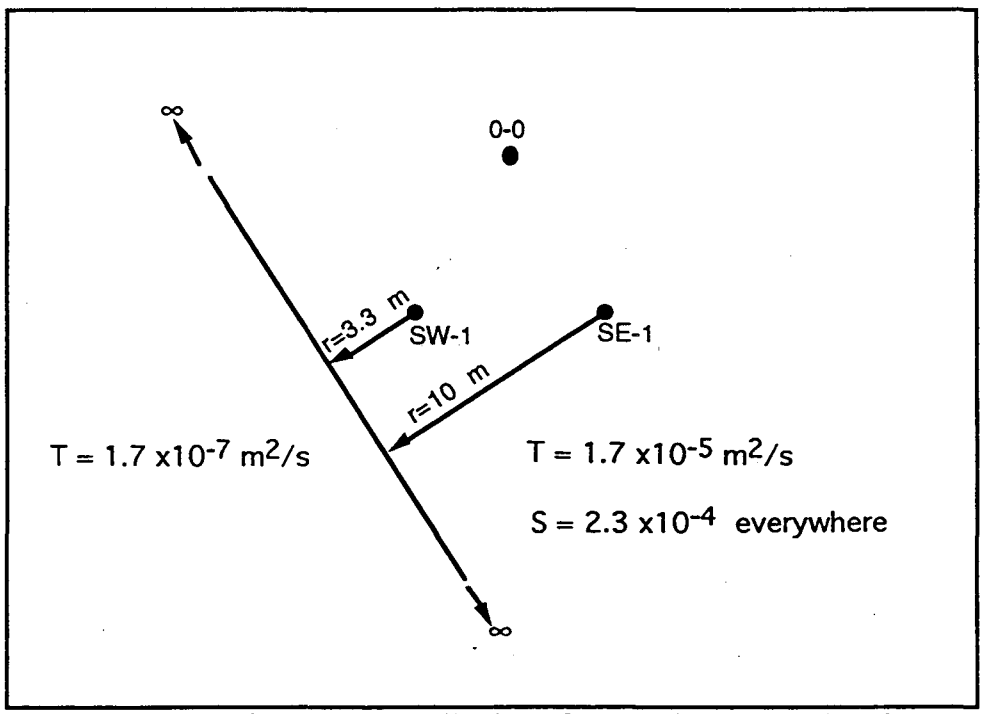

Figure 6.3. Schematic of the basic distribution of properties assigned to the numerical model.

6.5 Simulation Results

Simulations of tests RAYP3 and FLOW 0-0 were conducted, and the calculated drawdowns in wells SE-1 and 0-0 were compared to the actual drawdowns. The sizes of the high conductivity zones around each well were systematically changed until reasonable fits were obtained. Figure 6.4 shows the model that accounted for the observed drawdown in the three wells, and Figures 6.5, 6.6, and 6.7 show the matches to the data. The positive deviation of the simulated drawdown in the pump wells at early times partly results from the fact that the numerical model does not account for wellbore storage.

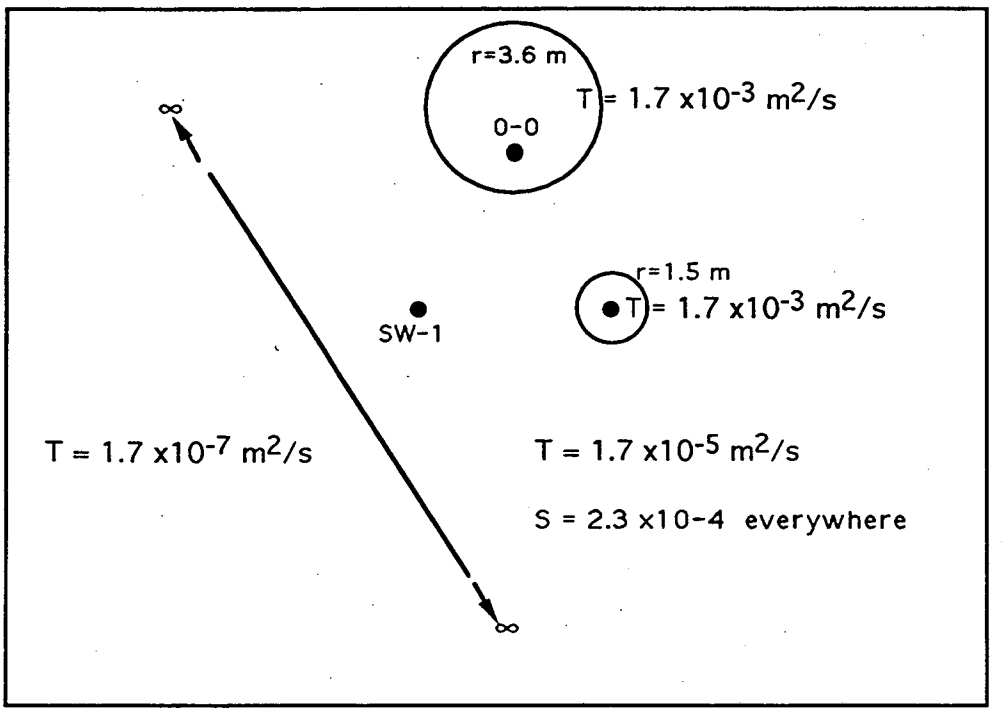

Figure 6.4. Schematic of model that accounts for observed drawdowns during tests RAYP22 and FLOW 0-0.

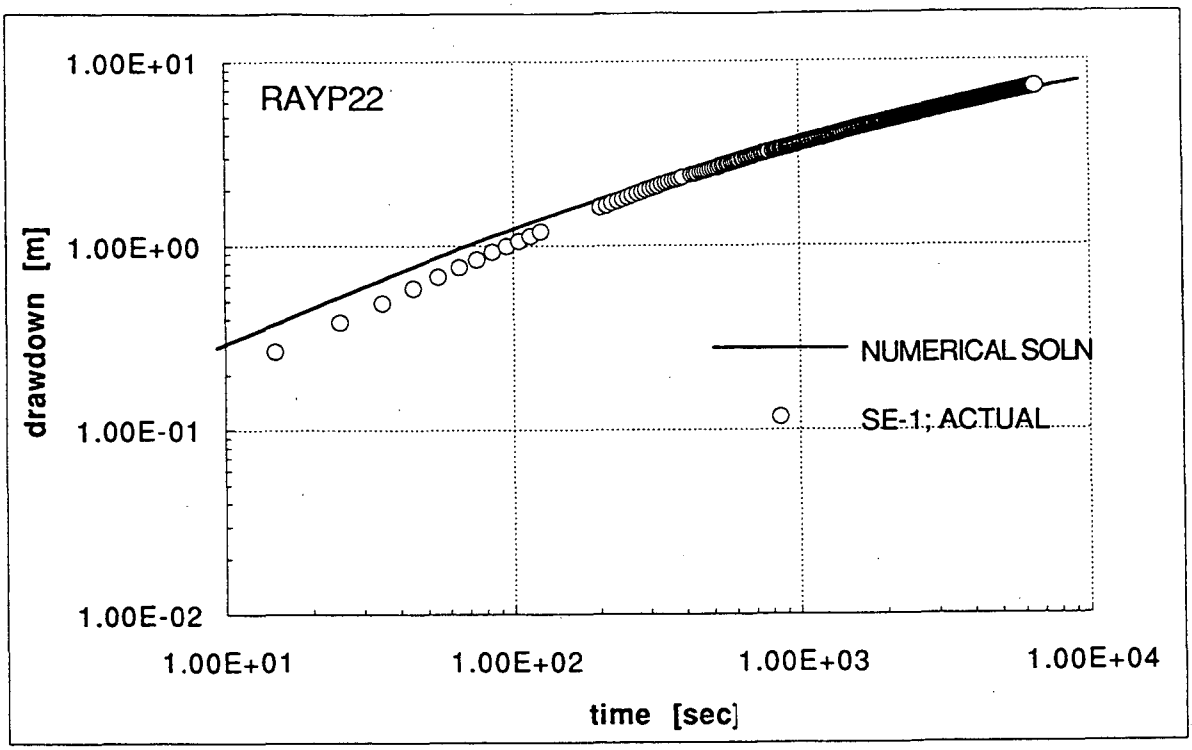

Figure 6.5. Simulated drawdown at pumped well SE-1 compared to actual drawdown during test RAYP22.

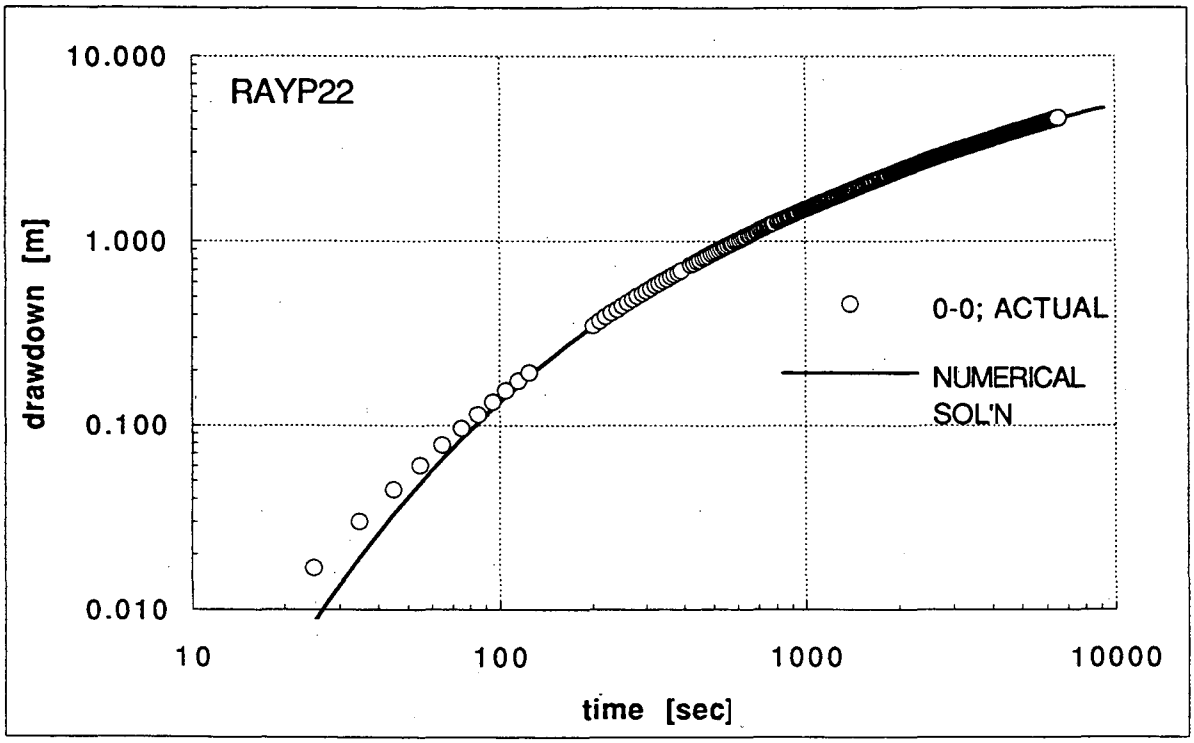

Figure 6.6. Simulated drawdown at observation well 0-0 compared to actual drawdown during test RAYP22.

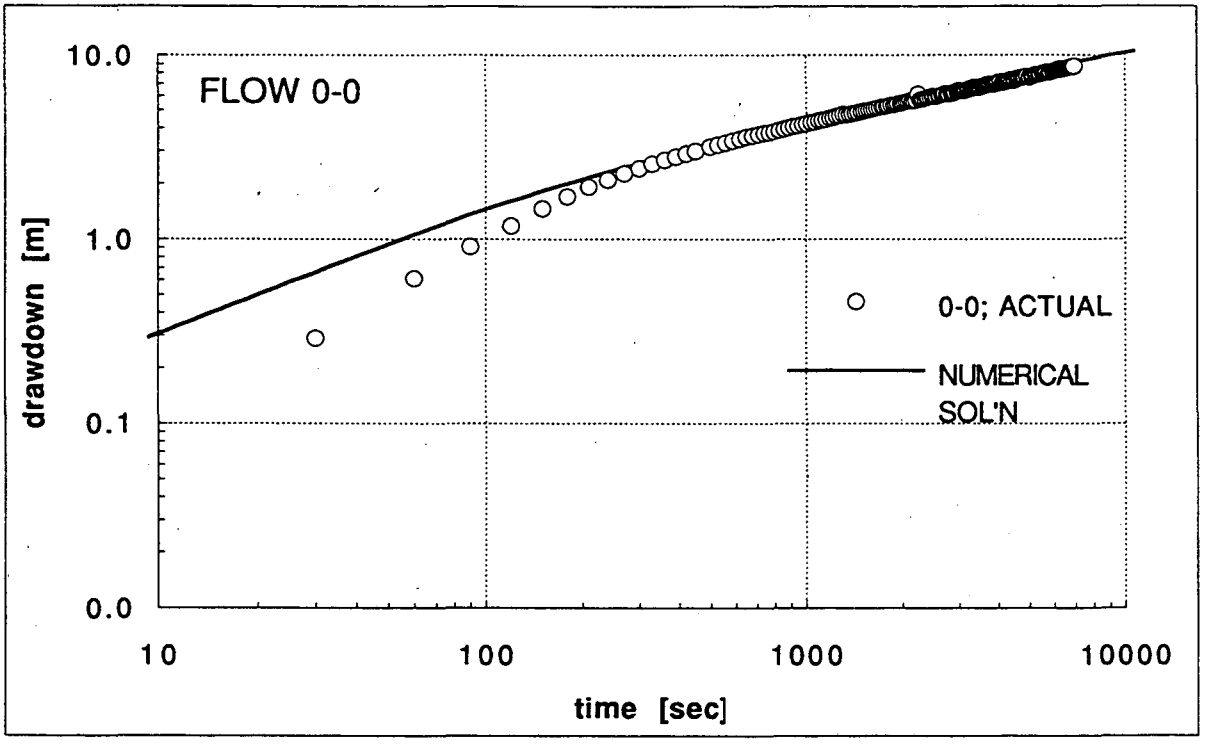

Figure 6.7. Simulated drawdown at pumped well 0-0 compared to actual drawdown during test FLOW 0-0.

Of course, the actual transmissivity distribution in reality is not exactly like that shown in Figure 6.4. A continuous conductive zone within which gradations in the transmissivity exist is more physically realistic. This fact was established by conducting numerical simulations assuming that a circular zone of higher conductivity surrounds all three wells (Figure 6.8). Regardless of the magnitude of increased transmissivity in this inner zone (Ti), the simulated drawdowns were consistently over predicted at observation well 0-0. Figures 6.9 and 6.10 show the simulated drawdowns compared to actual drawdowns during test RAYP22 for several different Ti values. Even if the size of the inner circular zone is increased, the drawdown in the observation well is over predicted.

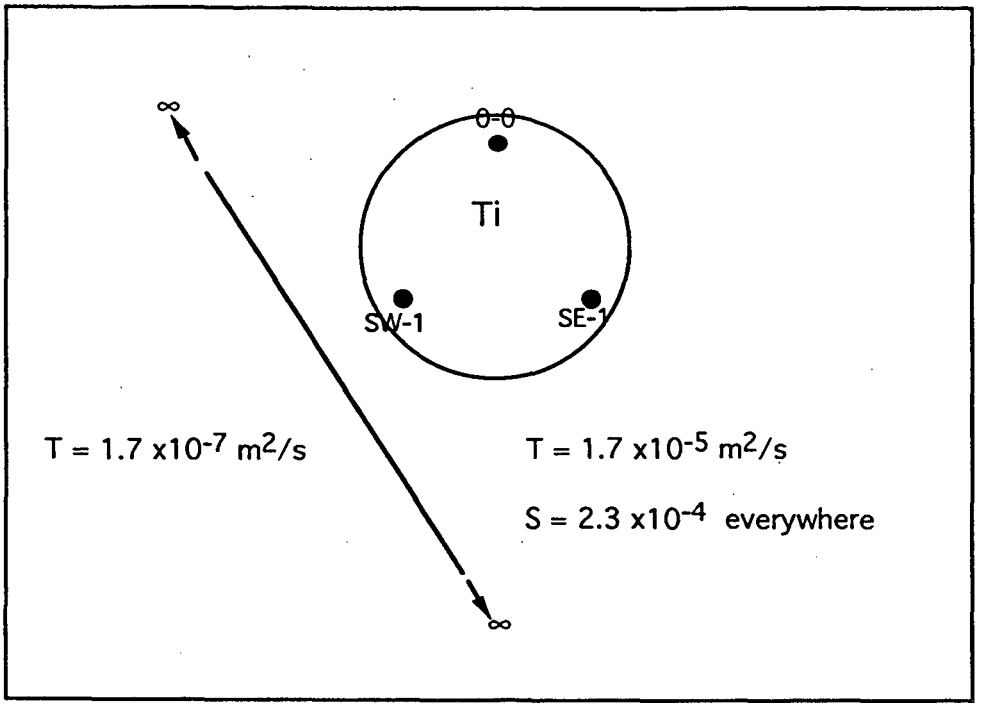

Figure 6.8. Schematic of numerical model in which all three wells are enclosed in a zone of constant transmissivity Ti.

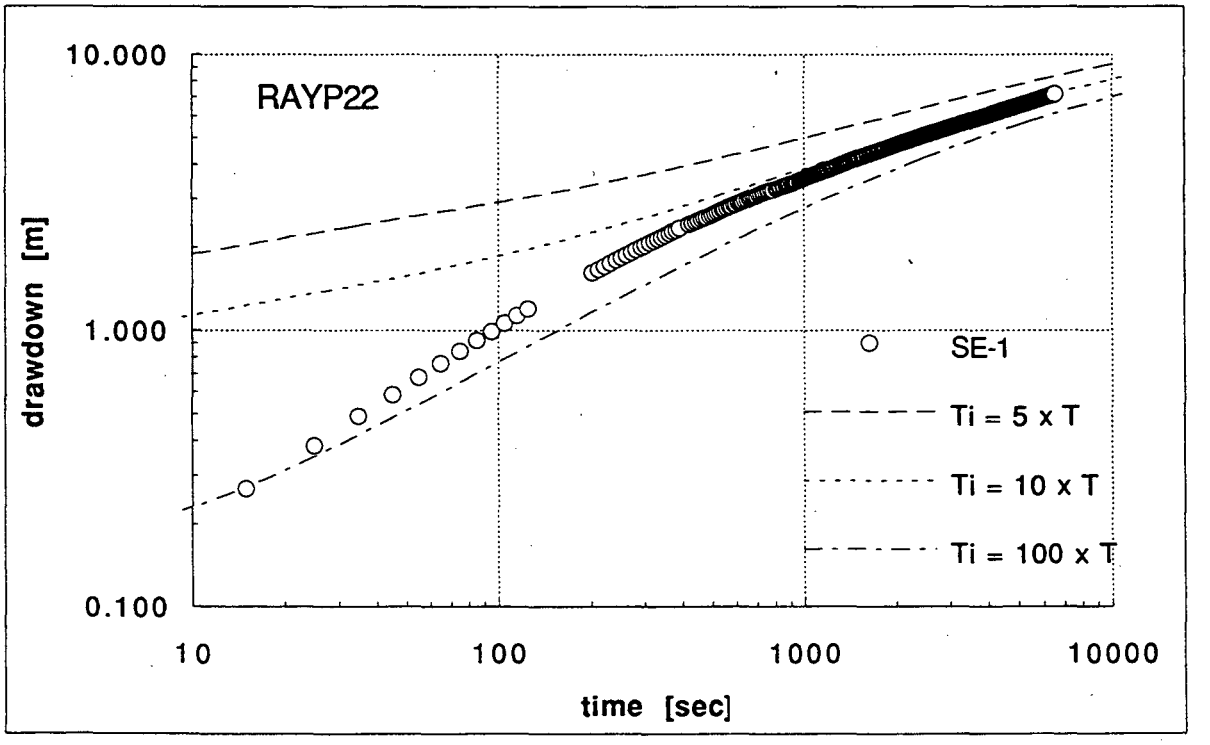

Figure 6.9. Simulated drawdown in pumped well SE-1 using numerical model shown in Figure 6.8.compared to actual drawdown during test RAYP22

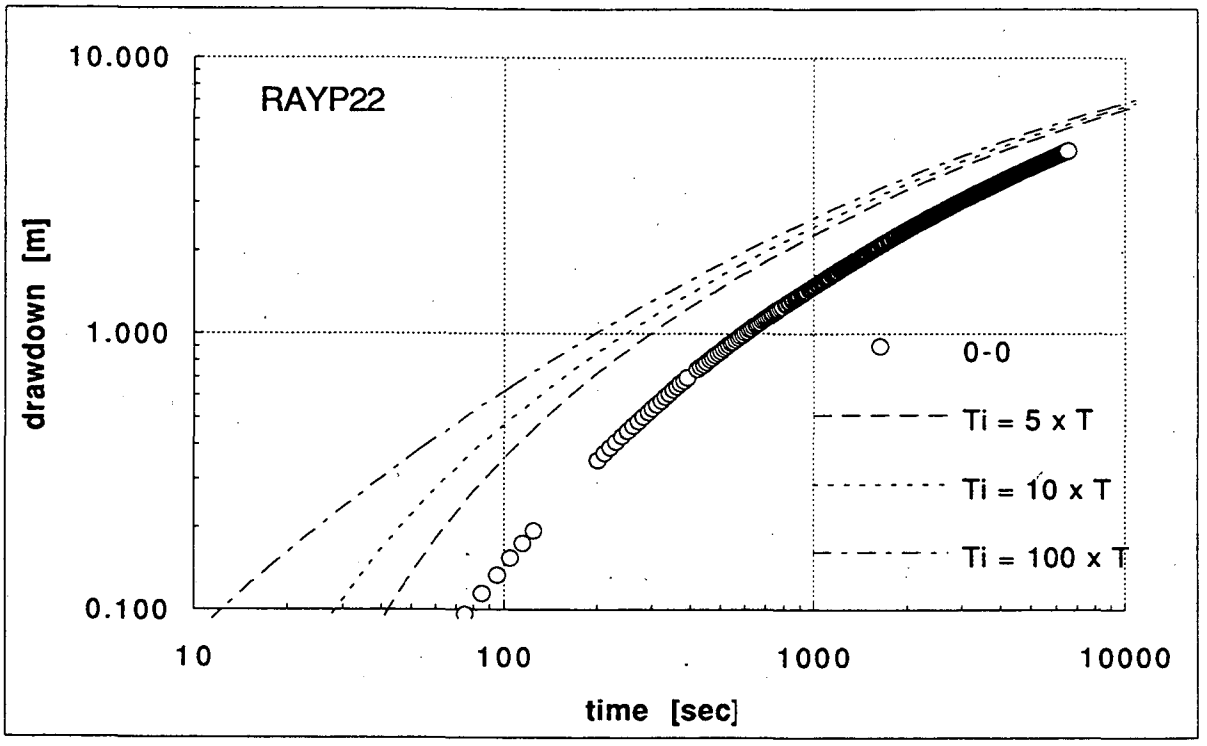

Figure 6.10. Simulated drawdown in observation well 0-0 using numerical model shown in Figure 6.8 compared to actual drawdown during test RAYP22.

In comparison, the model shown in Figure 6.4, which was first formulated from an analytical analysis, can account for the observed drawdowns in 3 wells during two different tests. These findings suggest that a distribution of properties similar to that shown in Fig. 6.4, but in which subtle variations in conductivity exist, is a feasible conceptual model. In order to further evaluate this model, results from the test conducted in well SW-1 should also be matched to the numerical model. This would require that a zone of higher conductivity be included near well SW-1, and that the dimensions and conductivities of the zones near the other wells be modified. An optimization program that systematically alters these properties, and which incorporates a sensitivity analysis would be a very appropriate technique to help achieve a match to the rest of the data.

7.0 SUMMARY AND CONCLUSIONS

In this study, the hydrogeologic structure and properties of a small portion of a fractured granitic rock aquifer near Raymond, California were assessed based on geophysical logs and hydrologic tests collected and performed in several closely spaced wells. The methodologies and findings are summarized below.

Subsurface fractures at the site were measured in wells 0-0, SE-1, and SW-1 from acoustic televiewer logs. This mapping identified three distinct sets of fractures: two nearly orthogonal and subvertical fractures that strike east-northeasterly and southeasterly, and a set that dips westwardly and subparallel to the topographic surface. The occurrence of these sets is consistent with the regional geology and geologic history. This suggests that the two subvertical sets are tectonic fractures, and that the subhorizontal set is comprised of unloading fractures.

The inferred general hydrogeologic structure of the aquifer is based on the detailed study of the fracture sets present, the correlation of the unloading fractures to the more highly weathered zones adjacent to the boreholes, and on visual inspection of the apparent resistivity and thermal-pulse flowmeter logs in all wells. Zones where the apparent resistivity is less than 700 ohm-m coincide with the occurrence of the unloading fractures. This indicates that, in the area near the three wells, these fractures are more weathered than the others. Simultaneous observation of the apparent resistivity logs in all wells reveals that there are generally two continuous and subparallel zones with apparent resistivities less than 700 ohm-m. The dip direction of these two zones is the same as that of the unloading fractures. Thermal-pulse flowmeter logs show that the major flow zones intersecting these wells mostly occur within the two weathered zones. These observations support the conclusion that the aquifer is generally composed of two

subhorizontal and nearly parallel hydraulically conductive zones of unloading fractures that dip approximately 15° to the west and that are separated by about 25 meters (Figure 3.13).

Pumping tests were conducted to obtain estimates of the transmissivity and storativity of the aquifer. The location of relatively high and low transmissivity zones was also inferred from these tests. Analysis of the drawdown responses in the three wells when each acted as the pumped well shows that a low conductivity zone is located just west of well SW-1, and that the zones around each of these wells has a significantly greater conductivity than that of the surrounding formation. This is most probably due to the presence of the 2 major fracture zones intersecting these wells, and to the increased conductivity in these zones near the wells as a result of drilling disturbances. The drawdowns in the pumped wells were matched almost exactly by an analytical solution that considers the presence of the low conductivity zone (considered as a linear impermeable boundary), and the high conductivity zone around each pump well. These analyses showed that the combined effects of the low conductivity boundary and of the high transmissivity zone could be two of the major heterogeneities located in the region near these wells. The average transmissivity and storativity of the aquifer in the region outside the low conductivity zone are 1.7×10^{-5} m^2s^{-1} and 2.3×10^{-4}, respectively.

Downhole flowmeter tests were conducted in each of the three wells. The flow entering the wellbore below different depths while it was being pumped at a constant rate was measured. The average horizontal hydraulic conductivity over different depth intervals was calculated from these measurements. These tests provided further evidence that flow is confined to the two subhorizontal fracture zones. The test results could be useful in validating a numerical model of the aquifer that accounts for its dual-layer structure.

A numerical model was constructed for the purpose of testing the hypothesis that the low conductivity zone located to the west of well SW-1, and the relatively high conductivity zones around the wells are the two major heterogeneities located near these wells. The aquifer was modeled as a single layer, equivalent porous medium with a transmissivity and storativity equal to the average value found from the drawdown analyses. The low conductivity boundary was modeled as the edge of a region with a transmissivity 100 times less than the surrounding formation, and it was placed to the west of the wells at the distances calculated by the drawdown analyses. The high conductivity zones around wells 0-0 and SE-1 were modeled as circular zones with transmissivities 100 times greater than the surrounding formation. The actual drawdown in both these wells during two different pumping tests were matched using this model, and this provides further evidence that the inferred distribution of properties near the three wells is a reasonable working hypothesis.

7.1 Suggestions for Future Work

Future work should be aimed at describing the spatial distribution of hydrologic properties within each of the two major fracture zones. The following suggestions are made:

• If the resources are available, inflatable packers should be installed simultaneously in several wells approximately halfway between the upper and lower major fracture zones. Pressure transducers should then be installed within each isolated zone. Pumping and/or injection tests can then be conducted within each layer. It may be possible to infer the locations of relatively high and low conductivity zones within each layer from analysis of the pressure transient responses within each layer in a way similar

to that shown in Section 4. At least three nearby wells situated at different angles from the pumping or injection source should be monitored so that the results can be analyzed for anisotropy. The suite of wells equipped with instrumentation should then be moved to different wells so that different portions of the aquifer can be sampled. The observed drawdowns within the lower fracture zone during pumping from this zone may yield information regarding the degree, if any, of hydraulic connection between the upper and lower fracture zones.

• If tracer tests are conducted, they should similarly be conducted within each packed-off fracture zone.

• The numerical model should be modified so that the dual-layer structure of the aquifer is accounted for. Each layer could be modeled as a two-dimensional porous medium with a particular transmissivity and storativity distribution. Vertical elements can be included to account for the connection of the layers by the wells. It would be very interesting to investigate how the connection of the layers by the wells influences the drawdown response in a well during a fully-penetrating pumping test.

• If additional boreholes are drilled, they should be done so with an air-rotary drill, and borehole cores should be collected. The infilling of fractures can then be analyzed, thereby providing additional information regarding the properties of each fracture set. With the suite of geophysical logs from this well, and knowledge of the properties of individual fractures, a better assessment of the properties of fractures intersecting the other wells could be made based on their geophysical logs.

REFERENCES

Balk, R., 1937. Structural behavior of igneous rocks, Geological Society of America Memoir 5, 177 pp.

Bateman, P. C., and C. Wahrhaftig, 1966. Geology of the Sierra Nevada, *in* Bailey, E. H., ed., Geology of northern California, California Division of Mines and Geology Bulletin 190, 107-172.

Bateman, P. C., and W. N. Sawka, 1981. Raymond quadrangle, Madera and Mariposa counties, California-analytic data, U. S. Geological Survey Professional Paper #1214, U. S. Geological Survey, Washington, D. C.

Bateman, P. C., Busacca, A. J., Marchand, D. E., and W. N. Sawka, 1982. Geologic map of the Raymond quadrangle, Madera and Mariposa counties, California, Map GQ-1555, United States Geological Survey, Department of the Interior, 1982.

Billings, M. P., 1972. "Structural Geology." Prentice-Hall, Inc., New Jersey, 606 pp.

Bixel, H. C., Larkin, B. K., and H. K. van Poollen, 1963. Effect of linear discontinuities on pressure build-up and drawdown behavior, *J. Pet. Tech., 228,* 885-895.

Carlsson, A., and T. Olsson, 1981. Hydraulic properties of a fractured granitic rock mass at Forsmark, Sweden, *in* Ground water in hard rocks, International Hydrological Programme, Project 8.6 of the International Hydrological Programme, prepared by the project panel, Ingemar Larsson, chairman, Paris, 1984, 228 pp.

Chernyshev, S. N., and W. R. Dearman, 1991. "Rock Fractures." Butterworth-Heinemann, London, 272 pp.

Cooper, H. H., and C. E. Jacob, 1946. A generalized graphical method for evaluating formation constants and summarizing well-field history, *Trans. Amer. Geophys. Union, 27*, 526-534.

Davies, R. K., and D. D. Pollard, 1986. Relations between left-lateral strike-slip faults and right-lateral monoclinal kink bands in granodiorite, Mt. Abbot quadrangle, Sierra Nevada, California, *Pure and Applied Geophysics, 124,* 177-201.

Davison, C. C., Keys, W. S., and F. L. Paillet, 1982. Use of borehole-geophysical logs and hydrologic tests to characterize crystalline rock for nuclear-waste storage, Whiteshell Nuclear Research Establishment, Manitoba, and Chalk River Nuclear Laboratory, Ontario, Canada, Office of Nuclear Waste Isolation, Technical Report ONWI-418, U. S. Department of Commerce, Springfield, VA, 103 pp.

Di Nitto, R. G., Norman, W. R., and M. M. Hanley, 1982. An approach to investigating groundwater contaminant movement in bedrock aquifers: case histories, *in* National Conference on Management of Uncontrolled Hazardous Waste Sites, November 29-December 1, 1982, Washington, D. C., Hazardous Materials Control Research Institute, pp. 111-117.

Dott, R. H., Jr., and R. L. Batten, 1988. "Evolution of the Earth." McGraw-Hill, Inc., New York, 643 pp.

Ellsworth, D., 1984. Laminar and turbulent flow in rock fissures and fissure networks, Ph.D. thesis, University of California at Berkeley, Berkeley, CA.

Fortin, R. L., 1988. Control and remediation of volatile organic chemical migration in fractured bedrock, *in* HWHM 88: Hazardous wastes and hazardous materials, proceedings of the 5th national conference held April 19-21, 1988, Las Vegas, Nevada, pp. 29-33.

Gale, J. E., 1982. Assessing the permeability characteristics of fractured rock, *in* Narasimhan, T. N., ed., Recent Trends in Hydrogeology, Special Paper 189, *Geol. Soc. Amer.*, 163-181, 1982.

Gringarten, A. C., and P. A. Witherspoon, 1972. A method of analyzing pump test data from fractured aquifers, *Proc.,* Symposium on Percolation Through Fissured Rock, International Society for Rock Mechanics, Stuttgart, Sept. 18-19, 1972.

Hawkins, M. F., Jr., 1956. A note on the skin effect, *Trans., AIME, 207,* 356-357.

Hess, A. E., 1986. Identifying hydraulically-conductive fractures with a low-velocity borehole flowmeter, *Canadian Geotech. J., 23*(4), 69-78.

Huber, N. K., 1987. The geologic story of Yosemite National Park, U. S. Geological Survey Bulletin, 1595, 64pp.

Hurst, W., 1953. Establishment of the skin effect and its impediment to fluid flow in a wellbore, *Pet. Eng., 5,* B6-B16.

Jacob, C. E., 1947. Drawdown test to determine effective radius of artesian wells, *Amer. Soc. Civ. Engin. Trans., 112*, 1047-1070.

Javandel, I., and P. A. Witherspoon, 1969. A method of analyzing transient fluid flow in multilayered aquifers, *Water Resour. Res., 5,* 856-869.

Jones, J. W., Simpson, E. S., Neuman, S. P., and W. S. Keys, 1985. Field and theoretical investigations of fractured crystalline rock near Oracle, Arizona, NUREG/CR-3736, Nuclear Regulatory Commission, 1985.

Keys, W. S., 1990. Borehole geophysics applied to ground-water inverstigations, *in* Techniques of Water-Resources Investigations of the United States Geological Survey, bk 2, chp. E2, U. S. Geologic Survey, Denver, CO.

Lockwood, J. P., and J. G. Moore, 1979. Regional deformation of the Sierra Nevada, California, on conjugate microfault sets, *J. Geophys. Res., 84,* B11, 6041-6049.

Loucks, T. L., and E. T. Guerro, 1961. Pressure drop is a composite reservoir, *Soc. Pet. Eng. J., 222,* 170-176.

Mackay, D. M., and J. A. Cherry, 1989. Groundwater contamination: Pump-and-treat remediation, *Environ. Sci. Tech., 23*(6), 630-636.

Marre, J., 1986. "The structural analysis of granitic rocks." Elsevier Publishing, New York, 123 pp.

Marsily, G. de, 1986. "Quantitative Hydrogeology." Academic Press, Inc., London, 440 pp.

Martel, S. J., Pollard, D. D., and P. Segall, 1988. Development of simple strike-slip fault zones, Mount Abbot quadrangle, Sierra Nevada, California, *Geol.Soc. Amer. Bull., 100*, 1451-1465.

Matthews, C. S., and D. G. Russell, 1967. "Pressure buildup and flow tests in wells." American Institute of Mining, Metallurgical, and Petroleum Engineers, Inc., Storm Printing Corp., Dallas, TX, 167 pp.

Mayo, E. B., 1941. Deformation in the interval Mt. Lyell-Mt. Whitney, California, *Geol. Soc. Amer. Bull., 94,* 563-575.

Mitten, H. T., LeBlanc, R. A., and G. L. Bertoldi, 1970. Geology, hydrology, and quality of water in the Madera area, San Joaquin Valley, California, U. S. Geological Survey open-file report, Water Resources Division, Menlo Park, California, 1970.

Molz, F. J., Morin, R. H., Hess, A. E., Melville, J. G., and O. Guven, 1989. The impeller meter for measuring aquifer permeability variations: evaluation and comparison with other tests, *Water Resour. Res, 25*(7), 1677-1683.

Nelson, R. A., 1985. "Geologic analysis of naturally fractured reservoirs." Gulf Publishing, Houston, Texas, 320 pp.

Neuman, S. P., Walter, G. R., Bentley, H. W., Ward, J. J., and D. D. Gonzalez, 1984. Determination of horizontal aquifer anisotropy with three wells, *Groundwater, 22*(1), 66-72.

Norris, R. M., and R. W. Webb, 1976. "Geology of California." John Wiley & Sons, Inc., New York, 365 pp.

Paillet, F. L., Keys, W. S., and Hess, A. E., 1985. Effects of lithology on televiewer-log quality and fracture interpretation, *in* Society of Professional Well Log Analysts Annual Logging Symposium, 26th, Dallas, 1985, Transactions, Society of Professional Well Log Analysts, pp. JJJ1-JJJ31.

Papadopoulos, I. S., 1965. Non-steady flow to a well in an infinite anisotropic aquifer, Symposium, Int. Assn. Sci. Hydr., Dubrovnik, Yugoslavia, 21-30, 1965.

Papadopoulos, I. S., and H. H. Cooper, Jr., 1967. Drawdown in a well of large diameter, *Water Resour. Res., 3*(1), 241-244.

Peaceman, D. W., 1978. Interpretation of well-block pressures in numerical reservoir simulation, *Soc. Pet. Eng. J., AIME, 18*(3), 283-294.

Ramey, H. J., Jr., 1970. Approximate solutions for unsteady liquid flow in composite reservoirs, *J. Canadian Pet. Tech., 9*, 32-37.

Ramey, H. J., Jr., 1982. Well-loss function and skin effect: a review, *in* Narasimhan, T. N., ed., Recent Trends in Hydrogeology, Special Paper 189, *Geol. Soc. Amer.*, 265-271, 1982.

Rorabaugh, M. I., 1953. Graphical and theoretical analysis of step-drawdown test of artesian well, *Amer. Soc. Civil Eng. Proc., 79*, sect. 362, 23pp.

Segall, P., and C. Simpson, 1986. Nucleation of ductile shear zones on dilatant fractures, *Geology, 14*, 56-59.

Segall, P., and D. D. Pollard, 1983a. Joint formation in granitic rock of the Sierra Nevada, *Geol. Soc. Amer. Bull., 94*, 563-575.

Segall, P., and D. D. Pollard, 1983b. Nucleation and growth of strike slip faults in granite, *J. Geophys. Res., 88*, 555-568.

Segall, P., McKee, E. H., Martel, S. J., and B. D. Turrin, 1990. Late Cretaceous age of fractures in the Sierra Nevada batholith, California, *Geology, 18*, 1248-1251.

Strahler, A. N., 1981. "Physical Geology." Harper & Row, New York, 612 pp.

van Everdingen, A. F., 1953. The skin effect and its influence on the productive capacity of a well, *Trans., AIME, 198*, 171-176.

Zemanek, J., Caldwell, R. L., Glenn, E. E., Jr., Holcomb, S. V., Norton, L. J., and A. J. D. Straus, 1969. The borehole televiewer - a new logging concept for fracture location and other types of borehole inspection, *J. Pet. Tech., 21*(6), 762-774.

APPENDIX 1: MEASUREMENTS AND CALCULATIONS OF BOREHOLE FRACTURE PROPERTIES

Notation:

2b=average thickness of fracture trace [ft]

D=diameter of borehole [ft]

H=middleL-middleH [ft]

h=horizontal trace

middleH=shallowest depth of the middle of the fracture trace [ft] (relative to top of casing for that particular well).

middleL=deepest depth of the middle of the fracture trace [ft] (relative to top of casing for that particular well).

β=dip angle [degrees]

$\delta\beta$=dip angle uncertainty [degrees]

δH=uncertainty in H [ft]

θ=dip azimuth [degrees] (0=magnetic north). Degrees increase clockwise.

Since the dip angle calculation is arctan(H/D), the uncertainty in the dip angle calculation is a function of the relative uncertainty of H and of D. From the general formula for error propagation, the dip angle uncertainty can be shown to be

$$\delta\beta = \frac{H \times D \times \sqrt{\left(\frac{\delta H}{H}\right)^2 + \left(\frac{\delta D}{D}\right)^2}}{H^2 + D^2}$$

To calculate $\delta\beta$, a nominal value of D = 0.55 ft and δD=0.002 ft was used. For most fractures, δH was taken as 0.10 ft, the value to which interpolations in H were made. For fractures whose trace thickness was larger than 0.1 ft, δH was taken as the trace thickness.

WELL 0-0							
#	depth [ft]: middleH	middleL	θ	apparent 2b [ft]	H [ft]	β	$\delta\beta$
1	40.30	41.60	0	0.03	1.30	67.1	1.58
2	59.20	63.50	270	0.80	4.30	82.7	1.34
3	59.10	62.70	60	0.60	3.60	81.3	1.43

WELL 0-0 CONT'

#	depth [ft]: middleH	middleL	θ	apparent 2b [ft]	H [ft]	β	δβ
4	69.60	71.10	135	0.30	1.50	69.9	3.70
5	73.90	76.00	135	0.30	2.10	75.3	2.01
7	80.00	81.40	140	0.10	1.40	68.6	1.39
8	86.40	87.10	310	0.03	0.70	51.8	3.98
9	92.40	93.00	90	0.06	0.60	47.5	4.76
10	94.30	98.00	h	3.80	3.70	0.0	81.8
11	99.40	99.40	h	0.03	0.00	0.0	3.1
12	100.20	100.40	h	0.20	0.20	0.0	20.0
13	101.40	102.30	165	0.06	0.90	58.6	2.83
14	103.00	104.20	140	0.40	1.20	65.4	1.81
15	111.80	112.40	350	0.12	0.60	47.5	4.76
17	124.60	125.60	150	0.06	1.00	61.2	2.42
18	126.00	126.40	245	0.09	0.40	36.0	6.81
19	126.40	130.00	140	0.30	3.60	81.3	0.71
20	128.00	128.40	140	0.09	0.40	36.0	6.81
21	139.00	140.50	270	0.30	1.50	69.9	3.70
22	140.90	144.80	245	0.25	3.90	82.0	0.51
24	145.40	145.90	235	0.09	0.50	42.3	5.70
25	146.20	147.00	250	0.09	0.80	55.5	3.34
26	145.90	146.80	20	0.03	0.90	58.6	2.83
27	151.40	151.90	0	0.06	0.50	42.3	5.70
28	155.00	159.00	240	0.20	4.00	90.0	na
29	164.20	164.65	60	0.11	0.45	39.3	6.24
30	168.60	170.30	50	0.14	1.70	72.1	0.99
31	173.70	175.30	140	0.14	1.60	71.0	2.75
32	174.50	175.00	280	0.09	0.50	42.3	5.70
33	180.00	180.50	0	0.06	0.50	42.3	5.70
35	184.25	185.00	340	0.08	0.75	53.7	3.64
36	185.40	185.70	280	0.05	0.30	28.6	8.03
37	186.90	187.30	280	0.06	0.40	36.0	6.81
39	189.20	190.00	165	0.09	0.80	55.5	3.34
41	195.18	195.44	250	0.03	0.26	25.3	8.52
42	195.40	195.76	240	0.03	0.36	33.2	7.29
43	196.20	196.90	250	0.05	0.70	51.8	3.98
44	196.70	197.50	245	0.06	0.80	55.5	3.34
45	197.60	197.90	300	0.11	0.30	28.6	8.03
46	198.00	198.44	270	0.03	0.44	38.7	6.35
47	199.10	199.60	40	0.09	0.50	42.3	5.70
48	200.00	200.50	140	1.10	0.50	42.3	5.70
49	200.50	202.60	135	0.06	2.10	75.3	0.67
51	204.30	206.60	100	0.06	2.30	76.6	0.57
52	204.60	205.30	280	0.03	0.70	51.8	3.98
53	210.00	211.60	145	0.06	1.60	71.0	2.20
55	212.10	212.90	280	0.09	0.80	55.5	6.69
56	213.30	214.20	230	0.05	0.90	58.6	2.83
59	215.80	216.80	245	0.09	1.00	61.2	4.84
60	219.00	219.20	220	0.06	0.20	20.0	9.20
61	220.30	220.60	280	0.06	0.30	28.6	8.03
62	220.80	223.80	275	2.40	3.00	79.6	0.34
63	224.10	229.00	130	0.11	4.90	83.6	0.13
64	229.60	234.00	140	0.40	4.40	90.0	0.16

WELL 0-0 CONT'

#	depth [ft]: middleH	middleL	θ	apparent 2b [ft]	H [ft]	β	δβ
	INCOMPLETE TRACES:						
6		76.30	50				
16		117.50	295				
23	143.9		315				
28							
34		181.60	280				
38	188.30		40				
40	192.70	192.90				19.8	
50	203.40	204.20	90	0.60	0.80	55.5	20.06
54							
57	214.20		305				
58		215.50	230				
64							
65	234.00	234.20	0	0.12		20.0	
66	233.56	235.20	310	na		71.5	
67							
68							

WELLSE-1

#	depth [ft]: middleH	middleL	θ	apparent 2b [ft]	H [ft]	β	δβ
0.5	51.80	53.10	130	0.03	1.30	66.9	1.75
1	55.40	56.70	50	0.09	1.30	66.9	3.25
2	73.00	73.60	310	0.20	0.60	47.3	9.57
4	82.00	83.00	70	0.05	1.00	61.0	2.57
5	83.10	85.00	300	0.02	1.90	73.7	0.98
6	83.70	84.80	70	0.02	1.10	63.3	2.24
8	89.00	91.20	70	0.06	2.20	75.9	0.78
9	90.00	90.50	0	0.24	0.50	42.1	22.84
10	89.60	91.20	70	0.06	1.60	70.9	2.29
11	90.50	90.90	150	0.06	0.40	35.8	6.89
12	90.60	91.90	130	0.05	1.30	66.9	1.75
13	92.20	92.80	155	0.02	0.60	47.3	9.57
14	92.80	94.50	160	0.06	1.70	72.0	1.16
15	93.90	94.50	155	0.05	0.60	47.3	4.87
16	96.40	97.00	h	0.60	0.60	0.0	47.3
18	101.60	103.10	150	0.20	1.50	69.7	2.56
19	104.90	105.90	280	0.08	1.00	61.0	4.92
20	105.90	106.20	340	0.05	0.30	28.4	8.08
21	118.50	119.00	230	0.60	0.50	42.1	17.14
22	119.40	120.00	210	0.06	0.60	47.3	9.57
23	124.10	124.60	240	0.08	0.50	42.1	5.80
24	135.60	142.00	135	0.20	na	90.0	na
26	137.60	138.80	50	0.05	1.20	65.2	1.97

WELL SE-1 CONT'

#	depth [ft]: middleH	middleL	θ	apparent 2b [ft]	H [ft]	β	δβ
27	141.80	142.40	240	0.14	0.60	47.3	9.57
28	143.40	143.80	260	0.06	0.40	35.8	6.89
29	143.20	147.40	140	0.06	4.20	82.5	0.75
30	160.60	161.80	80	0.02	1.20	65.2	7.28
31	167.10	168.00	340	0.02	0.90	58.4	11.37
32	168.80	169.50	255	0.06	0.70	51.6	8.02
33	172.90	173.20	260	0.03	0.30	28.4	8.08
34	172.60	175.20	255	0.30	2.60	78.0	1.40
35	174.00	174.40	70	0.06	0.40	35.8	6.89
36	174.50	175.20	70	0.30	0.70	51.6	11.97
37	176.10	176.90	70	0.05	0.80	55.3	3.48
38	176.60	178.80	70	0.06	2.20	75.9	1.32
39	177.40	177.70	0	0.09	0.30	28.4	8.08
41	180.20	180.80	280	0.06	0.60	47.3	4.87
42	181.00	181.40	280	0.03	0.40	35.8	6.89
42.5	182.00	183.00	90	1.20	1.00	61.0	9.72
43	191.00	191.10	h	0.03	0.03	0.0	10.2
45	192.80	193.10	320	0.03	0.30	28.4	8.08
46	193.80	194.30	20	0.20	0.50	42.1	11.45
47	195.20	195.50	345	0.08	0.30	28.4	8.08
48	196.00	196.40	270	0.05	0.40	35.8	6.89
49	197.60	199.40	280	1.50	1.80	72.9	1.87
50	199.60	202.40	h	2.80	2.80	0.0	78.8
51	202.60	203.20	330	0.03	0.60	47.3	4.87
52	204.20	204.80	260	0.40	0.60	47.3	19.05
53	206.20	206.60	290	0.50	0.40	35.8	13.66
54	207.60	208.20	100	0.17	0.60	47.3	28.56
56	205.70	205.90	280	0.03	0.20	19.9	9.23
57	211.30	211.60	281	0.50	0.30	28.4	8.08
58	211.40	215.40	0	0.20	4.00	82.1	0.48
59	213.60	214.70	280	0.40	1.10	63.3	4.25
60	215.40	215.70	270	0.20	0.30	28.4	8.08
61	216.10	216.60	210	0.12	0.50	42.1	5.80
62	216.80	217.20	235	0.11	0.40	35.8	6.89
63	218.10	219.00	0	0.08	0.90	58.4	2.98
64	221.40	221.80	0	0.70	0.40	35.8	20.46
65	222.90	223.10	310	0.25	0.20	19.9	18.41
66	223.90	224.10	310	0.15	0.20	19.9	9.23
68	233.30	235.50	0	0.12	2.20	75.9	1.32
69	238.80	241.60	0	2.80	2.80	78.8	0.55
70	242.40	242.40	0	0.20	0.00	0.0	19.9
	INCOMPLETE TRACES:						
3		80.80	140				
7							
17	97.20		25				
25		136.00	135				
40	180.00		330				
44	192.00		80				
55	210.00		105				
67	233.00		0				

WELL SW-1

#	depth [ft]: middleH	middleL	θ	apparent 2b [ft]	H [ft]	β	δβ
1	34.50	35.75	140	0.20	1.25	66.1	1.86
2	35.30	36.70	140	0.15	1.40	68.4	1.56
8	47.74	48.80	55	0.06	1.06	62.4	2.37
10	51.86	52.20	180	0.40	0.34	31.5	7.59
11	54.52	55.40	60	0.20	0.88	57.8	8.83
12	57.10	57.50	285	0.11	0.40	35.8	6.89
14	61.60	62.80	60	0.10	1.20	65.2	3.70
15	68.16	68.60	270	0.80	0.44	38.5	12.74
17	80.00	81.36	135	0.20	1.36	67.8	3.02
18	83.40	83.90	260	0.23	0.50	42.1	11.45
20	89.40	91.00	140	0.20	1.60	70.9	2.29
22	93.20	93.80	285	0.10	0.60	47.3	4.87
23	93.80	94.40	285	0.10	0.60	47.3	4.87
24	94.40	95.00	285	0.20	0.60	47.3	4.87
25	95.60	95.60	285	1.50	0.40	45.0	27.27
26	104.30	105.80	60	0.06	1.50	69.7	2.56
27	106.10	106.50	0	0.03	0.40	35.8	6.89
28	111.50	111.90	260	0.10	0.40	35.8	6.89
29	112.20	112.40	180	0.03	0.20	19.9	9.23
31	116.80	118.30	80	0.08	1.50	69.7	2.56
35	120.60	121.80	145	0.08	1.20	65.2	3.70
36	121.26	122.00	310	0.11	0.74	53.2	7.48
37	125.50	126.40	280	0.05	0.90	58.4	2.98
38	125.50	126.84	70	0.06	1.34	67.5	1.67
39	128.00	128.20	145	0.09	0.20	19.9	9.23
40	128.60	130.50	145	0.20	1.90	73.7	1.70
43	133.00	134.50	70	0.05	1.50	69.7	1.41
45	136.30	136.80	285	0.09	0.50	42.1	5.80
47	140.00	141.80	150	0.20	1.80	72.9	1.87
48	145.00	146.30	70	0.02	1.30	66.9	1.75
53	154.48	154.90	270	0.15	0.42	37.2	9.92
54	155.60	158.50	80	0.15	2.90	79.2	0.66
57	165.00	166.10	160	0.09	1.10	63.3	2.24
58	166.40	167.00	20	0.18	0.60	47.3	14.31
60	176.00	176.00	h	0.40	0.20	0.0	35.8
63	187.40	188.06	280	0.20	0.66	50.0	8.60
64	188.60	189.00	295	0.06	0.40	35.8	6.89
65	189.00	189.46	295	0.05	0.46	39.7	6.21
66	189.36	189.74	295	0.08	0.38	34.4	7.12
67	189.60	190.10	300	0.11	0.50	42.1	5.80
68	190.14	190.44	290	0.14	0.30	28.4	8.08
69	190.60	190.90	320	0.14	0.30	28.4	8.08
70	191.40	191.70	310	0.06	0.30	28.4	8.08
71	191.70	192.04	320	0.06	0.34	31.5	7.59
72	192.00	192.32	320	0.15	0.32	30.0	7.84
73	192.38	192.50	320	0.08	0.12	12.2	9.95

WELL SW-1 CONT'

#	depth [ft]: middleH	middleL	θ	apparent 2b [ft]	H [ft]	β	δβ
74	193.50	194.40	60	0.05	0.90	58.4	2.98
75	196.30	198.20	50	0.09	1.90	73.7	1.70
76	198.70	199.40	0	0.25	0.70	51.6	9.99
77	200.40	201.30	60	0.10	0.90	58.4	2.98
78	200.60	203.90	60	0.23	3.30	80.5	0.66
79	207.80	208.80	165	0.30	1.00	61.0	7.31
81	213.60	214.40	160	0.20	0.80	55.3	6.76
82	215.00	216.10	145	0.03	1.10	63.3	2.24
83	218.00	218.50	60	0.02	0.50	42.1	8.62
84	221.40	222.10	170	0.05	0.70	51.6	4.10
85	222.26	223.00	300	0.14	0.74	53.2	11.17
86	223.40	223.90	310	0.40	0.50	42.1	5.80
87	223.80	224.50	310	0.14	0.70	51.6	11.97
88	224.30	227.60	310	3.30	3.30	80.5	1.18
89	231.50	231.70	180	0.05	0.20	19.9	9.23
90	232.40	232.60	150	0.05	0.20	19.9	9.23
91	235.60	236.80	0	0.15	1.20	65.2	3.70
	INCOMPLETE TRACES:						
3		37.20	140				
4	37.60		50				
5	41.10	41.10					
6		43.90	180				
7	42.20	46.00					
9	49.30						
13	60.80	61.30	90	na		42.1	
16							
19	86.40	86.40	h	1.50		0.0	
21		91.60	260				
30	114.30		75				
32		120.10	75				
33		120.30	75				
34		116.80	75				
41	129.90	131.20	65	0.06		66.9	
42		132.60	65				
49		147.70	65				
50		148.96	65				
51		152.40	65				
52		153.34	100				
55	156.80		80				
56	157.46		80				
44		136.30	285				
46		137.40	75				
59		170.00	290				
61		180.60	50				
62	184.30		60				
80	211.10		50				

APPENDIX 2: DOWNHOLE FLOWMETER MEASUREMENTS

Notation:

t=time since pumping began [sec]
z=depth below top of casing for that particular well [m] (see Fig. 5.5)
R=flowmeter reading [rpm]
+/-=variation in flowmeter reading
Qt=total discharge from well [gpm]
psi=inflatted pressure of packer

Calibration curve for test SE-1 and SW-1:

Q[gpm]=0.019R[rpm]+0.818
r^2=0.995
n=20
range=1.2-30 gpm

Calibration curve for test 0-0:

Q[gpm]=0.017R[rpm]+1.05
r^2=0.995
n=45
range=1.9-9.05 gpm

SE-1:

to=10:31, 10/23/92 = PUMP ON

t [sec]	z [m]	R [rpm]	+/-	Qt [gpm]	psi	Pump @ [m]	Transducer @ [m]
900	-22.6	126		na	50	19.8	18.9
1740	-22.6	142		na	75	19.8	18.9
2160	-22.6	143		4.1	75	19.8	18.9
2700	-22.6	146.5	0.5	4.13	75	19.8	18.9
3360	-23.9	119	1.0	4.23	75	19.8	18.9
3720	-25.4	113	1.0	4.2	77	19.8	18.9
4080	-28.7	103.5	0.5	4.22	80	19.8	18.9
4380	-30.0	56	1.0	4.23	80	19.8	18.9
na	-31.5	0		na	80	19.8	18.9
4980	-33.0	0		4.18	80	19.8	18.9
na	-31.2	0		4.18	80	19.8	18.9
na	-30.9	32	1.0	4.21	80	19.8	18.9
na	-30.6	31	1.0	4.21	na	19.8	18.9
na	-21.4	166		4.25	60	19.8	18.9
na	-21.4	167		4.16	60	16.8	15.8
na	-21.1	167		4.17	60	16.8	15.8
na	-20.8	163		4.18	60	16.8	15.8
na	-20.8	165		4.11	70	16.8	15.8
na	-19.6	162		4.17	70	16.8	15.8
8100	=12:46 = PUMP OFF						

SW-1:

to=13:19, 10/23/92 = pump on

t [sec]	z [m]	R [rpm]	+/-	Qt [gpm]	psi	Pump @ [m]	Transducer @ [m]
120	-20.8			4.12	na	16.8	15.8
2100	-20.8	127		4.21	70	16.8	15.8
2220	-20.8	132		4.23	70	16.8	15.8
2580	-22.3	80		4.12	70	16.8	15.8
2880	-23.8	74		4.06	70	16.8	15.8
3240	-25.3	65		4.05	75	16.8	15.8
3540	-26.8	61	1.0	4.12	75	16.8	15.8
3900	-31.4	62	1.0	4.15	75	16.8	15.8
4200	-34.5	61.5	1.0	4.15	76	16.8	15.8
4500	-37.5	59	1.0	4.14	80	16.8	15.8
4860	-40.6	60	1.0	4.16	90	16.8	15.8
5220	-43.6	57	1.0	4.18	95	16.8	15.8
5460	-46.7	60	1.0	4.2	97	16.8	15.8
5760	-49.7	60	1.0	4.19	107	16.8	15.8
6060	-52.8	60	1.0	4.2	110	16.8	15.8
6360	-55.8	60	1.0	4.2	100	16.8	15.8
6600	-58.9	59.5	1.5	4.2	115	16.8	15.8
6900	-61.9	60	1.0	4.19	120	16.8	15.8
7080	-63.4	61	1.0	4.2	122	16.8	15.8
7440	-65.6	0		4.2	125	16.8	15.8
7680	-64.9	0		4.22	125	16.8	15.8
7920	-64.3	0		4.21	124	16.8	15.8
na	-64.0	0		4.2	120	16.8	15.8
na	-63.7	0		4.21	120	16.8	15.8
na	-63.7	0		2.3	130	16.8	15.8
na	-63.4	66		4.15	125	16.8	15.8
8880	=15:47	=PUMP	OFF				

0-0:

to=12:35, 11/5/92 = pump on

t [sec]	z [m]	R [rpm]	+/-	Q [gpm]	psi	Pump@ [m]	Transducer@ [m]
180	-19.2	155		6.13	70	16.2	15.8
300	-19.2	188.5	0.5	6.07	70	16.2	15.8
540	-19.2	211	1	6.05	70	16.2	15.8
840	-19.2	214.5	0.5	6.06	70	16.2	15.8
1275	-19.2	219		6.02	70	16.2	15.8
1320	-19.2	219		6.02	70	16.2	15.8
1590	-19.2	224.5	0.5	6.02	70	16.2	15.8
2100	-19.2	226		6.04	70	16.2	15.8
2580	-19.2	233	0.5	6.02	70	16.2	15.8
3180	-23.8	228	0.5	6.01	75	16.2	15.8
3540	-26.8	221	1	5.98	80	16.2	15.8
3660	-26.8	234.5	0.5	6.00	80	16.2	15.8
3960	-28.4	231.5		6.00	75	16.2	15.8
4020	-28.4	232		6.00	75	16.2	15.8
4080	-28.4	237		6.02	75	16.2	15.8
4440	-31.7	0		6.03	60	16.2	15.8
4620	-31.1	0		6.06	65	16.2	15.8
4770							

LAWRENCE BERKELEY LABORATORY
UNIVERSITY OF CALIFORNIA
TECHNICAL INFORMATION DEPARTMENT
BERKELEY, CALIFORNIA 94720

ABH203
LBL Libraries